TECHNISCHE UNIVERSITÄT MÜNCHEN

Fakultät für Physik
Lehrstuhl für Funktionelle Materialien

Nanostructuring and Understanding Morphology-Property Correlation in Semiconductor Thin Films

Rui Wang

Vollständiger Abdruck der von der Fakultät für Physik der Technischen Universität München zur Erlangung des akademischen Grades eines

Doktors der Naturwissenschaften (Dr. rer. nat.)

genehmigten Dissertation.

Vorsitzender:	Prof. Dr. Martin Zacharias
Prüfer der Dissertation:	1. apl. Prof. Dr. Peter Müller-Buschbaum
	2. Prof. Dr. Ian Sharp

Die Dissertation wurde am 31.01.2018 bei der Technischen Universität München eingereicht und durch die Fakultät für Physik am 22.03.2018 angenommen.

Abstract

In this thesis the morphology and the functional properties of two kinds of semiconductor thin films based on conjugated diblock copolymer and organometal halide perovskite are investigated. The focus is on tailoring the film nanostructure and on elucidating its impact on the optoelectronic and optical behaviors. Advanced X-ray and neutron scattering techniques are combined with surface sensitive imaging methods to obtain a full picture of the resulting morphology. We find that, the self-assembly of P3HT-*b*-PS is dramatically influenced by the addition of PCBM, which accordingly effects on the exciton dissociation behavior. The crystal orientation of lead bromide perovskite crystal can be effectively tuned by adding long organic ligands. An identical crystal orientation between 3D and 2D perovskite crystals as well as a compact film domain structure lead to the arise of the amplified spontaneous emission (ASE).

Zusammenfassung

In dieser Dissertation wurden die Morphologie und die funktionellen Eigenschalten von zwei dünnen Halbleiterfilmen am konjugiertem Diblockcopolymeren und Organometall Halogenid-Perovskit untersucht. Der Fokus lag darauf, die Nanostruktur der Filme zu verändern und dessen Einfluss auf optoelektronische und optische Verhaltensweisen zu erläutern. Moderne Röntgen- und Neutronenstreumethoden wurden in Kombination mit oberflächensensitiven Bildgebungsverfahren verwendet, um die resultierenden Morphologie zu bestimmen. Es wurde gezeigt, dass P3HT-*b*-PS durch die Zugabe von PCBM stark beeinflusst wird, was folglich ein Einfluss auf die Exzitonen-Dissoziation hat. Die Kristallorientierung des Bleibromid Perowskitkristalls kann wirksam durch Hinzufügen von langen organischen Liganden abgestimmt werden. Mit einer identischen Kristallorientierung zwischen 3D und 2D Perowskitkristallen in Kombination mit einer kompakten Filmdomänenstruktur wird eine verstärkte spontane Emission erreicht.

Contents

1 Introduction

The rapid growth of global industrialization and the evolving ecological concerns in last decades post new challenges for the application of advanced technologies. In order to meet the requirements of modern society, innovative materials with outstanding properties hold the key to the technological advances since the performance of devices and the properties of materials are closely interrelated.

Among the emerging new materials, nanostructured materials have gathered great interests not only in science, but also play an ever increasing role in the daily life in twenty-first century. [1] More and more products based on nanostructured materials have been realized in markets, covering diverse applications such as energy conversion, energy storage, semiconductor devices and biotechnology. [2–5] With dimensions been tailored with atomic accuracy, nanostructured materials experience tremendous changes of both the physcial and the chemcial properties. [3] The surface to volume ratio changed incrementally in nanostructured materials due to size tuning. The interface phenomenon becomes notable and both bulk and surface properties are combined in such materials. [6] As a consequence, unique mechanical, electrical and optical properties appear. In the present thesis, two nanostructured semiconductor material systems, conjugated diblock copolymers:fullerene blends and organometal halide perovskite are investigated as model systems for their potentially applications of organic photovaltics (OPV) and optical gain media, respectively. For both systems, samples are prepared in thin films with respect to the geometry of real device.

Conjugated polymers exhibit intriguing optical and optoelectronic properties due to their overlapping π-orbitals that creates delocalized π-electrons. In polymer-based organic solar cells, conjugated polymers act as electron donor and blended with fullerene derivatives (typically, PCBM), which act as electron acceptor. A high performance organic solar cell features a so-called bulk heterojunction (BHJ) morphology, in which electron donor and electron acceptor form an interpenetrating network with structure sizes on the same length scale of the exciton diffusion length (10-20 nm). [7, 8] This structural layout exhibit shorten domain sizes for exciton transportation and large interface areas for charge carriers separation. According to such crucial requirement, conjugated diblock polymers attract high expectation for OPV application due to its intrinsic microphase separation

behavior. In conjugated diblock copolymers, the conjugated polymer is connected with another polymer moiety via covalent bond. Instead of macrophase separation, conjugated diblock copolymers can form a various kinds of nanostructures via self-assembly due to microphase separation. [9, 10] The morphology of conjugated diblock copolymers can be tuned by the addition of functional additives. The ordered nanoscale morphology of the pristine conjugated diblock copolymer becomes disordered at higher loading of PCBM content. [11] However, by directly blending diblock copolymer with PCBM, so far no good OPV device as compared to homo-polymer:PCBM blends can be obtained. Therefore, it is important to obtain a detailed understanding about the morphology evolution of the diblock copolymer:fullerene blends at different blending stages.

Organometal halide perovskite materials emerged as a promising material for optoelectronic and optical applications in last decades due to their outstanding dielectric properties and tunable wide absorption spectrum. [12, 13] The dimensional structures of perovskite crystals can be nanostructured from three-dimensional (3D) bulk crystals down to zero-dimensional (0D) nanoparticles by using long organic ligand as structural template. [14] In response to the sizable changes, nanostructured perovskite crystals can exhibit quantum confinement effects, which accordingly impacts on the optoelectronic behavior. By decreasing the size of perovskite crystals smaller than the de Broglie wavelength and the mean free path of electrons, discrete energy levels arise instead of the continuous density of states (DOS) for bulk materials. As a consequence, the resulting perovskite crystals exhibit an increased band gap and its absorption shifts toward large energies. [15,16] Further, for perovskite films containing both 3D and low dimensional crystals, the resulting optoelectronic devices enjoy increased performance as a consequence of the interaction between different dimensional structures. [17, 18] In order to better control the crystal formation and further boost these materials in industrial application, the understanding of the interaction between different dimensional perovskite crystals and its correlation on the functional property is essential.

The fundamental aspects in this thesis contain three chapters. The theoretical background is first detailed in chapter 2 in terms of the basics of polymers, organometal halide perovskite and the fundamentals of the scattering methods that used for structure investigation. Thereafter, chapter 3 describes all the used characterization methods as well as the experimental parameters, followed by the sample preparation of diblock copolymer and perovskite thin films and a description of the involved materials in chapter 4. Research highlights as the main part of this thesis are presented in chapter 5 and chapter 6.

Chapter 5 elucidates the influence of the addition of PCBM on the P3HT-*b*-PS thin films. The weight fraction of PCBM in the BHJ films is varied from 9% to 67%. This

wide range of compositional variation is expected to distinctly affects the self-assembly of P3HT-*b*-PS. Further, the morphological changes is assumed to directly impact on the optoelectronic property of the BHJ films. Through the comparison between the obtained morphological and spectroscopy results, the following questions are addressed:

- How does PCBM distribute in the BHJ film at different compositions?
- Can the addition of PCBM effects on the molecular order of the P3HT-block?
- Does the PCBM addition has an impact on both, mesoscale and microscale structures of P3HT-*b*-PS? How does it correlate to the exciton dissociation quality?

In chapter 6, a mixture of organic ligands with different molecular lengths are used to prepare perovskite thin films. Due to the sizable effect of the longer organic ligand on the formation of perovskite crystal, the resulting crystals are expected to be mixed dimensions, i.e. a mixture of both 3D bulk and 2D platelets perovskite crystals. As a consequence, the functional property of the prepared thin films is assumed to have a combined characteristic of different crystal families. The resulting perovskite thin films are thoroughly characterized in terms of optical property, crystal structure, film morphology, and amplified spontaneous emission (ASE) behavior, aiming to answer the following questions:

- How do different dimensional crystals grow in the perovskite thin films?
- How does the addition of long organic spacer impact on the resulting film morphology?
- Can energy transfer from 2D platelets to 3D bulk crystals exists? Will the resulting morphology effects on the energy transfer efficiency? How does it correlate to the resulting ASE behavior?

At the end, the obtained results and a short outlook for future projects on the basis of this thesis is given in chapter 7.

2 Theoretical aspects

2.1 Polymer basics

This section covers some aspects of the fundamental background of polymer physics. Firstly, the theoretical definition of polymeric materials is presented (Section 2.1.1), followed by the introduction of diblock copolymers (Section 2.1.2). Both the phase separation behavior of polymer blends (Section 2.1.3) and the polymer crystallization behavior (Section 2.1.4) are described in details. Afterwards, the origin of the conductivity in polymeric materials is explained (Section 2.1.5). Lastly, a brief introduction of optoelectronic properties in polymer:fullerene blends closes this section (Section 2.1.6).

2.1.1 Basic definitions

Polymers are a kind of macromolecule that consist of a sequence of one or more covalently-bond repeating units, i.e. monomers. For example, N numbers of monomer A are covalently linked to each other and therefore created a polymer (named polyA or in short, PA) with molecular structure A-A-...-A-A. N is the degree of polymerization of a polymer, which defines the number of monomer units in a polymer. Typically, for a macromolecule called polymer the corresponding molecular weight M_w is higher than 10^4 g mol^{-1}. In contrast, macromolecules with M_w smaller than 10^4 g mol^{-1} are generally named as oligomers.

The process that describes the covalent linking of monomer units in polymer synthesise is called polymerization. However, the yielded polymer chains are hardly monodisperse in length, but rather have a certain length of distribution. Therefore, statistical mean values are used to describe synthetic polymers. Depending on the molar mass M_i of component i and the number of chains n_i of component i, the so-called number average molar mass M_n is defined as the first central moment of the statistical distribution of molar mass

$$M_n = \frac{\sum_i n_i M_i}{\sum_i n_i} \tag{2.1}$$

In addition, the so-called weight average molar mass M_w of a synthetic polymer is defined as the ratio of the second central moment to the first central moment

$$M_w = \frac{\sum_i w_i M_i}{\sum_i w_i} \tag{2.2}$$

with w_i being the total mass of polymer chains for component i

$$w_i = \sum\nolimits_i n_i M_i \tag{2.3}$$

On the basis of M_n and M_w, the polydispersity index P that describes the heterogeneity of the molar masses and the inconsistency U are

$$P = \frac{M_w}{M_n} = U + 1 \tag{2.4}$$

In the ideal case for monodisperse polymers, $P = 1$. However, besides nature-abundant macromolecule like proteins, the synthetic polymers generally exhibit a statistically distributed degree of polymerization with $P > 1$.

Three terms are highly important to define polymer architectures, which are constitution, configuration, and conformation. Depending on the types and the sequences of monomers, polymers can be categorized into different groups. In the simplest case, homopolymers only constituting of one type of monomer, such as the aforementioned PA. Polymers that are constructed from more than one type of monomers are caller copolymers. On the basis of architecture of different monomers, copolymers can be partitioned into different groups. For example, if copolymers contain an alternating sequence of different monomers, a so-called alternating copolymer is defined, e.g. A-B-A-B-...-B-A-B-A. In the case of diblock copolymers, the covalently-bond momoners are distributed in a specific sequence, e.g. A-A-A-...-*block*-...-B-B-B. More details are illustrated in the coming Section 2.1.2. An overview of polymer naming and descriptions can be found in IUPAC (International Union of Pure and Applied Chemistry) definitions. [19]

The configuration of the polymer chain describes the physical arrangement of the monomer residues along the backbone of the polymer chain. For example, depending on the geometrical arrangement for all the side groups, either on one side or on opposite sides with respect to the backbone, *cis*- or *trans*- configuration can be defined. Furthermore, polymers with configurationally identical repeating units are tactic polymers. If all the substitutes are located on the same side of the polymer backbone, it is called the isotactic polymer. Otherwise, syntactic polymer describes that the substitutes are alternating along the backbone. In addition, a regioregular polymer is derived from the same isomer of the monomer, otherwise a regiorandom polymer is defined. The degree of regioregularity in conjugated polymers is closely related to the crystallinity and subsequently optical properties.

The term confirmation describes the configuration of a polymer chain, which arises from the rotation of molecules or chain segments around single bonds within the polymer. The final shape of polymer chains are strongly dependent on the local environment. In the case of polymers dissolved in a so-called good solvent that favors intermixing with polymers, all chains are more stretched. However, in the case of a bad solvent environment, polymer chains tend to be tightly coiled in order to reduce the interface to the solvent molecules.

Different characteristic length scales can be used to describe the states of polymer conformation. The so-called contour length of polymer refers to the maximum length of a fully stretched chain. The conformation of polymer chain can be described using the end-to-end distance R_e

$$R_e = |\overrightarrow{r_N} - \overrightarrow{r_1}| \tag{2.5}$$

where $\overrightarrow{r_N}$ and $\overrightarrow{r_1}$ are the first and last position of an atom in the polymer chain with the degree of polymerization N, respectively. [20] However, the volume information of a polymer chain is not included in R_e. A more generally used term is the so-called radius of gyration R_g

$$R_g = \frac{1}{M}\sum\nolimits_i m_i(\overrightarrow{r_i} - \overrightarrow{r_c}) \tag{2.6}$$

where M is the total mass of the polymer chain, m_i and r_i are the mass and the position of the i-th component of the polymer, and r_c is the center of mass position. [20] Typically, R_g is widely used in describing polymer chains with Gaussian coil conformation and the value is on the order of several nanometers.

2.1.2 Diblock copolymers

As briefly described in the previous section, diblock copolymers consist of two identical monomers A and B, in which A and B are distributed in two individual chains and covalently-bond together. The resulting polymers is named polyA-*block*-polyB or in short as PA-*b*-PB. [21] In general, the two monomers have different degrees of polymerization N_A and N_B, from which, the block ratios f_A and f_B are defined as

$$f_A = \frac{N_A}{N_A + N_B} \tag{2.7}$$

$$f_B = \frac{N_B}{N_A + N_B} = 1 - f_A \tag{2.8}$$

In general, macrophase separation occurs in the case of blending different types of immiscible polymers. That is, the respective polymer chains demix and form domains on the order of several micrometer. [20] However, the components in diblock copolymers are covalently linked and therefore, macrophase separation cannot take place. Instead, diblock copolymers are self assembling into fine patterns on the order of chain length, i.e. nanometer scale, by microphase separation. The generated sizes of domains are determined by the chain fractions of each block. A detailed introduction is depicted in Section 2.1.3.

2.1.3 Phase separation

In applications, polymers can be blended, i.e. mixing of two or more different homopolymers. Homogeneous mixtures are commonly hard to achieve due to the incompatibility among different homopolymers. Therefore, multi-phase materials are deduced depending on Gibb's free energy. [22] Based on the mean-field theory, the Flory-Huggins equation (Equation 2.9) is widely used to describe the organization of a two components system. [23, 24]

$$\frac{\triangle G_m}{k_B\,T} = \frac{\phi_A\,ln\phi_A}{N_A} + \frac{\phi_B\,ln\phi_B}{N_B} + \chi\,\phi_A\,\phi_B \tag{2.9}$$

where $\triangle G_m$ is the free energy of mixing per unit voclume, k_B the Boltzmann's constant, T is the absolute temperature, ϕ_i and N_i are volume fractions and degrees of polymerization of component i, v is an arbitrary reference value, and χ denotes the interaction parameter between the two components. The first two parts describe the entropic contribution for randomly mixed chain molecules, whereas the enthalpic contribution is described by the last part through the interaction parameter χ. The interaction parameter can be empirically rewritten as [22]

$$\chi = \frac{\chi_h}{T} + \chi_s \tag{2.10}$$

where χ_h and χ_s denote the enthalpic and entropic parts of χ, respectively. The entropic component χ_s accounts the contributions from chain conformation, chain-end effects, monomer molecular structure and excess free volume. For a small value of χ, the two components are generally alike and establish a better mixing phase. An exemplary phase diagram is showed in Figure 2.1 for a mixture of polymers A and B with $N_A = N_B = N$. Depending on the thermodynamic minimization of the Gibb's free energy, either a homogeneous phase or a phase separation system forms. The exact situation is determined by the smaller value of Gibb's free energy for the two cases. More specifically, the critical point ϕ_c is determined by the third derivative of Gibb's free energy

$$\phi_c = \frac{1}{\sqrt{N_B/N_A} + 1} \tag{2.11}$$

Moreover, the critical value of polymer-polymer interaction parameter χ_c is calculated by the second derivative of Gibb's free energy that can be expressed as

$$\chi_c = \frac{1}{(2\,N_B)}(1 + \sqrt{\frac{N_B}{N_A}})^2 \tag{2.12}$$

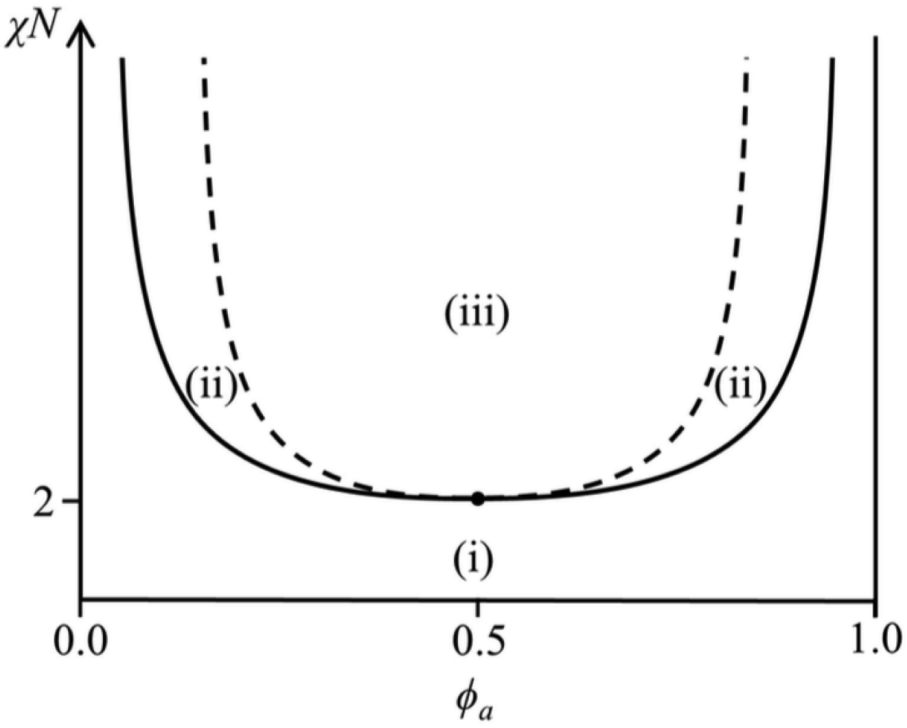

Figure 2.1: Phase diagram of a blend of polymer A and polymer B. Depending on the volume fraction of polymer A ϕ_a and varying values of χN, different phases can be described as: (i) a homogeneous mixture, (ii) a metastable region, and (iii) phase separated system. The image is adapted from literature. [20] The solid line is called binodal, the dashed line is called the spinodal, and a dot indicates the critical point.

On the condition of $N\chi_c = 2$, the miscibility gap is defined. [20] For products of stronger interaction between high molecular mass polymers, a phase-separation is observed as shown in Figure 2.1. For polymers with different degrees of polymerization, the phase diagram is asymmetric with respect to $\chi = 0.5$. [20]

Microphase separation

As aforementioned in Section 2.1.2, instead of blending two incompatible monomers, the two blocks are covalently-bond in diblock copolymers. As a consequence, macrophase separation is avoided and diblock copolymers are microphase separating on the nanometer scale via self-assembly. A general phase diagram for a conformationally symmetric diblock copolymer PA-*b*-PB is displayed in Figure 2.2 (adapted from [25]). The phase behavior depends on three parameters: the degree of polymerization N, the relative volume fraction of each block f and the Flory-Huggins interaction parameter χ. The self-assembled domain structures is predominantly dependent on the block ratio f in equation 2.7 and equation 2.8. In general, the sizes of the domains distributed from 10 nm to 100 nm can by tuned through the controlling of the molecular weight of diblock copolymers. [25]

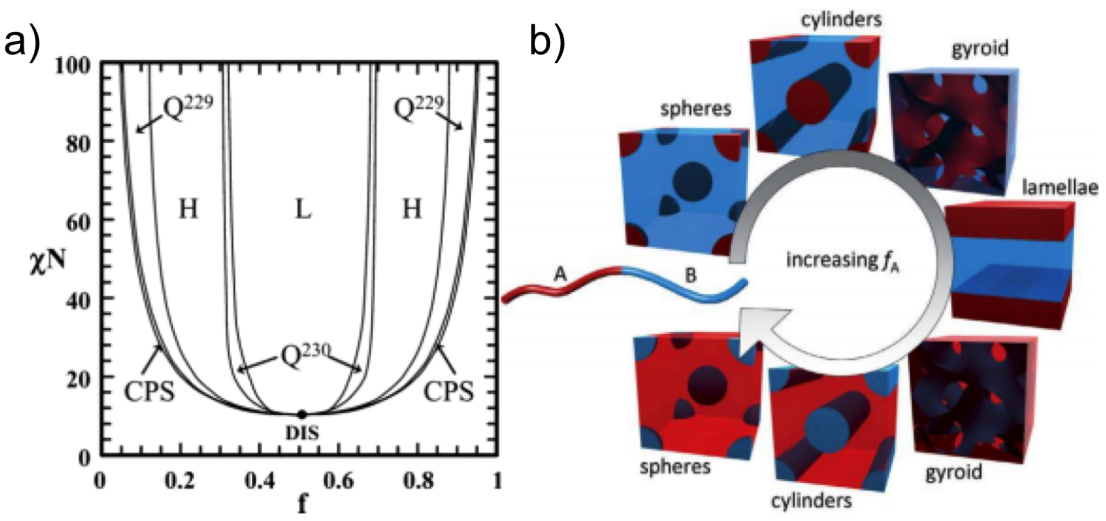

Figure 2.2: a) Phase diagram of a symmetric diblock copolymer PA-*b*-PB alongside changing the relative volume fraction of each block f: (L) lamellae, (H) hexagonally packed cylinders, (Q^{230}) double-dyroid phase, (Q^{229}) body-centered spheres, (CPS) closed-packed spheres, and (DIS) disordered. The black dot in phase diagram indicates the man-field critical point.b) Schematic descriptions of different structures of PA-*b*-PB with different degrees of f_A. The PA block is depicked in red whereas PB block in blue. The image is adapted from literature. [25]

The critical value in the case of symmetric blocks is $\chi_c N = 10.5$, the so-called weak segregation limit (WSL). For χN far below 10.5, diblock copolymers exsit as a homogeneous melt with no ordered structure. Upon increasing the value of χN, the two blocks start to repeal each other, which subsequently leads to local fluctuations of the volume concentration in the system. The so-called order-to-disorder (ODT) phase transition that happens due to the repulsion is strong enough to drive the phase separation. Upon further increasing the value of χN, pure domains for each block associated with sharp interfaces

are formed, which is the so-called as strong segregation limit (SSL) for $\chi N \ggg 10.5$. [26] WSL or SSL is hardly observed in some block copolymers due to the molecular weight.

In reality, the phase diagram of block copolymers is asymmetric. More specifically, a diversity of structures as well as crystallization properties of the monomers can affect the morphological development in diblock copolymers. Also, when going from bulk samples into thin films other structures are identifiable due to the boundaries at both the substrate and the air interfaces.

2.1.4 Polymer crystallization

The ordering of conjugated polymer chains is closely correlated to their optical properties. For example, the charge carrier mobility in crystalline regions of P3HT is orders of magnitudes highers than the amorphous parts. [27] Therefore, understanding of mechanisms of polymer crystallization is important for organic optoelectronic devices.

In contrast to small organic molecules, polymer crystallites do not form complete crystals but exist in a semicrystalline state. That is, the crystallized polymer parts distribute in an amorphous matrix of the same polymer (Figure 2.3). Polymer crystallites posses a lamellar-like structure with a layer thickness of d_c whereas the amorphous parts in semicrystalline polymers mainly contain entangled chains, chain ends, impurities and defects. The lateral size for a semicrystalline polymer can grow up to several micrometers. [28] A complete crystallization state is entropically impeded by a high activation barrier to fully disentangle the coiled polymer chains. Therefore, the semi-crystalline state for polymers is kinetically determined in comparison to thermal equilibrium. In addition, polydispersity is another factor that hinders polymers to achieve full crystallization. The crystallinity (ϕ_c) of semi-crystalline polymers is defined by the volume fraction of the crystalline part

$$\phi_c = \frac{v_c}{v_c + v_a} \tag{2.13}$$

where v_c and v_a denote the volumes of crystallized and amorphous phases, respectively. The crystallinity of polymers is affected by varying factors, such as the type of side chains, the flexibility of the backbone and the polydispersity.

The physical states of polymer can be described by three characteristic temperatures, which are the glass transition temperature T_g, melting temperature T_m and crystallization temperature T_c. Polymers behave like solid and brittle-like material below T_g while they become soft and flexible upon heating the system temperature above T_g. This transition can be understood as the mobility of chain segments in polymer being enhanced when the

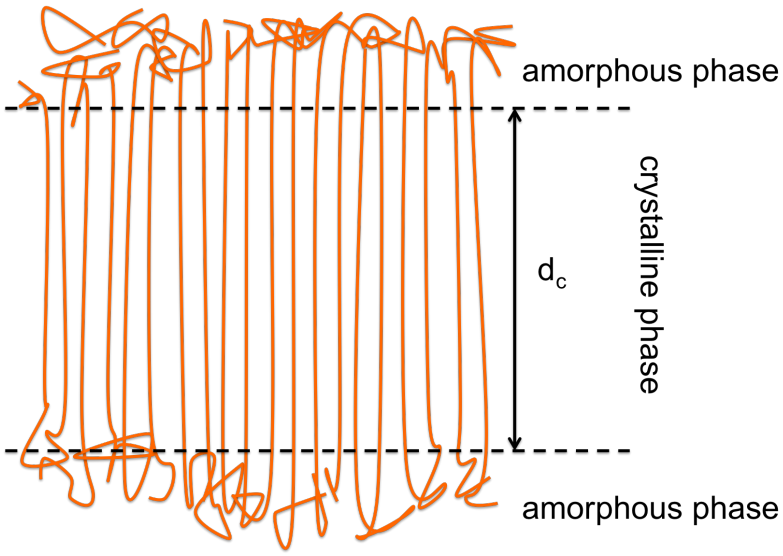

Figure 2.3: Sketch of polymer crystals with thickness d_c. The straight lines refer to the crystalline part of the backbone whereas the amorphous part is described by coils-like lines.

system temperature exceeds T_g. [20] At T_m, crystallites in semi-crystallite polymer start to be behave like amorphous liquid. T_c describes the temperature at which the polymer gains enough energy for crystallization to build ordered structures. T_c is typically between T_g and T_m. In the following sections, polymer crystallization is described by a multistage model proposed by Strobl. [20, 29]

Nucleation

Polymer crystallization from an amorphous state starts with nucleation. The nucleation rate ${\tau_{nuc}}^{-1}$ yields a proportional relationship to the volume of the crystallized domain v_c [30]

$$ {\tau_{nuc}}^{-1} \propto v_c \tag{2.14} $$

Moreover, base on the fact that T_c is located in between T_g and T_m, ${\tau_{nuc}}^{-1}$ is exponentially correlated to the temperature [31]

$$ {\tau_{nuc}}^{-1} \propto exp(-\frac{\triangle U + \triangle F_c}{k_B T}) \tag{2.15} $$

where k_B is the Boltzmann constant, $\triangle U$ the activation energy barrier for diffusion across the grain boundary, and $\triangle F_c$ the critical free energy barrier for primary nucleation. [32] Nucleation in polymer crystallization can be divided into two types. Firstly, nanometer-sized small particles with good internal ordering are formed as a consequence of thermal

fluctuations. These particles either functionalize as nuclei that allow crystal growth or dissociate due to thermal motion. This type of nucleation is a homogeneous process which is thermodynamically determined. Apart from this, impurities, dusts and defects can also behave as nuclei to affect nucleation in polymers. This process is considered as heterogeneous nucleation, in which polymer chains attach to the surface of those nuclei and start crystallization to build ordered structures.

Growth

After the nucleation process, polymer crystals start to grow. The folded coils in polymers start to develop ordering perpendicular to the chain direction. Microscopically, large spherulite-like structure as shown in Figure 2.4d can form on a length scale approaching several micrometers. However, these structures are not attractive for organic optoelectronic devices due to the big size compared to the exciton diffusion length (Section 2.1.6). Therefore, only early stages in polymer crystals development are detailed in this section.

The crystal formation in polymers from melt is irreversible and vice versa. More specificially, an intermediate mesoporphic state is introduced to explain the detailed processes. [33] It has been experimentally demonstrated that the crystallization and melting of polymers in the bulk can be illustrated by three characteristic temperatures: T_{am}^{∞} describes the transition from the melt to the mesomorphic phase, T_{ac}^{∞} describes the transition from the amorphous to the crystalline phase, and T_{mc}^{∞} desribes a virtual transition between the mesomorphic and the crystalline phase. [20] The three controlling temperatures are correlated as

$$T_{am}^{\infty} < T_{ac}^{\infty} < T_{mc}^{\infty} \tag{2.16}$$

The multistage model for describing polymer crystals growth is sketched in Figure 2.4. [34, 35] Polymer coils develop ordering in the melt by epitaxial forces, whereas defects are expelled from the mesophase associated with preliminary lamellae are formed (Figure 2.4a). After reaching a critical thickness value the core region solidifies and forms blocks (Figure 2.4b). In a final step, coils at the surface order to further stabilize the crystals (Figure 2.4c).

Based on this multistage model, a thermodynamic phase diagram is proposed by Strobl as shown in Figure 2.5 as a function of the inverse crystal thickness $1/n$ and the temperature T. [34] n represents the number of subunits and therefore the crystal thickness is defined as

$$d_c = n \triangle a \tag{2.17}$$

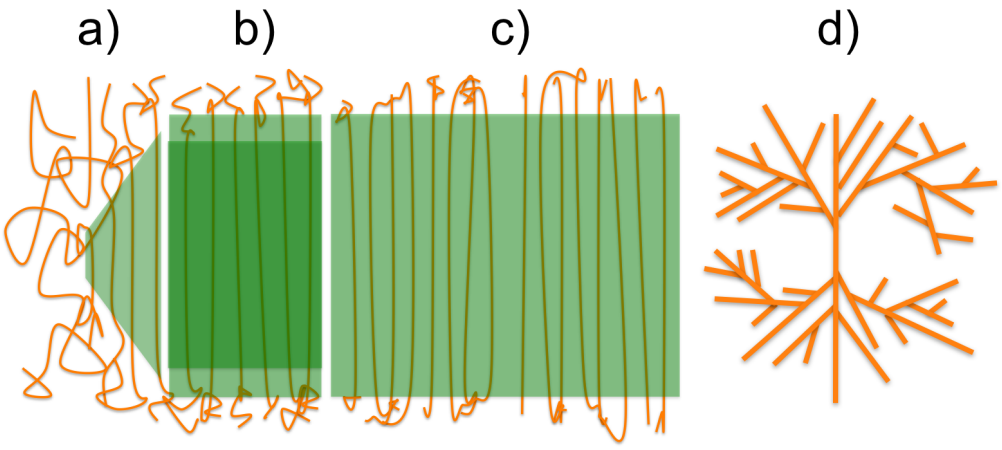

Figure 2.4: Sketch of a multistage model for polymer crystallization process. Polymers from melt start crystallization from (a) a mesomorphic phase, and thereafter undergoes (b) solidification by core crystallization and stabilize by (c) surface ordering. (d) An examplary spherulite structure formed upon crystal branching and splaying.

where $\triangle a$ is the length of the subunit. Four phases together with the respective transition lines are discussed: The amorphous melt, the mesomorphic phase and the crystalline phase which is detailed with two forms of the native crystal c_n and the stabilized crystal c_s. The effect of surface free energy and transition temperatures can be described by the Gibbs-Thomson equation

$$T_{ac}^{\infty} - T \approx \frac{2\,\delta_{ac_s}\,T_{ac}^{\infty}}{\triangle h_{ac}}\,\frac{1}{n} \tag{2.18}$$

where δ_{ac_s} denotes the surface free energy of a stabilized crystal and $\triangle h_{ac}$ is the heat of fusion. Equation 2.18 illustrates the reduction of the melting temperature as a consequence of the folded crystal surface. In more detail, the crystallization line and the recrystallization line can be respectively described equation 2.19 and equation 2.21

$$T_{mc}^{\infty} - T \approx \frac{(2\delta_{ac_n} - 2\delta_{am})\,T_{mc}^{\infty}}{\triangle h_{mc}}\,\frac{1}{n} \tag{2.19}$$

$$T_{mc}^{\infty} - T \approx \frac{(2\delta_{ac_s} - 2\delta_{am})\,T_{mc}^{\infty}}{\triangle h_{mc}}\,\frac{1}{n} \tag{2.20}$$

where δ_{ac_n}, δ_{ac_s}, δ_{am} and $\triangle h_{mc}$ refer to the corresponding surface free energies and the heat of fusion, respectively. The equilibrium melting temperature T_{ac}^{∞} in equation 2.18 decreases upon incorporating impurities whereas both crystallization and recrystallization lines are impurity independent.

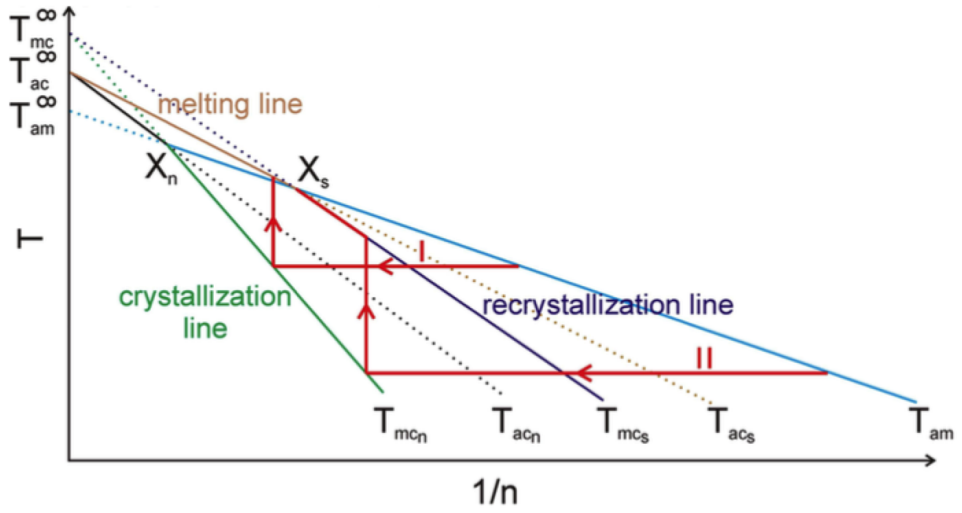

Figure 2.5: T/n^{-1} phase diagram of layered polymer crystals in an amorphous melt. Four phases are identified by the transition lines: (a) melt, (b) mesophase, (c_n) native crystals and (c_s) stabilized crystals as described by equations 2.18 to 2.21. The image is adapted from literature. [35]

Two identical processes of isothermal annealing followed by heating are depicted with red lines in Figure 2.5. In the case for high crystallization temperatures (process I), the crystal thickness is not influenced by heating until it reaches the melting line. However, in process II the crystal thickness increases once the recrystallization line is reached. With further heating, the crystal melts at the triple point χ_s. [34, 35]

2.1.5 Conductive polymers

In general, the major applications for polymers are generated from their mechanical properties and flexible processability. In the year 2000, the Nobel Prize was awarded to Heeger, Shirakawa and MacDiarmid for their discovery of conductivity in polymers. [36] Since then, tremendous effort had been applied to study conductive polymers. The conductivity in polymers is based on the delocalized π electrons. Thus, the π-orbitals overlap and merge together so that a large orbital is formed which secures the free movement of electrons. The overlapping π-orbitals form bonding π- and anti-bonding π^*-bands, in which the latter one is energetically unfavorable. The two are named the highest occupied molecular orbital (HOMO) and the lowest unoccupied molecular orbital (LUMO), respectively. The molecular structure for most conducting polymers contains alternating singe and double bonds along the backbone. These conjugated double bonds allow charge transportation in polymers. In the following sections, the conductivity in poly-

mers is discussed in detail in terms of band structure, charge carriers, doping and charge transport.

Band structure

The band structure of conjugated polymers can be generally described by Peierl's theorem. [37] For a one-dimensional chain with atoms all periodically located with a distance of a, the corresponding band is half-filled up to the Fermi level E_F as shown in Figure 2.6a. In this case, the system typically exhibits metallic properties. However, if the periodic distance is slightly distorted in case of conjugation or dimerization, a new superstructure lattice distance of $2a$ is defined (Figure 2.6b). Accordingly, the Brioullin zone is bisected and leads to the formation of an energy gap $\triangle E_{gap}$. Since the Fermi level remains unchanged, the system undergoes a transition from metal to insulator and generally known as the Peierl's instability. For polymers with atoms distributed in flexible chains, the Peierl's theorem is commonly applicable to understand the formation of a band gap and, to illustrate the intrinsic insulating as well as semiconducting nature of polymers. The band gap of polymers depends on several factors, such as molecular structure, degree of polymerization, or doping of the polymer. Typically, the band gap of semiconducting polymers lies in the range of 1.5-3.0 eV. [20] For P3HT studied in the present thesis, the value is around 1.9-2.0 eV. [38]

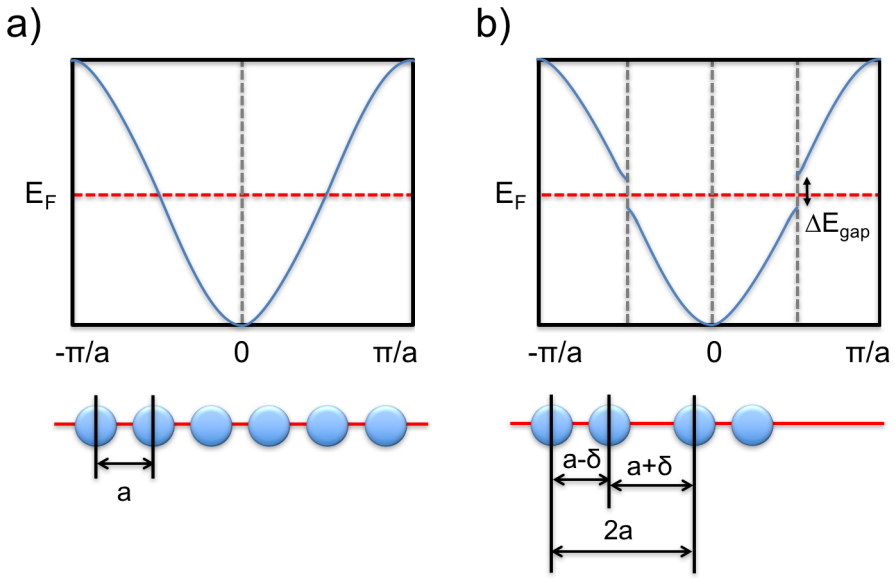

Figure 2.6: Schematic illustration of polymer band structure derived from Peierl's theorem: (a) band structure of a one-dimensional metal chain along with a periodic atom distance of a, (b) band structure of dimerized chain with a super-structural atomic distance of $2a$.

Charge carriers

In contrast to inorganic systems where charge is carried by electrons or holes, charge carriers in conductive polymers consist of quasiparticles which account for both, charge and lattice distortion. The atoms in polymer chains are able to move more freely in comparison to inorganic lattices, so the lattice distortion in polymers cannot be neglected. The chain conformations in polymers can generally lead to stronger polarization effects. Solitons, polarons, and bipolarons are the three types of quasiparticels with an energetically degenerate ground state in conductive polymers. In Figure 2.7, these three types of quasiparticles are schematically illustrates using polyacetylene (PA) as an example. Although the quasiparticles are represented as symbols at fixed positions, in reality they are more freely extended over several atoms due to chain relaxation. For example, a soliton in PA is distributed over 14 carbon atoms and possesses six times the effective mass of an electron. As shown in in Figure 2.7a, solitons with charge are spin-zero whereas neutral solitons have half-integer spin. Charged solitons can be created either via doping or via light excitation, where the latter one contributes to the photoconductivity in polymers. In contrast, polarons are charged and have half-integer spin while bipolarons are charged and spin-zero. The combination of two neutral solitons will result in annihilation. However, the combination of a neutral and a charged soliton will lead to the formation of a polaron.

Doping

Unlike in inorganic system where doping is carried out by the replacement of lattice atoms with dopants, polymers are doped via reduction or oxidation. For example, iodine is typically used as an oxidizer to dope PA and P3HT due to its high oxidation potential. [39, 40] In the case of neutral solitons, the oxidation by iodines will take the electron and lead to the formation of charged solitons.

2.1.6 Optoelectronic properties

Organic optoelectronic devices, such as organic solar cells, are a kind of device that can convert light into electricity. In general, the light absorbing layer (active layer) in organic photovoltaics consists of at least one polymeric material as a light absorber. In the present thesis, the diblock copolymer P3HT-*b*-PS:PCBM bulk heterojunction (BHJ) blend is selected as a model system, which employs the conjugated diblock copolymer as an electron donor and the small molecule PCBM as an electron acceptor. The basic principle of light-electricity conversion in BHJ blend is schematically illustrated in Figure 2.8, which

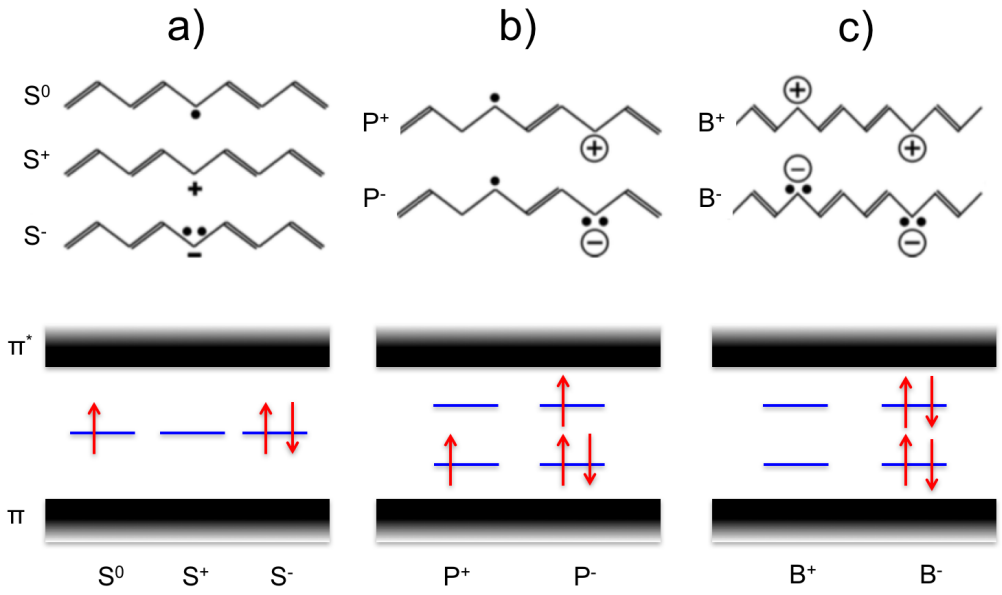

Figure 2.7: Schematic illustration of the quasiparticles with their respective energetic states in an exemplary system of PA: (a) solitons, (b) polarons, and (c) bipolarons. Dots represent electrons that are not a part of a π-bond. $\oplus$ and $\ominus$ indicate the net charge of the quasiparticles.

includes a) light absorption, b) exciton diffusion, c) exciton dissociation and d) charge transportation. Herein, only the first three processes correlating to the present thesis are discussed in sequence.

Light absorption

The solar energy conversion process starts with light absorption. A photon can be absorbed by the photo-actively functional layer on the condition of $E > E_g$, thereafter an electron is excited from the HOMO level to the LUMO level in the conductive polymer. Simultaneously, a so-called Frenkel exciton, i.e. an electron-hole pair, is created in the polymer phase. In contrast to the Wannier-Mott excitons in inorganic semiconductors, excitions in organic molecules exhibit higher binding energy on the order of 0.5-1.0 eV. [41,42] As a consequence, the exciton cannot dissociate into charge carriers at room temperature and additional forces are required. For example, PCBM in the studied system exhibits a different LUMO level compared to P3HT and therefore a potential difference can be provided at the donor/acceptor interface to separate the exciton.

For organic molecules, the shape of their absorption spectrum is presented as a function of wavelength and determined by the type of monomer. Unlike inorganic semiconductors, the absorption spectrum of organic molecules not only consists of a sharp peak but also ex-

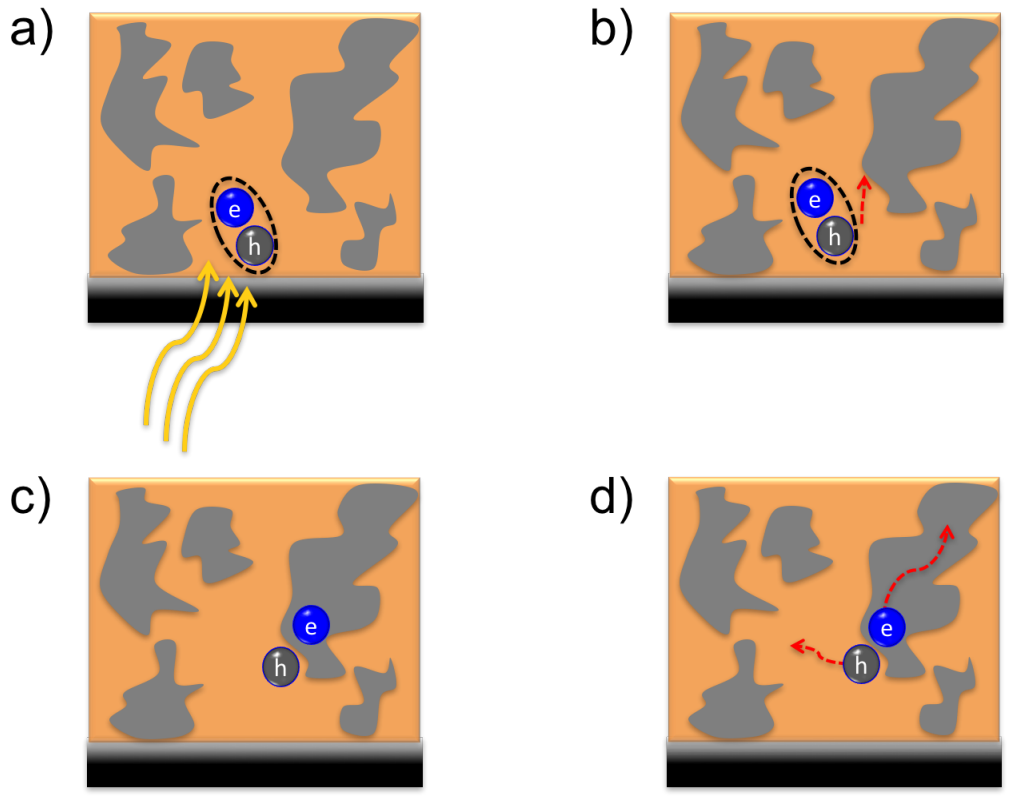

Figure 2.8: Schematic illustration of the solar energy conversion process in a BHJ blended film: (a) light absorption and exciton generation, (b) exciton diffusion, (c) exciton dissociation and (d) charge transportation. The bottom dark block depicts the substrate used for BHJ film deposition.

hibits further fine structures due to vibrational excitations. Based on the Franck-Condon principle, the electronic transition is much faster than the motion of the nucleus. Accordingly, the electronic transitions are considered as vertical lines normal to the vibrational states. In organic molecules, transitions to different vibrational states n are possible due to the spatial displacement $\triangle Q$. More specifically, the transition probability is determined by the overlap of wavefunctions of the initial and the final state. A schematic description for the transition process is illustrated in Figure 2.9. Once a photon with certain energy $h\nu$ is absorbed by the organic molecules, an excitation process occurs from the vibrational ground state of $m = 0$ in the lower electronic level l to the vibrational state of $n = 1$ in the higher electronic level u. Afterwards, the excited electron can transit to the vibrational ground state $n = 0$ in the same electronic level in form of non-radiative relaxation. The relaxed electron thereafter might then transits to the initial electronic level. At the same time, a photon is emitted with a frequency of ν^*. So far, only the singlet exciton is discussed since it dominants the transition process.

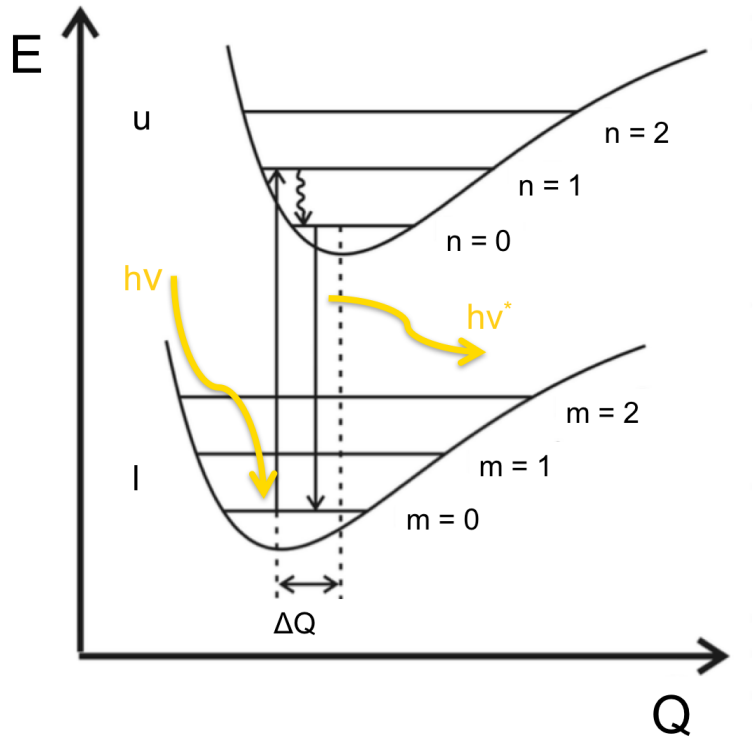

Figure 2.9: Band profile of a molecule with spatial displacement $\triangle Q$ between a lower (l) and an upper (u) electronic state. The vibrational states in the corresponding electronic states of l and u are denoted as m and n, respectively. E describes the energy whereas Q is a displacement coordinate.

For conjugated polymers, the absorption position is determined by the intrachain ordering, i.e. the conjugation length, which describes the length of the conjugated portion in the polymer chain. The conjugation length is affected by defects or kinks along the polymer backbone. Additionally, the interchain interaction among polymer chains can also influence the shape of the absorption spectrum. In the case of two polymeric chains close to each other, the electronic excitations are coupled in the vibrational modes of the molecules and consequently the absorption spectrum is affected by the type of molecular aggregation. In general, the major types of aggregates are so-called as J- and H-aggregates. For J-aggregates, dipoles align in-line whereas H-aggregates possess parallel dipoles. [43] In literature, it was reported that the conjugated polymer P3HT can be regarded within the H aggregate model. Therefore, by determining the relavent absorbance of the 0-0 and 0-1 vibronic peaks, one can address the free exciton bandwidths of W [44]

$$\frac{A_{0-0}}{A_{0-1}} = \frac{n_{0-0}}{n_{0-1}} \left(\frac{1 - 0.24 \frac{W}{E_p}}{1 + 0.073 \frac{W}{E_p}} \right)^2 \tag{2.21}$$

where n_{0-i} are the real parts of the refractive index at the corresponding absorption bands and E_p is a constant value of the phonon energy of the electronically excited state. For P3HT, E_p was reported to be 0.18 eV whereas the relevant refractive index was assumed to be around 1. [44] Generally, the free exciton band widths W decrease with increasing conjugation length. [45]

Exciton diffusion

As discussed in the previous section, the generated exciton can not dissociate into free charge carriers at room temperature due to its large binding energy. Therefore, exciton have to diffuse towards the donor/acceptor interface at which a potential differences are provided. The exciton diffusion process can be considered as a energy transfer process between donor and acceptor molecule. In the case of polymers, the donor molecule is the site where excitons are located and the acceptor molecule is the site toward where excitons are transferred. Two types of energy transfer processes are considered for conjugated polymers depending on the distance between donor and acceptor molecule, namely the trivial energy transfer process (Figure 2.10a) and the Förster resonant energy transfer process (Figure 2.10b).

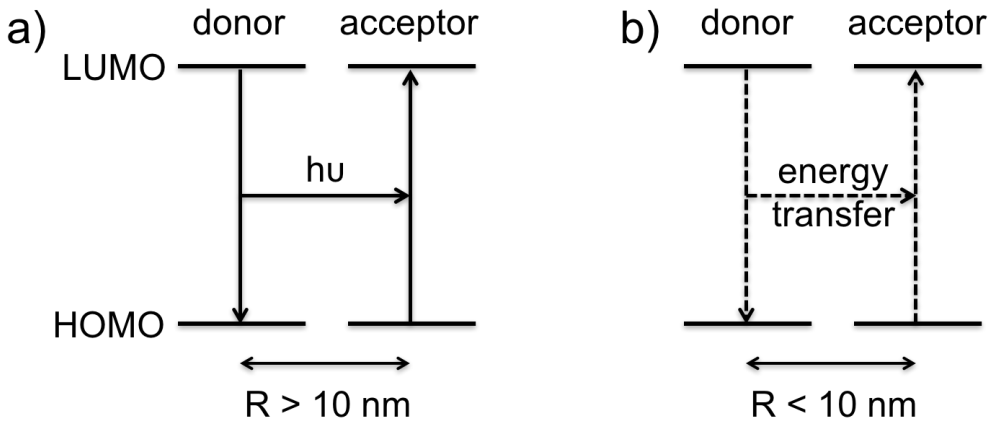

Figure 2.10: Sketches of band diagrams describing (a) the trivial energy transfer process and (b) the Förster resonant energy transfer process.

The trivial energy transfer process dominates at larger distances between donor and acceptor molecule ($R > 10$ nm). It represents a photon re-absorption process in which

a photon is emitted by fluorescence in the donor molecule and subsequently absorbed by the acceptor molecule. Afterwards, a new exciton is created in the acceptor molecule. The transfer rate $K_{D\to A}^{ET}$ of the trivial energy transfer process is

$$K_{D\to A}^{ET} \propto R^{-2} \tag{2.22}$$

where R is the distance between donor and acceptor molecule. The re-absorption process can be analogous to excitation transference among molecules and therefore the exciton lifetime is extended. [37]

The Förster resonant energy transfer process, which is also known as fluorescence resonance energy transfer (FRET), is a radiationless process that generally occurs at smaller distances between donor and acceptor molecule ($R < 10$ nm). It processes by dipole-dipole coupling. The transfer rate $K_{D\to A}^{FRET}$ for this radiationless process is

$$K_{D\to A}^{FRET} = \frac{1}{\tau_D}(\frac{R_0}{R})^6 \tag{2.23}$$

where τ_D is the natural lifetime of the donor and R_0 the critical transfer distance at which the energy transfer rate matches the radiative decay rate τ_D^{-1}. The transfer rate correlates to the dipoles orientation of the donoar and acceptor molecules. The transfer rate $K_{D\to A}^{FRET}$ is maximized on the condition of parallel dipoles of the donor and acceptor molecules.

The exciton diffusion process consists of several energy transfer steps, which can be regarded as directional randomly hopping-like motion. The effective moving distance or diffusion length l_D is comparably smaller than the total moved distances. l_D is described as

$$l_D = \sqrt{Z D\, \tau_D} \tag{2.24}$$

where Z is a parameter describing the dimensionality of the diffusion, D denotes the diffusion coefficient and τ_D depicts the exciton lifetime. For P3HT, l_D is on the order of 4-12 nm. [46, 47]

Exciton dissociation

In order to create free charge carriers, exciton dissociation process takes place at the donor/acceptor interface. Literally, excitons can be generated in both, donor and acceptor materials. Since the absorption spectrum of P3HT is overlapping more with the solar spectrum as compared to PCBM, in the present thesis P3HT is considered to be matrix in which the exciton is created. Due to the energy levels, P3HT is regarded as the electron donor whereas PCBM is the electron acceptor.

Once an exciton reaches at an donar/acceptor interface, the exciton dissociation process occurs in two ways: a direct charge transfer or an initial energy transfer followed by a charge transfer. In either case, the positive and negative charge carriers in the donor and acceptor phases exist as a Coulomb-bound polaron pair. To obtained free charge carriers, separation of the polar pair is necessary. The Braun-Onsager model is generally applied to explain the polaron pair dissociation, in which an external electric field is considered to assist the separation of the Coulomb-bound pair of charges. [48, 49] The bounded polaron pair can either dissociate with a rate of k_d or recombine back to the ground state with a rate of k_f. Meanwhile, it is also possible that free polarons can reform a polaron pair with a rate of k_r. The polaron pair separation yield P_F is given by

$$P_F = \frac{k_d(F)}{k_d(F) + k_f} \tag{2.25}$$

with the field-dependent dissociation rate as

$$k_d(F) = \frac{3\gamma}{4\pi r_{pp}^3} exp(-\frac{E_b}{kT}) \frac{J_1(2\sqrt{-2b})}{\sqrt{-2b}} \tag{2.26}$$

with γ is the Langevin recombination factor, [37] r_{pp} the initial polaron-pair radius, E_b the Coulombic binding energy, kT the thermal energy, J_1 the first order of Bessel function and b the reduced field. Taking into account the charger carrier mobility of μ, $k_d(F)$ in equation 2.25 can be rewritten as

$$P_F = \frac{\kappa_d(F)}{\kappa_d(F) + (\mu\tau_f)^{-1}} \tag{2.27}$$

where $\kappa_d(F) = k_d(F)/\mu$ and τ_f is the polaron-pair life time. [50] Therefore, the polaron-pair separation yield $P(F)$ strongly correlates to the charge carrier mobilities μ and the polaron-pair lifetime τ_f. For a system with high charge carrier mobility and long lifetime, the charge carrier generation process is quite efficient. [50] In the case of the P3HT:PCBM blend system, the exciton dissociation process is as fast as 10 fs. [51]

2.2 Organometal halide Perovskite basics

The nomenclature Perovskite initially described a calcium titanium oxide mineral with the chemical formula of $CaTiO_3$. Currently, this nomenclature has been extendedly applied for materials that adopt a similar crystal structure, e.g. organometal halide perovskite materials. In this section, the theoretical background of organometal halide perovskite materials is introduced in detail in terms of spatial structure (Section 2.2.1) and opto-electronic properties (Section 2.2.2).

2.2.1 Spatial structure

The general crystal structure of organometal halide perovskite materials can be denoted as ABX_3 where the A-site is occupied by monovalent organic moieties (i.e. $CH_3NH_3^+$ (MA^+), $HC(NH_2)_2^+$ (FA^+)), bivalent metal cations at the B-site (i.e. Pb^{2+}, Sn^{2+}), and halides (i.e. Cl^-, Br^-, I^-) at the X-site. Due to their intrisic optoelectronic properties that offer a multitude of possibilities based on composition, organometal halide perovskite materials attract increasing attention in applications of solar cells, light-emitting diodes and optical gain medias. [52–54]

3D Perovskite

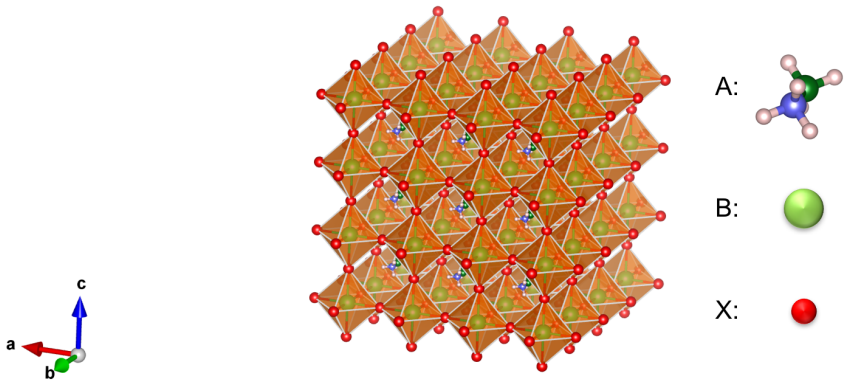

Figure 2.11: Sketch of a general perovskite crystal structure with chemical formula ABX_3.

Figure 2.11 depicts the general organometal halide perovskite crystal structure, where B occupies the center of the metal-halide octahedral $[BX_6]^{4-}$ clusters whereas A is 12-fold cuboctahedral coordinated with halide X anions. As compared to conventional perovskites, the A site in organometal halide perovskite materials contributes functionality to the structural template and solution processibility. [55] The formability of the perovskite structure can be estimated using the Goldschmidt tolerance factor t (Equation 2.28) and the octahedral factor μ (Equation 2.29) [56, 57]

$$t = \frac{r_A + r_X}{\sqrt{2}\,(r_B + r_X)} \tag{2.28}$$

$$\mu = \frac{r_B}{r_X} \tag{2.29}$$

where r_i denote the effective ionic radii of A, B and X ions. From literature, it is reported that stable perovskite can form on the condition of $0.813 < t < 1.107$ and $0.442 < t < 0.895$ [58]. Taking into account the large ionic radii of Pb (1.19 Å) and halides (e.g. bromide 1.96 Å), the ionic radius of the A cation is constrained to ≈ 2.5 Å. Therefore, only small organic molecules containing 2-3 C-C or C-N bonds, or small inorganic cations such as Cs^+ (1.88 Å) are considered to meet the requirement of forming 3D perovskite structure. [59]

Low-dimensional layered Perovskite

In contrast to the 3D perovskite, the Ruddlesden-Popper layered perovskite with the general chemical formula $(RNH_3)_2A_{n-1}B_nX_{3n+1}$ can form when the applied cations (R; e.g. C_mH_{2m+1}; m = 4-12) are too large to fit in the cuboctahedral cavity between the $[BX_6]^{4-}$ octahedra. [60] To accommodate these larger cations, the 3D symmetric growth of the cubic structure is terminated and sliced along the (001) or (110) direction (Figure 2.12a). As a consequence, pure 2D layered ($n = 1$) or quasi-2D (n = defined integer) layered structure are formed. Schematic illustrations of layered perovskite structures are depicted in Figure 2.12b-d. The interlayer spacing increases with increasing chain length of the larger organic cations. Moreover, the hydrogen bonding between the amine and the terminal halides strongly directs to the orientation of the layered perovskite. [59] The higher-order inorganic lead halide layers are held together by van-der-Waals forces and generally are multidimensional, as their dimensional structure lies in between 2D and 3D.

2.2.2 Optoelectronic properties

Organometal halide perovskite materials have gathered remarkable attention as a photo-active material for optoelectronic applications. A power conversion efficiency over 20 % has been achieved in organometal halide perovskite-based solar cells, [61] which benefits from its intrinsic photophysical properties, such as a large absorption coefficient, [62] low trap-related recombination rates, [63] and long charge-carrier diffusion lengths in the micrometer range. [64] In the following, the band gap tunability of organometal halide perovskite materials is discussed, followed by the charge carrier recombination mechanism and the quantum confinement phenomenon in layered perovskite materials.

Band gap tunability

Organometal halide perovskite materials are a kind of direct band gap semiconductor. As for $MAPbI_3$, the valence band maximum at the reciprocal symmetry point is formed by

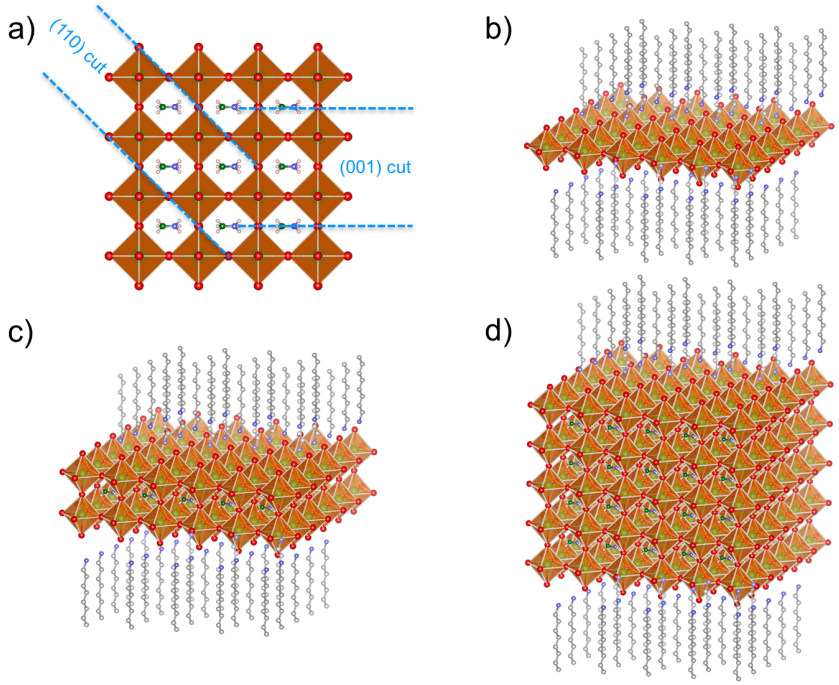

Figure 2.12: a) Sketch of the dimensionally slicing options for 3D perovskite crystal. Schematic illustration of low-dimensional layered perovskite with b) a single layer of $[BX_6]^{4-}$ octahedra, c) 1 unit perovskite cell, and d) 4 unit perovskite cells along the terminated crystal growth direction.

anti-bonding states derived from hybridization of the $5p$ orbitals of iodine and $6s$ orbitals of lead, whereas the conduction band minimum is mainly constituted by the empty $6p$ orbitals of lead. [63] Notably, the band gap in these perovskite materials can be steadily tuned during synthesis by either partial substitution of the cation or by controlling the mixed halide stoichiometry. As a consequence, the absorption spectrum of perovskite is extended.

It has been demonstrated that the band gap of $MAPbX_3$ gradually decreases from 3.11 eV, to 2.3 eV and to 1.55 eV along the line of using Cl^-, Br^-, and I^- at the X sites. [65] This is also in agreement with calculation results which suggested that substitution of the bigger atomic size of halides will lead to a decrease in the band gap. Comparably, this trend is also applicable to substitution of the organic cations, that is, the band gap of $MAPbI_3$ decreases from 1.6 eV to 1.5 eV when replacing a MA cation with the larger-radius FA. [66] As compared to MA, FA is more likely to form hydrogen bonds with the lead iodide matrix, which in turn decreases the propensity for octahedral tilting. As a

consequence, the lead character of the conduction band states enhanced in the Pb-I bond and therefore amplifies the effect of spin-orbit coupling.

Charge carrier recombination

Upon photoexcitation, the generated exciton is composed of a Coulomb-bond electron-hole pair. The strength of this attractive bond is analogous to the hydrogen Rydberg (Ry(H)) and is described by the exciton binding energy (E_b)

$$E_b = \frac{m_r e_0^4}{2\hbar^2(4\pi\varepsilon\varepsilon_0)^2}\frac{1}{n^2} = \frac{(m_r/m_0)}{\varepsilon^2}\frac{1}{n^2}Ry(H) \tag{2.30}$$

with the associated exciton Bohr radius (r_b) which is given by

$$r_b = \frac{\hbar^2(4\pi\varepsilon\varepsilon_0)}{m_r e_0^2} = \frac{\varepsilon}{(m_r/m_0)}a_B \tag{2.31}$$

where m_r is the reduced effective mass, e_0 the elementary charge, ε_0 the permittivity of free space, ε the dielectric constant of the host material, $n \geq 1$ the integer of excitonic states, and a_b the Bohr radius of the hydrogen $n = 1$ state. Excitons in conjugated polymers are tightly bounded with small Bohr radii and therefore additional effort is needed to dissociate excitons into free charge carriers at room temperature, e.g. morphological nanostructuring. Contrarily, low E_b excitons with spatially delocalized radii that are much greater compared to the host lattice are known as Wannier-Mott excitons. After diligent research efforts in the past five years, it is now firmly established that in perovskite materials, excitons formed after photoexcitation behave like Wannier-Mott excitons and spontaneously dissociate into free electrons and holes. [67–69] The various photophysical processes in perovskite materials are illustrated in Figure 2.13.

The dynamics of charge carrier recombination through monomolecular and/or higher-order processes are determined by

$$\frac{dn}{dt} = G - k_1 n - k_2 n^2 - k_3 n^3 = G - nR_T(n) \tag{2.32}$$

where k_1 is the monomolecular charge recombination rate constant, k_2 the bimolecular electron-hole recombination rate constant, and k_3 the Auger recombination rate constant, G represents the charge-density generation rate, n denotes the charge carrier density, and $R_T(n)$ is the total charge recombination rate described by

$$R_T = k_1 + nk_2 + n^2 k_3 \tag{2.33}$$

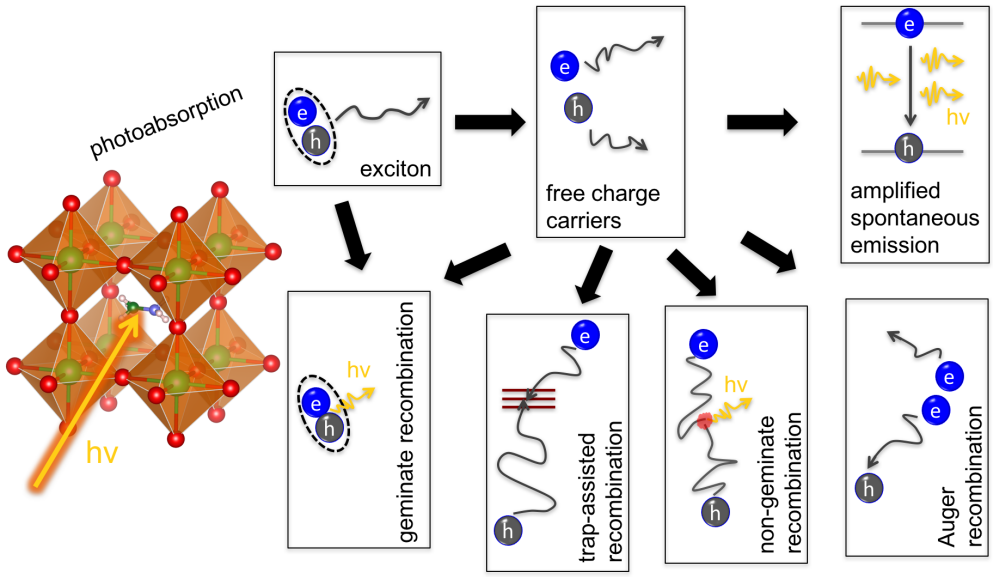

Figure 2.13: Schematic illustration of the various photophysical processes in perovskite materials upon photoexcitation.

Monomolecular charge carrier recombination in organometal halide perovskite most probably originates from trap-assisted recombination. It has a strong dependence on the trap cross-section, energetic depth, density, and distribution characteristics, which are closely related to the processing condition. The exact nature of trap states in organometal halide perovskite materials is still under investigation. For perovskite thin films, it is established that the trap densities might be significantly larger at grain boundaries, making the trap-assisted recombination linked to crystallite size. [54]

Bimolecular recombination has a lower dependence on the processing conditions than trap-assisted recombination. The relatively weak preferential localization of electrons and holes in different regions of the perovskite unit cell causes reduced spatial overlap of wave functions of electron and hole, and therefore lowers the recombination rates. [70] But a better understanding of bimolecular recombination mechanism in perovskite materials is still necessary.

Auger recombination is a many-body process including recombination of an electron and a hole, associated with energy and momentum transfer to another electron or hole. A Spin-off band originating from spin-orbit coupling is generally involved in efficient Auger recombination. Auger recombination depends on the charge carrier density as described by k_3 in Equation 2.32 and strongly depends on the electronic band structure.

Amplified spontaneous emission

As shown in Figure 2.14 a, the excited electron upon photoabsorption may decay to a lower energy state without any external influence and emitting a photon. This process is called spontaneous emission (SE). The created photon exhibits no phase relationship with the incident photon. Stimulated emission is the process in which matter lose energy due to preturbation by a photon and resulting in the creation of another photon. The created photon exhibits the same phase, frequence and polarization in comparision to the perturbing photon (Figure 2.14b). For an optical gain medium, population inversion can be generated by an external stimulation (e.g. photopumping), in which, fluorencence gained in intensity due to stimulated emission accompanied by the PL spectra narrowing results from the amplified spontaneous emission (ASE). g_0 is the signal gain that connected to the population inversion [71]

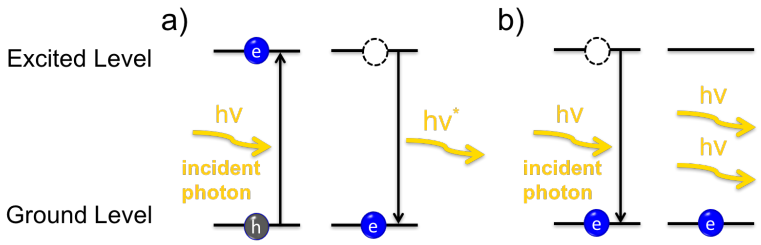

Figure 2.14: Schematic illustration of a) spontaneous emission and b) stimulated emission processes.

$$g_0 = exp[d(N_0\,\sigma_{em} - (N_{dop} - N_0)\,\sigma_{abs})] \tag{2.34}$$

where N_0 is the initial excitation density of the laser active ions in the active material, d the thickness, σ_{em} and σ_{abs}, the emission and absorption cross sections for the laser wavelength of a monochromatic laser beam, and N_{dop} the doping concentration of the active material. Typically, a loss term L accounting for the reduction of the gain due to impurities or re-absorption should be included

$$L = 1 - exp[-N_{dop}\,\sigma_{abs}\,d] \tag{2.35}$$

which leads to a comprehensive description of g_0 as

$$g_0 = (1 - L)\,exp[N_0\,d\,(\sigma_{em} + \sigma_{abs})] \tag{2.36}$$

ASE provides an avenue to understand the dominant recombination pathways in perovskite materials. A standard emergence of ASE behavior of perovskite materials under different excitation fluence is showed in Figure 2.15. At low excitation fluence, only SE is observed. Along with an increases in the excitation intensity, a second sharp PL peak with narrower FWHM arises after certain fluence threshold is surpassed, which can be assigned to the ASE peak. The gain originates from the transition from occupied excited electronic states to the ground state (Figure 2.15). The bathochromic shift of the ASE peak is caused by parasitic self-absorption on the high-energy side of the SE, [54] and the energy of the stimulated emission must be lower than the chemical potential of the plasma. [72] Non-radiative processes are believed to diminish the optical gain. A low-threshold ASE indicates that radiative recombination processes compete with Auger recombination following trap saturation.

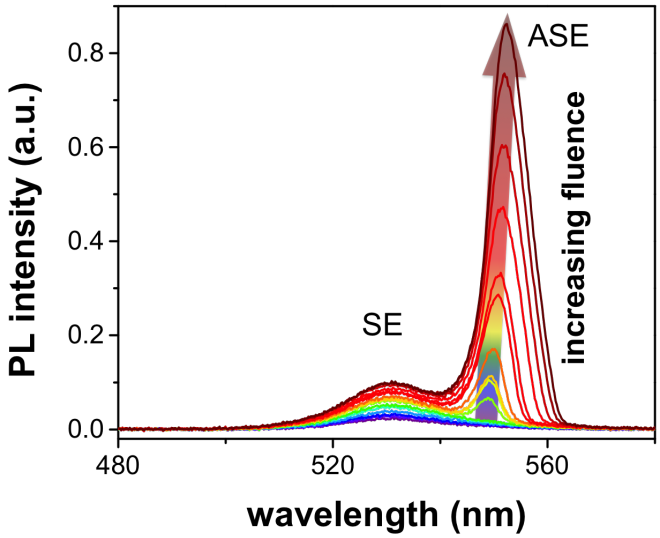

Figure 2.15: PL spectra of a organometal halide perovskite thin film excited with different pumping intensities. SE and ASE peaks are marked in the spectra.

Quantum confinement

In the low-dimensional layered perovskite materials, the dielectric mismatch between the inorganic and organic layers is expected to alter the optical and charge transportation properties as compared to 3D perovskite materials. The organic layer surrounding the perovskite layer contributes a strong confinement energy. Depending on the size of the nanostructure d and the exciton Bohr raidus r_b, two major regimes can be defined. On the condition of $d \gg r_b$, electron and hole bound in a pair to form an exciton. Whereas

for $d \ll r_b$, electron and hole need to be treated as separated particles and this regime is also called the strong confinement regime.

In 3D perovskite, the Coulomb interaction between the electron and hole is greatly screened. Upon decreasing the layered perovskite thickness, the dielectric constant becomes lower as an increasing amount of electric field lines between charge carriers are outside the perovskite, therefore eliminating the screening and strongly enhancing the exciton binding energy. The band gap of layered perovskite can be theoretically estimated by

$$E_g \approx E_{g,DFT}^{3D} + \sum^{3D} + \delta E_{g,DFT}^{2D} + \delta \sum^{2D} \tag{2.37}$$

where $E_{g,DFT}^{3D} + \sum^{3D}$ is the 3D perovskite band gap, and $\delta E_{g,DFT}^{2D}$ represents the quantum confinement effect as well as lattice distortions in the layered perovskite materials.

2.3 Scattering methods

As a complementary method to various real space characterization techniques such as microscopy, scattering methods using X-rays or neutrons are employed to reveal the morphological information in the semiconductor thin films. The information extracted from scattering methods is obtained from the full film volume, which has a higher statistical relevance as compared to the fractional information acquired on the sample surface. Firstly, the basic physical background is explained (Section 2.3.1) and followed by detailed discussions of X-ray reflectivity (Section 2.3.2) and X-ray diffraction (Section 2.3.3). Afterwards, grazing incidence scattering is addressed (Section 2.3.4), which including detailed explanations of the applied GIWAXS, GISAXS and GISANS techniques.

2.3.1 Basic principles

To guarantee a successful scattering experiments, the variation of scattering contrast is necessary since homogeneous media do not scatter. The propagation of an electromagnetic wave through a medium is described by the Hemholtz equation [73]

$$\triangle \vec{E}(\vec{r}) + k^2 n^2(\vec{r}) \vec{E}(\vec{r}) = 0 \tag{2.38}$$

where $\vec{E}(\vec{r})$ is the electron magnetic wave vector depending on the the position vector ($\vec{r}$), k is the modulus of the wave vector, i.e. $k = |(\vec{k_i})| = 2\pi \ / \ \lambda$ with the wavelength λ, and $n(\vec{r})$ is the position dependent refractive index, which can be described as [74]

$$n(\vec{r}) = 1 - \delta(\vec{r}) + i\beta(\vec{r}) \tag{2.39}$$

depending on the dispersive part $\delta(\vec{r})$ and absorption part $\beta(\vec{r})$. In case of X-rays, the scattering is caused from changes in the mean electronic density and the dispersion is

$$\delta(\vec{r}) = \frac{\lambda^2}{2\pi} r_e \, \rho(\vec{r}) \sum_{j=1}^{N} \frac{f_j^0 + f_j^{'}(\lambda)}{Z} \tag{2.40}$$

and absorption contribution is

$$\beta(\vec{r}) = \frac{\lambda^2}{2\pi} r_e \, \rho(\vec{r}) \sum_{j=1}^{N} \frac{f_j^{''}(\lambda)}{Z} \tag{2.41}$$

which depends on the classical electron radius $r_e = e^2/(4\pi\epsilon_0 mc^2)$ and the position dependent electron density $\rho(\vec{r})$. [75, 76] The summation is expressed over N atoms per unit volume with Z referring to the number of electrons in the unit volume and $f_j = f_j^0 + f_j^{'}(\lambda) + f_j^{''}(\lambda)$ is the expression of the forces oscillator strength of the atom j. [73] For X-rays, f_j^0 can be approximated by the number of electrons of the atom j.

In case of neutrons, the scattering is caused by variations of the mean scattering length within the probed medium and the dispersion is

$$\delta = \frac{Nb\lambda^2}{2\pi} \tag{2.42}$$

and absorption contribution is

$$\beta = \frac{N\alpha_a\lambda}{4\pi} \tag{2.43}$$

with the atomic number density N, the coherent scattering length b, the absorption cross-section for neutrons α_a and the scattering length density (SLD) Nb. In general, for hard X-rays, the dispersion δ is on the order of 10^{-6} whereas the absorption β is on the order of 10^{-8}. In the case of neutrons, the dispersion δ is on the order of 10^{-6} and the absorption β is on the order of 10^{-12}. [73] Therefore, the absorption part is only a minor contribution for neutrons.

In Figure 2.16 the principle scattering setup is presented. The incident beam $\vec{k_i}$ impinges on the sample surface under a shallow incident angle α_i. The exit beam $\vec{k_f}$ can be described by the exit angle α_f (in the xz-plane) and the out-of-plane angle ψ (in the xy-plane), whereas the transmitted beam $\vec{k_f}$ exits at a angle of α_t. The momentum transfer which is also known as the scattering vector $\vec{q}$ is defined by

$$\vec{q} = \vec{k_f} - \vec{k_i} \tag{2.44}$$

In this thesis, only elastic scattering is considered and thus, the scattering vector $\overrightarrow{k}$ only describes a change of direction of the beam whereas its modulus is preserved. With respect to the angels being measured from the surface of the boundary, Snell's law, which describes the relation of the incident and final beam propagating though two mediums of different refractive indexes, can be rewritten as

$$n_0 cos(\alpha_i) = n cos(\alpha_t) \tag{2.45}$$

since $\delta > 0$, the refractive index $n < 1$, which means that a total external reflection occurs when the incident angle α_i is smaller than the critical angle α_c. In case of X-rays, α_c is calculated from the dispersion part δ of the refractive index of the material [77]

$$\alpha_c(\lambda) = \sqrt{2\delta(\lambda)} \tag{2.46}$$

and in case of neutrons from the scattering length density of the material ρ as function of wavelength λ

$$\alpha_c(\lambda) = \lambda\sqrt{\frac{\rho}{\pi}} \tag{2.47}$$

The penetration depth is defined as the depth at which the intensity of the beam is reduced to 1/e of its original intensity ($\approx$ 37 %). Since the beam is also scattered inside the medium, a so-called escape depth should be considered as a second dampening occurs on the way out of the medium. Therefore, the scattering depth Λ is approximately half of the penetration depth of most materials. [78, 79] Λ is on the order of 50 Å in the case of $\alpha_i < \alpha_c$, while it significantly increases when $\alpha_i = \alpha_c$. In the case of $\alpha_i > \alpha_c$, Λ can be as large as several hundreds of nanometers, which is merely limited by the absorption.

2.3.2 X-ray reflectivity

X-ray reflectivity (XRR) is an ideal method to investigate the vertical composition distribution in thin films. During measurement, the specular scattering is probed as a function of the incidnet angle α_i, i.e. $\alpha_i = \alpha_f$ whereas $\psi = 0$. As a consequence, only the z-component of the scattering factor q_z (equation 2.48) is changed. [73]

$$q_z = \frac{4\pi}{\lambda} sin(\alpha_i) \tag{2.48}$$

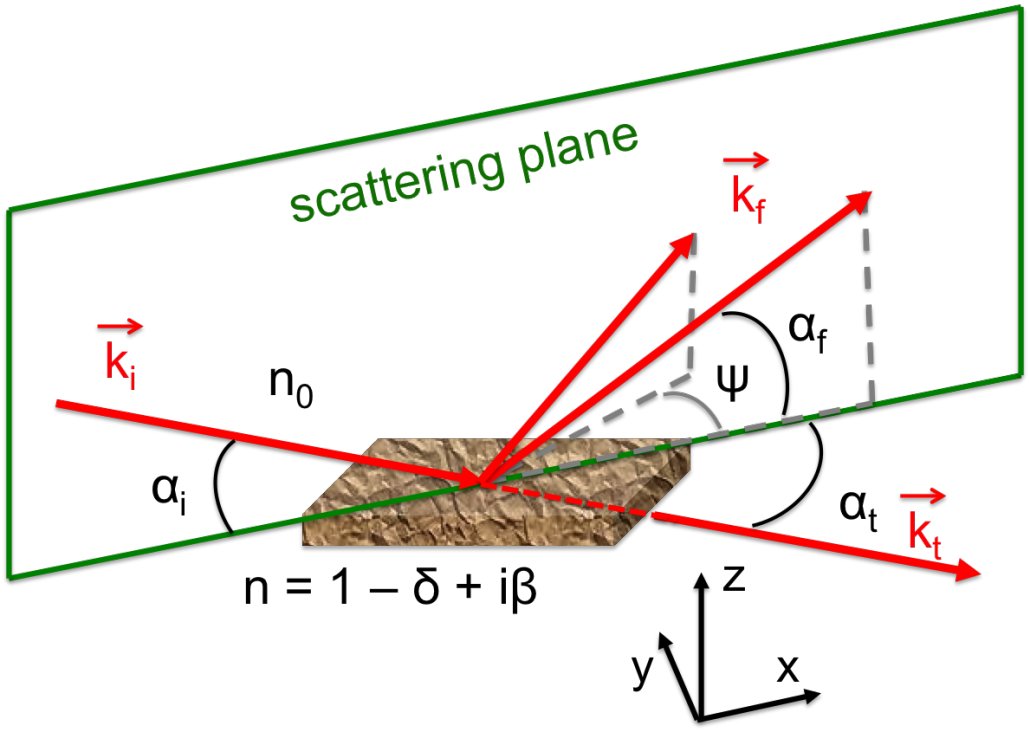

Figure 2.16: Definitions of directions and angles of a principle scattering setup. $\vec{k_i}$, $\vec{k_f}$ and $\vec{k_t}$ describe the incident, exiting and transmitted beam, respectively. The incident angle α_i and exit angle α_f lie in the scattering plane whereas ψ in the sample plane and α_t depicts the angle of the transmitted beam.

Accordingly, the electron density distribution normal to the sample plane is recorded. At a single interface between two materials with respective refractive index n, the incident beam is partly reflected and partly transmitted as described by Equation 2.45 in Section 2.3.1. The amplitudes of the transmitted and reflected beam are given by the Fresnel reflection coefficent r^F and the Fresnel transmission coefficient t^F. Based on this, the reflectivity and transmittivity are defined by the square of the corresponding coefficient [73]

$$R^F = |r^F|^2, T^F = |t^F|^2 \tag{2.49}$$

However, the polymer thin films studied in the present thesis typically exhibit compositional differences at the interface close to the air with respect to the interface close to the substrate. Therefore, an approach developed by Parratt using a recursive algorithm is necessary to describe the reflectivity. [80] Within this model, N stacked layers with a defined refractive index $n_j(z)$ and thickness d_j are applied to represent the vertical film composition. These stacked layers are sandwiched between an infinitely thick layer of air

on the top side and a glass or silicon substrate on the bottom side. For each interface between layer j and layer $j+1$ the ratio of reflectivity and transmittivity is calculated by

$$X_j = \frac{R_j}{T_j} \tag{2.50}$$

where R_j and T_j are calculated by equation 2.49. In real polymer thin films, the interfaces are not ideally smooth but have certain degree of roughness. An extension of the Parratt algorithm including the Nevot-Crocet factor can be applied to account for non perfectly flat interfaces. Therefore, the root mean square roughness σ_{rms} is included in the Parratt algorithm by an exponential function to the Fresnel coefficient [81]

$$\sigma_{rms} = \sqrt{\frac{1}{N_{\sigma_{rms}}} \sum_{i=1}^{N_{\sigma_{rms}}} \Delta z_i^2} \tag{2.51}$$

where $N_{\sigma_{rms}}$ is the number of measured points alongside the interface and Δz_i is the deviation from the mean interface at the sampling point i. A theoretical description is detailed in literature. [73]

An example XRR curve is displayed in Figure 2.17. At low incident angles, the normalized intensity is unity as the total reflection condition is fulfilled ($\alpha_i < \alpha_c$). When α_i slightly increases, several intensity minimums are seen, indicating the critical angles of different materials ($\alpha_i = \alpha_c$). For $\alpha_i > \alpha_{c_{si}}$, the reflectivity curve follows a distinct decreasing with a decay of q^{-4} and so-called Kiessig-fringes are observed due to interference effects. [82] In addition, a deeper decay can resulted from roughness. The width of the Kiessig fringes is correlated with the film thickness d. Therefore, the total film thickness can be approximated by [82]

$$d \approx \frac{2\pi}{\Delta q_z} \tag{2.52}$$

Based on the aforementioned descriptions, the scattering length density profiles normal to the sample plane can be extracted by modeling the measured reflectivity curves, which are used to describe the vertical compositional variation in P3HT-*b*-PS:PCBM blend films in chapter 5.

2.3.3 X-ray diffraction

X-ray diffraction (XRD) is generally used to probe the crystalline structure on atomic length scales. A monochromatic X-ray beam with a certain wavelength is scattered at different lattice planes within a crystal. In principle, the atoms located in a crystal lattice

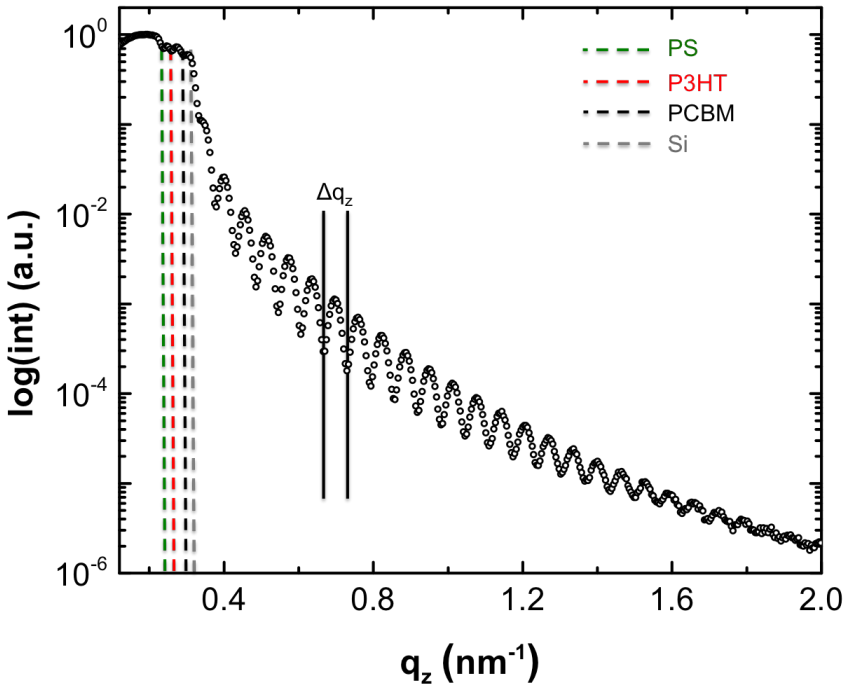

Figure 2.17: Exemplary reflectivity curve of a P3HT-*b*-PS:PCBM blend film on the silicon substrate. The dashed vertical lines indicate the crtical angles of materials PS, P3HT, PCBM and silicon. The distance between the minima of the Kissig dringes is Δq_z.

can be considered as a periodic gratings for X-rays. As shown in Figure 2.18, constructive interference or destructive interference occurs depending on the correlation between path difference s of parallel X-rays and angle θ.

For constructive interference, the scattered X-rays interfere and give rise to a intensity maximum when Bragg laws is fulfilled [83]

$$n\lambda = 2d_{hkl}\, sin(\theta) \tag{2.53}$$

where d_{hkl} is the distance between hkl-lattice planes. However, not all reflections from every lattice planes in a crystal are observable due to destructive interference, which is also called as extinction rules. The polycrystalline perovskite sample investigated in this thesis exhibits a powder-like diffraction pattern because the lattice planes are randomly orientating within the material. The powder diffraction pattern shows Bragg peaks of each lattice plane, from which the size of the crystallites can be approximated using the Scherrer equation

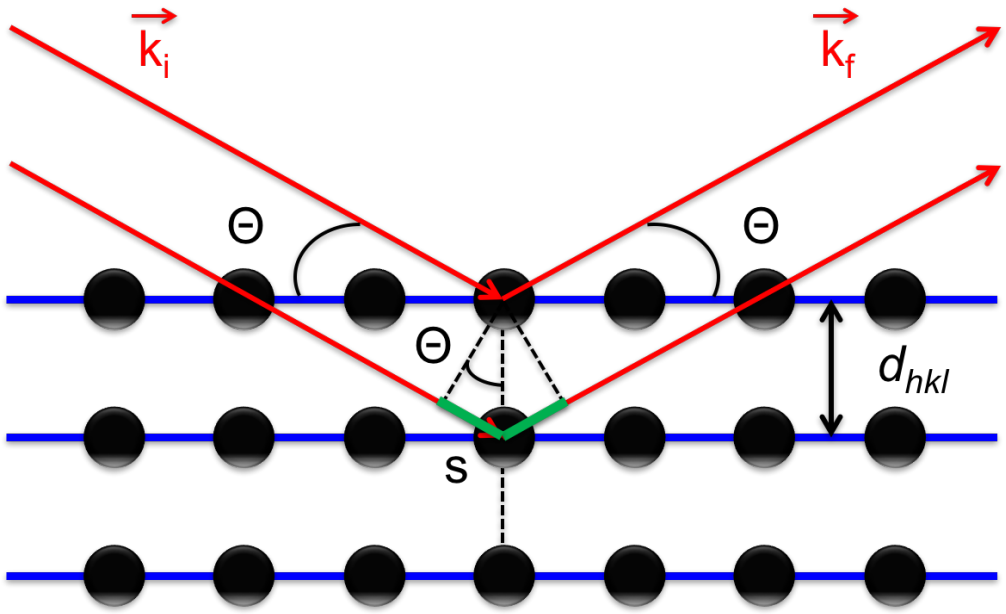

Figure 2.18: Schematic illustration of the Bragg equation. Two incoming beams $\overrightarrow{k_i}$ approach the electron clouds of the probed atoms which are located on the crystal planes (blue lines) and scattered $\overrightarrow{k_f}$. The extra path lengths of the lower beam is highlighted with green lines s, depending on the angle θ. d_{hkl} describes the periodic distance between two crystal planes.

$$D_{hkl} = \frac{K\lambda}{\delta(2\theta)cos(\theta)} \tag{2.54}$$

where $K \approx 0.9$ is the Scherrer form factor, λ denotes the applied wavelength, $\delta(2\theta)$ is the full width at half maximum (FWHM) of the Bragg peak at the angle of 2θ. [83] Upon transforming the angle θ into scattering vector $\vec{q}$, the Scherrer equation can be rewritten as

$$D_{hkl} = \frac{2\pi}{\delta\, q_{hkl}} \tag{2.55}$$

where δq_{hkl} is the integral line width of the Bragg peak that is calculated by dividing the Bragg peak by its amplitude. [84, 85] From literature, it was reported that the width of the Bragg peak is effectively interrupted by the paracrystalline order, e.g. the $\pi - \pi$ stacking in P3HT. [86] In order to decouple contributions from paracrystallinity and crystal size, the detection of higher orders of reflection peaks is necessary, which is hard to achieve for most conjugated polymer films. In addition, the resolution of the scattering setup broadens the Bragg peaks. Therefore, the Scherrer equation is only used to draw qualitative comparisons between samples.

2.3.4 Grazing incidence scattering

For morphological characterization of thin films, it is hard to obtain statistically relevant information due to the restriction of limited volume of material available for investigation. This limitation is well addressed by studying thin films under a geometry of grazing incidence scattering (GIS). A shallow incident angle of typically $\alpha_i < 1°$ is applied in GIS measurements and therefore the scattering volume is compensated with a larger footprint on the sample. The scattered intensity is captured by pixels on the two-dimensional (2D) detector. For a given sample-detector distance (SDD), each pixel corresponds to certain out-of-plane angle ψ and exit angle α_f. The scattering vector $\vec{q}$ is given by [87]

$$\vec{q} = (q_x, q_y, q_z) = \vec{k_f} - \vec{k_i} \tag{2.56}$$

with each component

$$q_x = \frac{2\pi}{\lambda}(cos(\alpha_f)cos(\psi) - cos(\alpha_i)) \tag{2.57}$$

$$q_y = \frac{2\pi}{\lambda}cos(\alpha_f)sin(\psi) \tag{2.58}$$

$$q_z = \frac{2\pi}{\lambda}(sin(\alpha_f) + sin(\alpha_i)) \tag{2.59}$$

In general, the 2D detector mostly records the q_y and q_z information whereas q_x is negligible due the small angles in GIS geometry. The q_y component can be mainly assigned to the in-plane lateral structures, and periodic structures normal to the film surface contribute scattering feature in q_z. In the next section, grazing incidence small angle scattering (GISAS) using either X-ray (GISAXS) or neutron (GISANS) as a probe is discussed including mechanisms and data analysis, followed by the introduction of grazing incidence wide angle X-ray scattering (GIWAXS).

GISAS

GISAS is used to determine the lateral morphology of thin film samples in the xy-plane (Figure 2.16). The GISAS data is generally treated within the framework of the distorted wave Born approximation (DWBA), where the scattering process is considered as a first-order perturbation of an ideal system with flat interfaces. [88,89] Thus, the roughness and lateral structures are described as perturbations and the differential cross section under a given solid angle dΩ is given by

$$\frac{d\sigma}{d\Omega}\mid_{diff} = \frac{C\pi^2}{\lambda^2}(1-n^2)^2 \left|T_i^F\right|^2 \left|T_f^F\right|^2 P_{diff}(\vec{q}) \propto P_{diff}(\vec{q}) \tag{2.60}$$

where C is the illuminated area, ${T_{i,f}}^F$ is the respective Fresnel transmission coefficients, and $P_{diff}(\overrightarrow{q})$ is the diffuse scattering factor which directly measures the scattered intensity. [75] The Fresnel transmission coefficients have the maximum value for the condition $\alpha_{i,f} = \alpha_c$, which is material sensitive and observed as the Yoneda peak in GISAS data. [90] The diffuse scattering factor $P_{diff}(\overrightarrow{q})$ can be described in terms of N identical and centrosymmetrical objects with no preferential orientation

$$P_{diff}(\vec{q}) \propto NF(\vec{q})S(\vec{q}) \tag{2.61}$$

where $F(\vec{q})$ is the form factor of each object that is derived from Fourier transformation of the object shape, and $S(\vec{q})$ denotes the structure factor that refers to the spatial distribution of objects in a one-dimensional paracrystalline lattice.

The diffuse scattering in GISAS is described by DWBA, which includes four terms of both scattering and reflection processes. That is: (i) only scattering; (ii) reflection on the substrate followed by scattering; (iii) scattering followed by reflection on the substrate and (iv) first reflection on the substrate, then scattering, and followed by another reflection on the substrate. All these four terms are included for the form factor correction. In this thesis, cylinder-like form factors are applied in modeling GISAS data due to the isotropic orientation of the studied film. In addition, a so-called local monodisperse approximation (LMA) is used to account for the object size distribution. In LMA, it is assumed that only identical objects scatter, thus objects with different form and structure factors are independent of each other. Finally, the overall scattering intensity is a sum of intensities out of all these objects. [86]

GIWAXS

In general, the GIWAXS experiment set-up is analogous to GISAXS except for a shorter SDD, thus revealing morphological information for larger q values, i.e. crystalline information. When the beam passes through a scattering medium (e.g. air), especially for the detection of wide angle scattering in grazing incidence geometry, the medium attenuation and the detector absorption need to be taken in to account. To reconstruct the actual sample morphology in reciprocal space, the analysis of the detected scatterings requires a number of corrections. Firstly, the 2D GIWAXS data is corrected by a flat field correction file that provided by the detector supplier to deal with the sensitivity difference of the individual pixel in the detector. Afterwards, a correction for the absorption efficiency on a pixel by pixel basis is carried out to resolve the medium attenuation by

$$E_m = \frac{1}{1 - exp(\mu_m SDD/cos2\Theta_i)} \tag{2.62}$$

where μ_m the linear mass attenuation coefficient of the path medium, SDD the nominal sample-to-detector distance with respect to the direct beam pixel and $2\Theta_i$ the oblique scattering angle of an individual pixel (x_i, y_i). [91,92] Thereafter, an efficiency-correction accounts for the detector absorption variation is calculated by

$$E_d = \frac{1}{1 - exp(\mu_d t_d/cos2\Theta_i)} \tag{2.63}$$

where t_d is the thickness of the pixel material in the detector. Furthermore, a solid angle correction is performed to deal with the difference in effective pixel areas for different solid angles. The detected intensity is normalized to the solid angle of the direct beam by

$$C_s = \frac{\triangle\Omega_0}{\triangle\Omega_i} = cos^{-3}(2\Theta_i) \tag{2.64}$$

where $\triangle\Omega_0$ is the solid angle of the direct beam pixel and $\triangle\Omega_i$ is the solid angel of pixel (x_i, y_i).

Since most synchrotron radiation is horizontally polarized, a polarization correction to account for changes in intensity distribution due to the beam polarization is done by

$$C_p = p_h(1 - cos^2\alpha_f sin^2\psi) + (1 - p_h)(1 - sin^2\alpha_f) \tag{2.65}$$

where p_h is the fraction of the radiation polarized in horizontal direction, α_f and ψ are the exit angle and out of plane angle.

All in all, the total correction is given by

$$corrected\,data = raw\,data * flat\,field * \frac{1}{C_p}\frac{E_m E_d}{max(E_m E_d)} * C_s \tag{2.66}$$

Compared to XRD, one advantage of GIWAXS using a 2D detector is that the preferential orientation of crystallites with respect to the film surface can be determined. For both P3HT and organometal halide perovskite materials, the understanding of crystalline orientation is important because it closely related to charge carrier transportation in films. A comparison between two identical crystalline orientations and the corresponding GIWAXS 2D data are displayed in Figure 2.19. The incident angle of α_i is kept constant for the GIWAXS measurements. As a consequence, the full q-range is not accessible. For a powder-like film (Figure 2.19a) with isotropically orientated crystallites, so-called Debye-Scherrer-like rings are detected in 2D GIWAXS pattern (Figure 2.19c). The scattered intensities are randomly distributed as a function of both $q_r = \sqrt{q_x^2 + q_y^2}$ and q_z. In

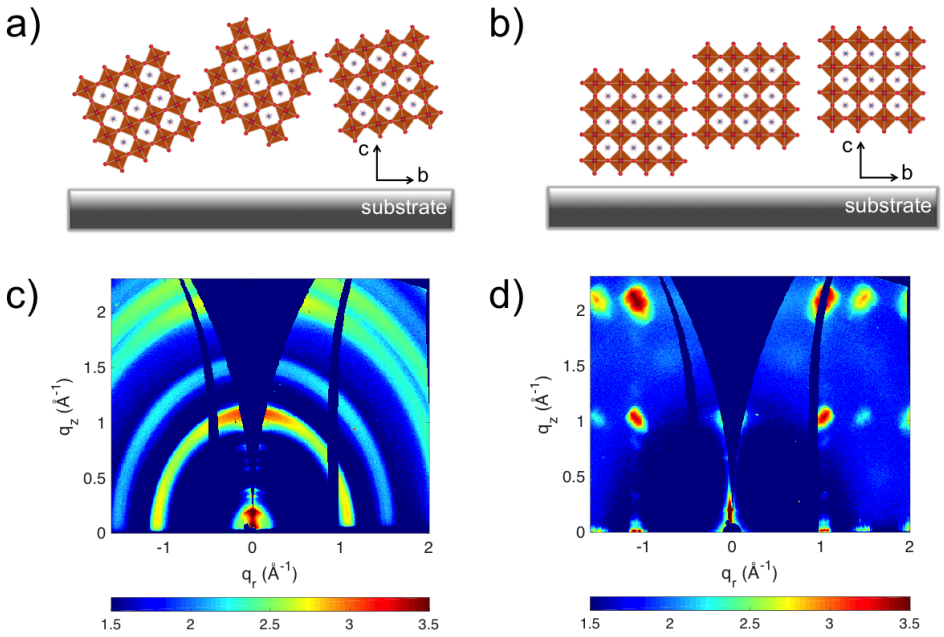

Figure 2.19: Schematic illustration of a) randomly orientated and b) highly orientated crystal morphology. Exemplary GIWAXS 2D data of c) randomly orientated and d) highly orientated polycrystalline film.

contrast, in the case of polycrystalline films with a high degree of preferential crystallite orientation (Figure 2.19b), intense Bragg peaks are revealed (Figure 2.19d). Therefore, from the arc analysis on specific lattice plane, the prominent crystallite orientations inside the film are accessible.

3 Characterization methods

To correlate the morphological properties of polymer- or perovskite-based semiconductor thin films with their optoelectronic behavior, various structural characterization techniques and spectroscopic methods are employed to examine these systems. In this chapter, all the fundamentals of the applied instruments and the corresponding data analysis principles are described.

3.1 Structural characterization

The structure of the resulting thin films is explored in both, real space and reciprocal space. Optical microscopy (Section 3.1.1), scanning electron microscopy (SEM) (Section 3.1.2) and atomic force microscopy (AFM) (Section 3.1.3) are applied to obtain direct images of surface structures in real space on different length scales. The vertical film composition and the crystalline information are determined by X-ray reflectivity (Section 3.1.4) and X-ray diffraction (Section 3.1.5), respectively. In addition, with grazing incidence scattering techniques using x-rays or neutrons (Section 3.1.6), information not only on the surface but statistically averaged over the full volume of the studied samples is achieved.

3.1.1 Optical microscopy

Optical microscopy is used to have a first quick check on surface homogeneity and surface morphology of the deposited film on the micrometer scale. An Axiolab A microscope from Carl Zeiss (Germany) is used in combination with a Pixellink USB Caputre BE 2.6 charge coupled device (CCD) camera. The surface topographic images are captured with different magnifications from 1.25 to 100x, with a corresponding pixel size from 6.258 μm to 80 nm. Each recorded image contains 1260 $\times$ 1024 pixels.

3.1.2 Scanning electron microscopy (SEM)

Scanning electron microscopy (SEM) is used to characterize the surface morphology of the perovskite films. Compared with optical microscopy, a desirable higher resolution on the nanoscale is achieved by using a wave source of electrons, which can have a much smaller wavelength with respect to that of optical light. In general, the electrons are either generated by a hot cathode or emitted from a cathode material (e.g. tungsten filament) under a strong electrical field. Afterwards, the generated electrons are accelerated by a voltage of typically several kV and are subsequently focused by different magnetic focusing lenses. Samples are line-wise probed by the electron beams, during which secondary electrons as well as backscattering electrons that are emitted from the sample surface are captured by the detector. In this way, a microscopic image containing different topographic changes is recorded. The signal intensity is determined by the electron conductivity of the probed samples as well as the sample-detector distance. Therefore, polymer materials appear darker on the image compared to conductive materials, such as organometal halide perovskite. However, for the latter one, due to restrictions by the electron beam irradation damage, it is difficult to acquire any local information with a lateral resolution below 20 nm. [93]

A Gemini Ultra Plus field emission scanning electron microscopy (FESEM) from Zeiss (Germany) is used to obtain the SEM images. All the measurements were carried out at the chair of Prof. Jochen Feldmann, Lehrstuhl für Photonik und Optoelektronik, LMU. The acceleration voltage is around 3 kV to get an optimal image contrast while avoid damaging the samples. A working distance of around 3.5 mm is used for all the measurements.

3.1.3 Atomic force microscopy (AFM)

A major limitation of SEM is that due to the poor electrical conductivity of polymeric materials and the electron beam irradiation damage of organometal halide perovskite materials, [93] it is hard to access local morphological information on the nanometer scale. Using atomic force microscopy (AFM), the surface topography, the phase information as well as surface roughness of thin films are measured. In this thesis, a 5500 Scanning Probe Microscope from Agilent Technologies is used.

Figure 3.1 shows a general AFM set-up. A very small tip with a radius of several nanometers is attached to the free end of a cantilever. The AFM data presented in this thesis are achieved with an aluminum backside coated pyramidal silicon tip from MikroMasch (US), having a radius of around 8 nm. When the tip approaches the sample surface, the cantilever is either repelled or attracted by various interactions. The sample-

tip potential can be described by a simple Lennard-Johns potential with a short-range repulsion and a long-range attractive part. Deflection of the cantilever is determined by means of a laser, which is directed on the rear top side of the cantilever and reflected onto a multiple segments photodiode. The deflected signals are recorded by the detector and are converted into an electrical signal. Therefore, the mechanical properties of sample surfaces are revealed.

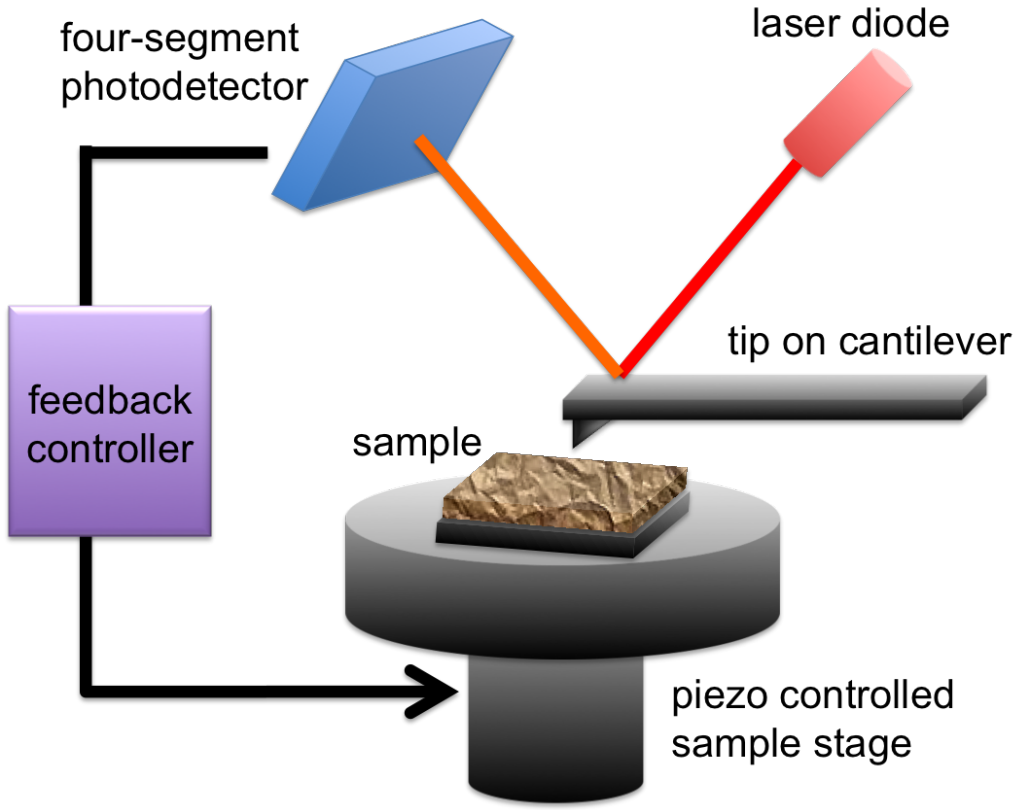

Figure 3.1: Schematic description of a standard AFM setup. The sample is placed on a piezo controlled sample stage. The cantilever with tip is positioned above the sample surface. Its displacement during line scanning is recorded on a four segment photodiode by means of the reflected laser beam. A feedback controller system is responsible for adjusting the sample-tip distance as well as data processing.

Depending on the sample-tip distance, three imaging modes are commonly used: the non-contact, tapping and contact mode. In this thesis, the tapping mode is selected to probe the samples in a safe condition with full preservation of the morphological information. Herein, the cantilever is excited by a piezoelectric drive force close to its resonance frequency ω and the sample is moved horizontally below the tip at a small sample-tip distance of less than 100 nm. In the tapping mode, the tip is still repeatedly touching the sample surface. During the measurement, the tip is tracing the scanning region of

the sample surface line by line, the changes in amplitude and frequency of the cantilever are detected and a electronic feedback control loop tunes the sample holder position to keep the sample-tip distance constant. By simultaneously recording these changes, the software calculates topography and phase images.

Images are taken with different scan sizes from 0.2×0.2 μm^2 up to 10×10 μm^2 for diblock copolymer based thin films. In the case of perovskite samples, the applied scan sizes are selected from 1×1 μm^2 up to 20×20 μm^2. In both cases, a scan speed of 1 ln/s is used. An excitation frequency $\sim$310 kHZ is selected within the resonance frequency for the tip (265-410 kHz). For good resolution, every image consists 512 lines and each line has 512 points. In oder to acquire the represntative information of every sample, several positions are measured. Using the software Gwyddion v2.47, the rms-roughness and power spectral density (PSD) of the measured data can be determined. For a quatitative understanding, the PSD of the 2D images were obtained by applying Fourier transformation following with radially averaged. The PSD yields lateral, characetristic surface structure information of the investigated sample, which can be compared with the inner film morphology obtained from scattering data. [94, 95]

3.1.4 X-ray reflectivity

X-ray reflectivity (XRR) measurements are performed to gain insight of the vertical film composition, the film thickness and roughness. The theoretical basics of reflectivity are discussed in Chapter 2.3.2.

The XRR experiments in this thesis are carried out at two different instruments, an Empyrean diffractometer (PANalytical) and a D8 reflectometer (Bruker). Figure 3.2 shows the principle setup for XRR measurements. Both instruments operate with a copper anode, that generates an X-ray beam with a wavelength of $\lambda = 0.154$ nm. Samples deposited either on silicon or on glass substrates are placed on the sample table, and a knife edge collimator is placed right above the sample surface to cut off the large footprint of X-ray at shallow incident angles. The generated X-ray beam is collimated through a slit system and impinges on the sample at a incident angle Θ. Whereas the reflected X-ray beam passed through a monochromator and is recorded on the detector in the specular reflection $\Theta/2\Theta$ mode.

At both instruments, the incident angle of Θ is varied from 0° to about 7° with a detection step of 0.005°. For measurements at the Empyrean diffractometer, a 1/32° divergence slit and a 1.4 mm anti-scatter slit are placed in the incident beam path to provide good resolution. Additionally, a 10 mm fixed mask defines the irradiated width on the samples. In the case of the D8 reflectometer, two slits with sizes of 0.2 mm and

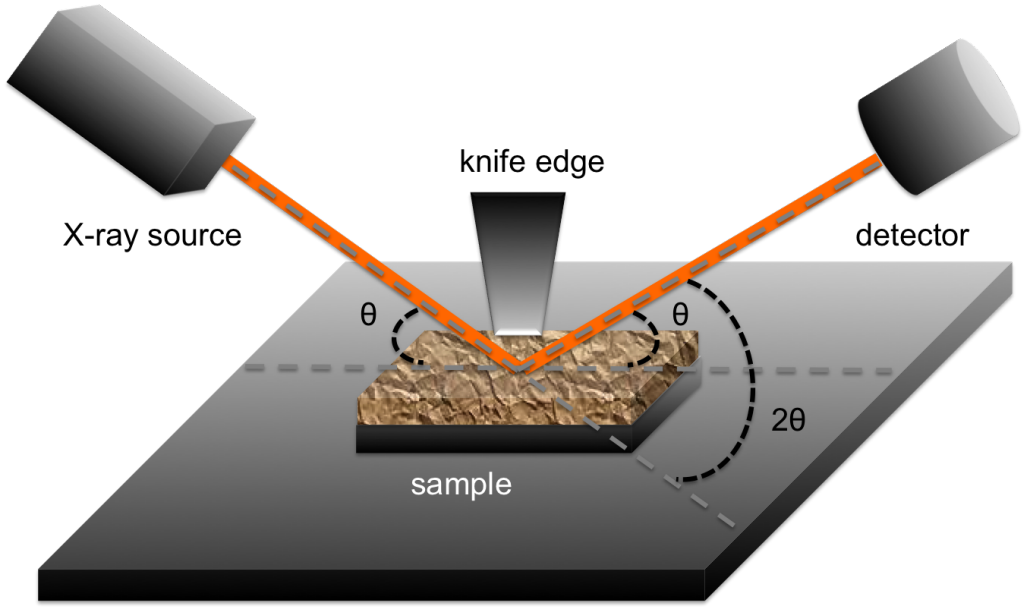

Figure 3.2: Schematic standard setup of XRR and XRD measurements. A knife edge is used in XRR measurements to cut off the large footprint of X-ray beam, aiming for a further collimation and reduction of the diffuse scattering. For XRD measurements, the knife edge is completely removed out of the beam.

0.1 mm are used to define the incident beam path, whereas a 0.05 mm slit is placed on the diffracted beam path.

Due to the difference in electron densities of different layers in the probed films, reflections occur at the surface and interfaces. The information of the layer composition, film thickness and roughness are directly related to the period at the interferece fringes, the intensity height and the curve slope. This allows to fit the recorded reflectivity with a muti-layers model. The software package Motofit [96] for IGOR Pro is used to simulate the reflectivity data, which accounting differences in thickness, scattering length density (SLD), interlayer roughness and refractive index. The obtained SLD vs. distance profile reveals the vertical film compositions.

3.1.5 X-ray diffraction

X-ray diffraction (XRD) is a widely used technique to identify the atomic structure and phase mixtures of crystalline materials. The theoretical background is introduced in Chapter 2.3.3.

A D8 reflectometer (Bruker) and an Empyrean diffractometer (PANalytical) are used for the XRD measurements. The working setup for XRD measurements follows a similar

principle as illustrated in the case of XRR measurements (Figure 3.2), but no knife-edge is applied. An X-ray beam with a wavelength of $\lambda = 0.154$ nm is generated from a copper anode and impinges on the sample under an angel Θ.

Two different experimental set-up are used for polymeric materials and for organometal halide perovskite materials. To enhance the signal intensity, a grazing incidence experimental geometry is used for diblock copolymer films. Better statistics are achieved under the grazing incidence geometry because of the beneficial effect of a larger probing footprint. The incident angle Θ is kept at a constant value of 0.2°, slightly above the critical angle of the investigated materials (0.17°). The diffraction intensities reflect the crystalline information of the probed samples along the surface normal direction. A typical 2Θ range from 2° to 30° is used with a step size of 0.01° for probing all samples. Each step takes 21 s. Even so, for the semicrystalline polymeric materials, each sample is measured for 17 hr to achieve sufficient statistics. For perovskite films, the conventional Bragg–Brentano setup is used, and the angle between the incoming X-ray beam and the point detector is always kept at 2θ. The measurements are typically performed for a 2θ range from 2° - 55° with a step size of 0.005°. Each step is counted 4 s. The obtained XRD peaks are fitted with Gaussian functions. Using Scherrer equation (Equation 2.55), the extracted full width at half maximum (FWHM) values as used to calculate crystal sizes. By combining the reflectivity data that is obtained from XRR measurements, information about 3D bulk perovskite crystals as well as low dimensional perovskite crystallites can be collected.

3.1.6 Grazing incidence scattering

Grazing incidence scattering (GIS) is used to obtain the buried structure of semiconductor thin films in terms of inner morphology and crystal orientation. Compared to real space microscopic characterization techniques (e.g. AFM), GIS can deliver morphological insight of the investigated thin films in a statistical view. The structural transformation can be monitored in real time under specific solvent or gas atmosphere. Thus, grazing incidence scattering has attracted tremendous attentions and popularity as an advanced technique for thin film characterization. In Figure 3.3, the principle setup of a grazing incidence scattering experiment is presented. Depending on the sample-detector distance (SDD), scattering angles and the resolvable length scales are defined. In the case of a short SDD (≈ 0.1 m), scattered signals can be recorded at the two-dimensional (2D) detector at large angles corresponding to small distances below 1 nm. Therefore, molecular information, i.e. the crystallinity, is obtained by grazing incidence wide angle scattering (GIWAS). For longer SDD (≈ 1 m), scattered signals at smaller angles of typically less

than 5° are detected by grazing incidence small angle scattering (GISAS), corresponding to distances ranging from approximately 1 nm up to 1 µm. Thus, by combining grazing incidence wide angle scattering and grazing incidence small angle scattering all relevant length scales in semiconductor thin films can be addressed. X-rays or neutrons can be used as scattering probes depending on the intrinsic contrast condition of the investigated systems. The theoretical background of GIS for X-rays and neutrons is introduced in Chapter 2.3.4.

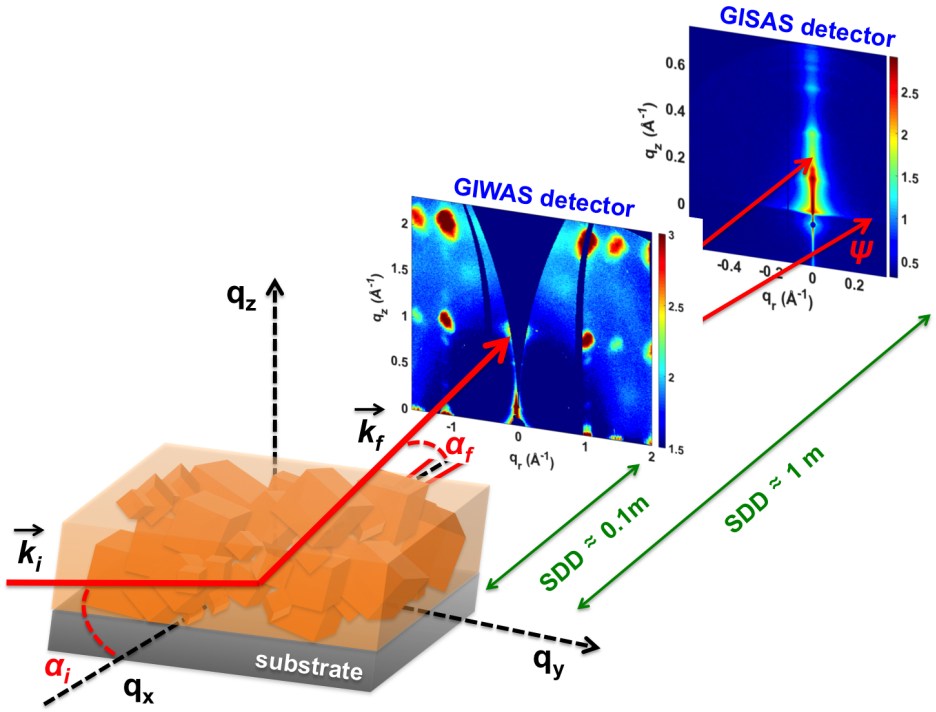

Figure 3.3: Schematic illustration of a standard GIS setup. The explanation of different labels is given in the text. The X-ray beam (red) impinges on a sample under a shallow angle α_i and is reflected with the angles of α_f and ψ. Depending on the SDD distance, the scattered signal is recorded on the 2D detector at different angles, corresponding to different length scales.

Grazing incidence wide angle X-ray scattering

In this thesis, grazing incidence wide angle X-ray scattering (GIWAXS) is employed to obtain the information about crystal orientation and crystal size in organometal halide perovskite thin films. GIWAXS experiments are carried out using an in-house Ganesha 300XL SAXS-WAXS diffractometer with a Cu-K_α X-ray source with an X-ray energy of 8 keV. The basic setup of GIWAXS measurement is illustrated in Figure 3.3. An X-ray beam with a wavelength of 0.154 nm impinges the sample under a shallow angle of 0.4° relative to the sample surface and the scattering signal is recorded on a 2D detector at a

SDD of about 106 mm. A Pilatus 300k detector is employed, which has 487 × 619 pixels with a pixel size of 172 × 172 µm^2. The analysis of the 2D GIWAXS data is performed with the GIXSGUI software. [91] All samples investigated with GIWAXS in this thesis are deposited on glass substrates and were measured for 6 hr to improve the statistics.

Unlike the data obtained from grazing incidence X-ray diffraction measurements, where typically only the signal along the specular reflected beam is measured (3.1.5), the GIWAXS data contains information corresponding to the sample surface. Quantitative information about the crystal orientation relative to the substrate surface can be revealed by selected radial integration of the 2D GIWAXS data as depicted in Figure 3.4, that results in a plot of the crystal orientation relative to the substrate with an angle of χ versus the scattering intensity. The peaks are fitted with Gaussian functions. The crystallite size for 3D perovskite crystal is calculated by the Scherrer equation (Equation 2.54).

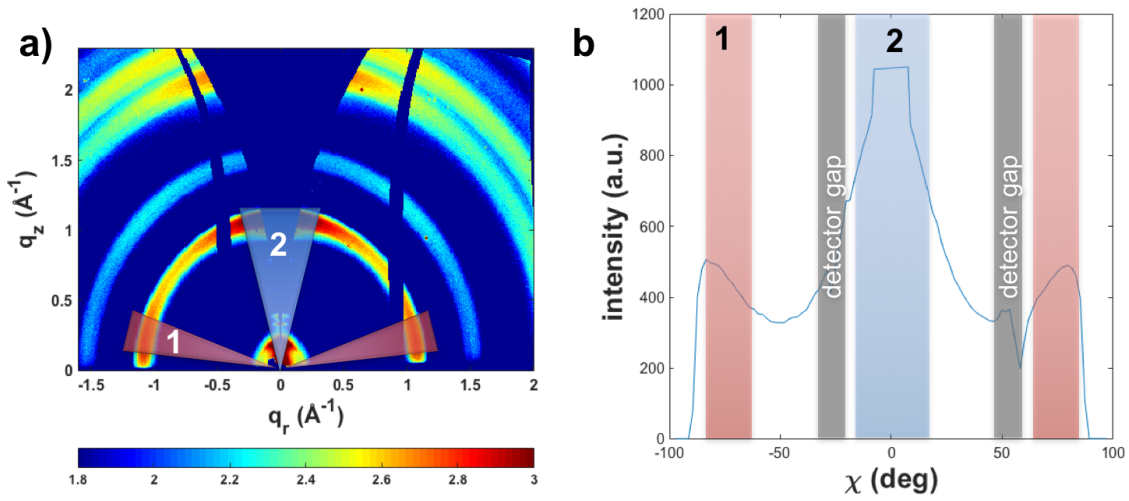

Figure 3.4: a) Standard 2D GIWAXS data. Two azimuthal segments are highlighted as red and blue boxes. b) Azimuthal intensity integration of the diffraction peak locates at 1.1 Å^{-1}. The extracted intensity distribution is plotted as a function of χ angle. The colored highlights are identical to those in panel a. The detector gaps are marked with grey boxes.

Grazing incidence small angle X-ray scattering

The setup for grazing incidence small angle scattering (GISAXS) is in principle the same as for GIWAXS measurements apart from the larger SDD to capture the scattering signals at smaller exit angles. In the present thesis, GISAXS is used to examine the perovskite domain information as well as two-dimensional (2D) perovskite crystallized structures.

GISAXS measurements are carried out using an in-house gallium anode low-angle X-ray instrument (GALAXI) equipped with a Dectris Pilatus 1M detector. [97] The X-ray beam is generated from a Bruker AXS metaljet X-ray source with a wavelength of 0.134 nm which irradiates the sample surface under an incident angle of 0.4°. A SDD of 829 mm is used during all measurements and combined with the grazing incidence geometry, a relatively large footprint of the X-ray beam in the millimeter range is generated. Each sample is measured for 6 hr for sufficient statistics. As a consequence, quantitative structural information with sizes between 3 nm and 100 nm is obtained from the relatively large volume fraction of the investigated samples, as introduced in Chapter 2.3.4.

The scattering data recorded in the vertical direction along the 2D detector reflects the information about the film composition perpendicular to the substrate surface, whereas the data along the horizontal direction contains information about the lateral mesoscale structures. In order to attract the morphological parameters, detailed analysis can be performed by making line integrals in horizontal and vertical direction. The cuts are either extracted by the software Fit2D or by the GIXGUI software. [91] From the horizontal line cuts, more accurate information about lateral structure distribution and spatial correlation can be revealed from the fit based on one-dimensional (1D) paracrystal model within the frame of distorted wave Born approximation (DWBA) as described in Chapter 2.3.4.

Grazing incidence small angle neutron scattering

Grazing incidence small angle scattering can also be performed by using neutrons as the type of probe. Grazing incidence small angle neutron scattering (GISANS) is used to investigate the structure information buried in the semiconductor thin films. In general, the basic setup of GISANS measurement is very similar to the setup for GISAXS measurements, with the main difference being that the transmitted signal is also resolvable in GISANS using silicon as substrate. GISANS is well suited to investigate the diblock copolymer:fullerene blend systems because the scattering contrast is enhanced by the mixed phase of PCBM and polymer. [98]

For the investigated polymer samples, GISANS experiments are carried out at the KWS-1 beamline at the Heinz Maier-Leibnitz Zentrum (MLZ), Garching. [99] A wavelength spread $\triangle\lambda/\lambda$ of 10 % is provided by a dornier velocity selector, and the scattered neutrons are recorded with a 2D angle-type 6Li-Scintillation detector. The detector contains 128 $\times$ 128 pixels with a pixel size of 5.3 $\times$ 5.3 mm^2. The incident beam shape is defined by two apertures with sizes of 10 $\times$ 30 mm^2 and 1 $\times$ 20 mm^2. The collimation length and the SDD are chosen to be 8 m and 7.7 m with a neutron wavelength of 0.7 nm to obtain a resolvable structure length scale between 10 nm and 200 nm. Each sample is measured 8 hr accounts for enough statistics.

For the perovskite samples, the scattering experiments are performed at the KWS-3 beamline at MLZ. [100] Incident neutrons are provided by a MgLi velocity selector with a wavelength spread $\triangle\lambda/\lambda$ of 20 %, whereas the scattered neutrons are detected by a 2D angle-type 6Li-Scintillation detector with a pixel size of 0.34×0.34 mm^2. A neutron wavelength of 1.28 nm is used for all measurements in order to secure high flux. The two entrance apertures are 2×2 mm^2 and 5×50 mm^2. By using a long collimation length of 10 m and a short SDD of 1.24 m, a larger structure length ranging from 50 nm to 400 nm is obtained. At KWS-1, the incident angle α_i is chosen to be 0.6° whereas at KWS-3, it is 0.56°.

The GISANS data are fitted using the fitting procedure of the GISAXS profiles to extract the morphological parameters in the probed samples. The scattering profiles are determined by the behavior of the power law scattering to elucidate additional structure information, such as film compactness and fractal morphology.

3.2 Spectroscopic characterization

Spectroscopic characterization methods like UV/Vis spectroscopy (Section 3.2.1) and photoluminescence (Section 3.2.2) are used to record the wavelength dependent absorption and fluorescence behavior of the investigated material systems. Also, information on charger carrier recombination, molecular ordering and quantum confinement phenomena within 2D layered perovskite structures can be revealed by analyzing the obtained spectra. Moreover, time correlated single photon counting (TCSPC) (Section 3.2.3) is used to determine the time-resolved kinetics of photoemission from the band-edge and the amplified spontaneous emission (ASE) (Section 3.2.4) is measured in air to draw a conclusion for the applicability of the investigated perovskite thin films as a gain medium.

3.2.1 UV/Vis spectroscopy

Absorption measurements are carried out with two different PerkinElmer UV/Vis spectrometers, the Lambda 35 and Lambda 650S. Both spectrometers are equipped with a halogen lamp and a deuterium lamp, covering a complementary light spectra from ultraviolet to visible wavelength region. In the case of the Lambda 35, the lamp is automatically switched at 326 nm, whereas the switch between the light sources in Lambda 650 S starts at 320 nm. Monochromatic light beams are provided by an optical grating and a slit system.

In the present thesis, all the investigated samples are deposited on acid-cleaned quartz glass. The software UV Winlab is used to control the spectrometer. Before every transmission measurement, an auto-zero measurement is performed on an acid cleaned bare glass substrate as a reference in order to obtain 100 % transmission. The transmitted signals going through the sample and through the reference are detected by photo diode. From this intensity ratio, the wavelength dependent absorbance $A(\lambda)$ is calculated using the Beer–Lambert's law.

$$A(\lambda) = -log_{10}\left(\frac{I_t(\lambda)}{I_0(\lambda)}\right) = \alpha(\lambda)\mathrm{d}log_{10}\mathrm{e} \tag{3.1}$$

with the initial and transmitted intensities $I_0(\lambda)$ and $I_t(\lambda)$, the material specific absorption coefficient $\alpha(\lambda)$ and the film thickness d. The linearity of the absorption coefficient can be used to determine the thickness of polymer films.

Furthermore, in the case of conjugated polymers, i.e. P3HT, the absorbance spectra can be further studied to extract structural information. The main absorption peak position of conjugated polymers is a measure for the inter- and intramolecular ordering. In addition, vibronic states arise as shoulders and peaks, conclusions about the degree of crytallinity and exciton band width can be revealed in the frame of the weakly coupled H-aggregate model (Chapter 2.1.6).

3.2.2 Photoluminescence spectroscopy

Photoluminescence spectroscopy (PL) is used to probe the radiative electron emissions across the band gap and from sub-bands to the top of the valence band. After photon absorption in semiconductor or semicrystalline polymer materials, photons are emitted at a higher wavelength. Two different fluorescence spectrometers both equipped with a Xenon discharge lamp acting as the light source are used in the present thesis.

For the investigation of the optically active polymer system, a fluorescence spectrometer LS55 (PerkinElmer) is employed. Samples are excited at a wavelength of 485 nm and a red-sensitive Hamamatsu R928 photomultiplier detects the PL signal. Due to the absence of a calibration standard, measurements are performed directly one after one in sequence to maintain comparability. In the conjugated:fullerene blend system, the PL intensity is a measure for the exciton dissociation. If the PL intensity of the polymer:fullerene blend sample quenches compared to that of the pure polymer sample, an indication for exciton dissociation can be addressed. In addition, the PL spectrum shape also reveals information on the molecular ordering of conjugated polymers. The crystalline portion of the conjugated polymer exhibits shoulder-like features in the florescence spectra.

In the case of organometal halide perovskite samples, experiments were performed at the chair of Prof. Jochen Feldmann, Lehrstuhl für Photonik und Optoelektronik, LMU. PL spectra are recorded with a Fluorolog-3 FL3-22 (Horiba Jobin Yvon GmbH) spectrometer equipped with a water-cooled R928 PMT photomultiplier tube mounted at a 90° angle. Samples are excited with monochromatic beam with a wavelength of 365 nm and information of the energy levels of a certain sample can be revealed by recording the emitted PL signal. An integrating sphere is applied in order to determine the absolute quantum yield values of the studied perovskite thin films. In addition, the photoluminescence excitation (PLE) measurements of perovskite samples were performed with the same instrument by detecting at 560 nm.

3.2.3 Time correlated single photon counting (TCSPC)

The exciton generated after photon absorption travels through the sample during its lifetime. This time-resolved kinetic of photoemission from the band edge is tightly correlated to the morphological quality of the investigated system. In the present thesis, the time resolved PL signals are measured by using a time-correlated single photon counting (TCSPC) system associated with a Pinceton monochromator. Measurements were carried out at the chair of Prof. Jochen Feldmann, Lehrstuhl für Photonik und Optoelektronik, LMU.

During measurement, the sample is excited by a 1.22 MHz pulsed laser with a wavelength of 365 nm at $\sim 30°$ with respect to the surface normal. Afterwards, the time between a laser pulse and the emission signal is recorded by a PicoQuant PicoHarp 300 detector. Restricted by the equipment set-up, the detector can only measure the time-resolved emission signals at a specific wavelength. Therefore, a static PL measurement should be performed first. The time-resolved PL kinetic is extracted in term of a decay plotted as count rates against time, rather than a constant value.

3.2.4 Amplified spontaneous emission

To examine the optical quality, amplified spontaneous emission (ASE) experiments are carried out to determine the dominant recombination channels in the multi-dimensional perovskite samples. Measurements were performed at the chair of Prof. Jochen Feldmann, Lehrstuhl für Photonik und Optoelektronik, LMU.

The fundamental laser beam from Coherent Inc. is doubled by an external beta barium borate (BBO) crystal to obtain the excitation laser pulses. Thereafter, the generated 400 nm femtosecond laser pulses are directed into the organometal halide perovskite films from

the film-substrate interface to excite the sample. The applied laser pulses have a defined pulse width of 100 fs and a repetition rate of 1 KHz. Increased excitation intensity is applied during measurements to surpass the threshold of the stimulated emission of the investigated samples, while the excited PL spectra are collected in the backward direction of the laser beam. The measured samples were deposited on the acid-cleaned glass substrates. Experiments are conducted at room temperature.

4 Sample preparation

In this chapter, basic materials and applied processing steps which are involved in preparing the investigated samples are described. In the first part, all the studied materials and the employed solvents are introduced (Section 4.1). Next, the substrate cleaning routine including different substrate types which are used in the thesis are presented (Section 4.2). Afterwards, the detailed fabrication procedure of different samples are illustrated (Section 4.3). The synthesis routine (Section 4.3.1) and thin film deposition method (Section 4.3.2) for the studied two different material systems are explained. Finally, most systems require annealing as a post production treatment step which are subsequently specified (Section 4.3.3).

4.1 Materials and solvents

Depending on the studied systems, the necessary materials for the presented investigation can be divided into three groups: polymer electron donor, electron acceptor and perovskite precursors. A polythiophene derived diblock copolymer poly(3-hexylthiophene-*block*-styerene) (P3HT-*b*-PS) was selected as the p-type hole conducting material. A fullerene derivative phyeny-C_{61}-butyric acid methyl ester was used as the n-type conducting electron in the diblock copolymer:fullerene blend. In the case of fabricating organometal halide peroskite thin films, inorganic $PbBr_2$ salt as well as two different organic compounds, methylammonium bromide and n-octylammonium bromide were applied. In this thesis, halogenated solvent 1,2-dichlorobenzene (DCB) was used to prepare the polymer solution whereas n,n-dimethylformamide (DMF) was used for the perovskite precursors dissolution.

Electron donors

Poly(3-hexylthiophene-2,5-diyl) (P3HT) is typically used as the electron donor material in organic solar cells. However, in order to control the photoactive polymer morphology at a length scale of ten nanometer, a diblock copolymer which contains the same photophysical nature of the donar semiconducting polymer, such as P3HT, can be used as an alternative

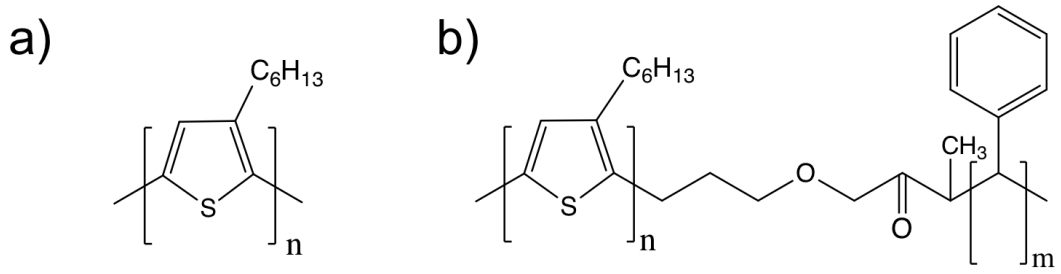

Figure 4.1: The chemical structures of the investigated conducting polymers a) P3HT, b) P3HT-*b*-PS.

approach. Additional desirable functionality can be brought in with the other block, like improved polymer crystallization and tailoring the interface between the electron donor and acceptor. [101,102] Following this idea, the diblock copolymer poly(3-hexylthiophene-*block*-styerene) (P3HT-*b*-PS) was selected as a model system. The chemical structures of both, P3HT and P3HT-*b*-PS are depicted in Figure 4.1. More details about the diblock copolymer, like molecular weight, polydispersity index (PDI), and the vendors sources are summarized in table 4.1.

Material	M_n (kg/mol)	PDI	Source
P3HT-*b*-PS	12.5-*b*-11.6	1.4	Polymer Source, Inc.

Table 4.1: Information of the used electron donor polymer: number average molecular mass M_n, polydispersity index (PDI) and the providing source.

Electron acceptor

A derivative of the buckminster fullerene, phyeny-C_{61}-butyric acid methyl ester (PCBM) was used as the electron conducting component. Figure 4.2 depicts the chemical structure of PCBM. Good solubility for PCBM is generated by the attached side chain. P3HT:PCBM is the most widely investigated material system for organic photovoltaic application. [103–105] In this thesis, an alternative approach by using PCBM as the n-type semiconductor, blended with P3HT-*b*-PS as the p-type semiconductor is studied.

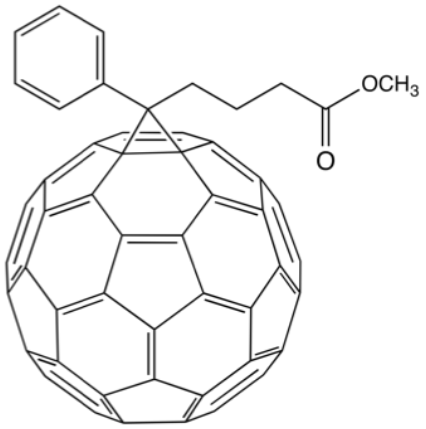

Figure 4.2: The chemical structure of PCBM.

Organometal halide perovskite precursors

Three chemicals were used in the solution processed perovskite synthesis. Two different lengths of the organic salts methylammonium bromide (MABr) and n-octylammonium bromide (OABr) were used as the cation precursors while lead bromide ($PbBr_2$) were served as the anion part. MABr and $PbBr_2$ were used as obtained from Dyesol and Sigma Aldrich, respectively. OABr was synthesized by following the route described in reference. [15] These precursors are well soluble in anhydrous dimethylformamide (DMF) solvent. The chemical structure of the organic precursors are described in Figure 4.3. Restricted by the intrinsic large size of OABr, it cannot diffuse into the lead lattice of $PbBr_2$ but dangle outward. Therefore, the $MAPbBr_3$ crystal growth can be consequently altered by differing the OABr content. For the organometal halide perovskite, the resulting crystal structure can be three-dimensional (3D), two-dimensional (2D), or even down to zero-dimensional (0D).

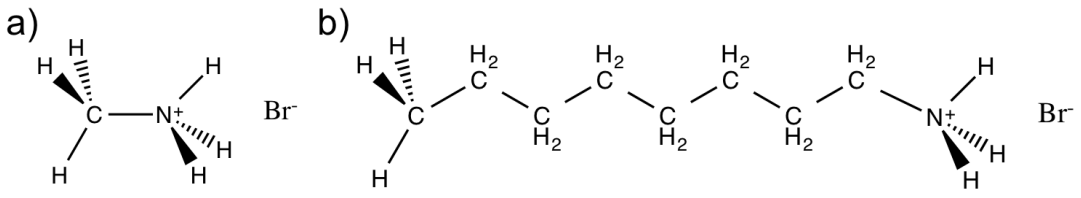

Figure 4.3: The chemical structures of the employed organic cation in the perovskite synthesis a) MABr, b) OABr.

Solvents

1,2-dichlorobenzene (DCB) is an aromatic compound with the molecular formula $C_6H_4Cl_2$, in which chloride substituents are adjacently located (Figure 4.4a). As a derivative of benzene, the colorless, flammable liquid has a boiling point of 180 °C with a density of 1.31 g/cm^3 at 25 °C.

Dimethylormamide (DMF), is an colorless organic liquid compound with the molecular formula $(CH_3)_2NCH$ (Figure 4.4b). It is miscible with water as well as the majority of organic liquid compounds. Its boiling point is 153 °C and the density is 0.944 g/cm^3 at 25 °C.

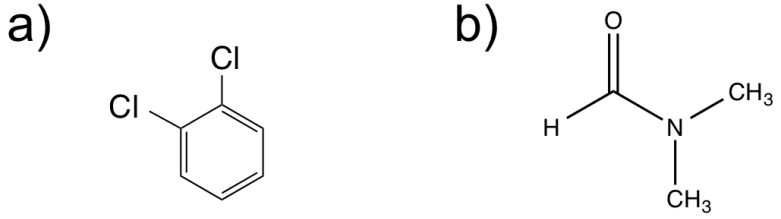

Figure 4.4: The chemical structures of the applied solvents a) DCB, b) DMF.

4.2 Substrates

In the present thesis, glass and silicon substrates were used depending on the investigated systems and the applied characterization techniques. The glass substrates were bought from Carl Roth GmbH with a size of 3.6 × 7.6 × 1 mm^3. The silicon substrate was purcahsed from Si-Mat as a p-doped wafer with a diameter of 100 mm and a thickness of (525 ± 25) µm. Depending on the specific investigation technique, the substrates are cut into the required dimensions. In the case of optical spectra characterization, glass substrates were cut to a size of 22 × 22 μm^2. This size was used to study surface morphology as well as x-ray scattering. Due to the relatively low neutron flux, a full piece of silicon wafer was used during neutron scattering experiments in order to achieve a better statistic.

4.2.1 Acid cleaning

In order to obtain a controllable surface property of the substrates, acid-cleaning was used as a pre-cleaning step before the film casting. [106] The cut substrates were placed in a teflon sample holder which was subsequently immersed in a acid bath for 15 mins at 80 $°C$. The compositions of the acid bath is listed in table 4.2. Afterwards, the sample holder was put into de-ionized (DI) H_2O for 10 mins at room temperature and each substrate was rinsed with DI H_2O. Dry oil-free nitrogen was used to blown dry the substrate surface. The substrates were used on the same day. [106]

chemical	amount (ml)
DI H_2O	22.5
H_2O_2 (30%)	35
H_2SO_4 (96%)	35

Table 4.2: The composition used in the acid bath for substrate cleaning.

4.3 Processing

Solution processed semiconductor thin films are advantageous for cheap large scale production, e.g. roll-to-roll printing. In the present thesis, spin-coating techniques was selected as a first step to start the investigation.

4.3.1 Solution preparation

P3HT-*b*-PS:PCBM BHJ thin films

As a first step, P3HT-*b*-PS and PCBM were weighed in cleaned vials in according to the designed blend ratios. In order to eliminate the potential pollution from the glass vials, a pre-washing step of the glass vials is necessary when DCB. Secondly, PCBM was dissolved in DCB at 60 °C for $\sim$ 2 hr until no solid residue is visible. Afterwards, the PCBM solution is used to dissolve P3HT-*b*-PS. In order to avoid big deviation in film thickness, the prepared solution concentration in terms of P3HT-*b*-PS concentration is 20 mg/ml for samples with a PCBM weight fraction smaller than 50%, 16 mg/ml for sample 58% , and 12 mg/ml for sample 67%. Because of the pour solubility of the polymer materials, the solution temperature was kept at 60 °C on a shaker overnight.

Mixed dimensional lead bromide perovskite thin films

For synthesizing the perovskite thin films, the precursors were dissolved separately in glass vials with anhydrous DMF as solvent. All glass vials were pre-cleaned before solution preparation and dried in a furnace at 100 °C to remove the liquid residue. The total mole concentrations for MABr, OABr and $PbBr_2$ are 1.67 M, 1.67 M and 1 M, respectively. All solutions are kept at 80 °C and stirred with magnetic stirrers to achieve a better dissolving. $PbBr_2$ was dissolved for 30 mins while MABr and OABr were dissolved for 15 mins. The mole ratio between MABr and OABr were tuned to achieve different morphology whereas organic and inorganic reagents were kept at 1:1. To synthesize the mixed dimensional perovskite materials, the mixed solution were kept at 80 °C with magnetic stirrers for 15 mins.

4.3.2 Spin coating

All samples investigated in this thesis were prepared by spin-coating method. Solutions with a defined concentration c_0 were applied to cleaned substrates achieving surface coverage. Afterwards, the substrate was rotated to reach a selected rotational speed w. After a certain rotation time, a thin layer is formed. In addition, a hot-casting spin coating process was used to have a good spread of the solution over the surface, in which all substrates were pre-heated at a temperature used in the post thermal annealing process. The correlation between the applied parameters and the resulting film thickness (d) can be described by [107]:

$$d = A \left(\frac{1950rpm}{w}\right)^{1/2} \left(\frac{c_0}{20gL^{-1}}\right) \left(\frac{M_w}{100kgmol^{-1}}\right) \tag{4.1}$$

where A is an experimental parameter depending on the used spin coater and the environmental conditions, M_w is the molecular weight of the used material. All the applied spin coating parameters are listed in table 4.3

material	rotation speed w (rpm)	acceleration level	time (s)
P3HT-*b*-PS:PCBM	1500	9	40
lead bromide perovskite	3000	9	200

Table 4.3: Summary of applied spin coating parameters for preparation of thin films.

4.3.3 Thermal annealing

In general, the fast solvent evaporation during the spin coating process will result in a non-equilibrium morphology and less developed crystallization. Therefore, a thermal annealing process was performed after the preparation of both P3HT-*b*-PS:PCBM BHJ films and mixed dimensional lead bromide perovskite films. For polymeric thin films, the thermal annealing increases mobility of the the polymer chains and the fullerene molecules, resulting in a rearrangement of morphology on different length scales. In the case of perovskite films, the residue solvent buried in the fresh spin coated films is removed, which improves the perovskite crystallization. [108, 109] Table 4.4 summarizes the parameters used for thermal annealing:

material	temperature ($^{\circ}C$)	time (min)
P3HT-*b*-PS:PCBM	140	20
lead bromide perovskite	100	2

Table 4.4: Summary of the applied thermal annealing parameters for the preparation of thin films.

5 Nanostructuring of diblock copolymer-fullerene thin films

Parts of this chapter have been published in the article: Effect of PCBM additive on morphology and optoelectronic properties of P3HT-*b*-PS films [110] (R. Wang et al., Polymer, 121, 173-182, 2017.)

Block copolymers are a promising material for optoelectronics devices due to their intrinsic ability to microphase separate into a large variety of well-ordered nanoscale structures with tailored physical propeties. [9, 10, 111, 112] In contrast to a blend of two immiscible components, the two polymeric segments are covalently bound in diblock copolymer. Therefore, an array of highly ordered nanostructures is formed *via* diblock copolymer self assembly rather than the unfavorable macrophase separation. [113] As a consequence, the ability to form nanoscale fine structural patterns from such diblock copolymers is very promising for application in functional nanotechnology, such as solar cells, lithium-ion batteries and drug deliveries. [25, 114–116]

For the well-investigated coil-coil block copolymers, the generated nanostructures are determined by the total degree of polymerization N, the Flory-Huggins interaction parameter χ and the volume fraction parameter f of the blocks. [117, 118] However, another block copolymer model system, the rod-coil block copolymers have gathered increased attention due to the functionality possibilities that can be add-in via the rod-block. In rod-coil block copolymers, unique optoelectronic properties can be offered by the conjugated polymer backbone, in addition to the ability to engineer the morphology on the nanoscale. Another three important parameters should be included to determine the self-assembly behavior for rod-coil block copolymers: the Maier-Saupe (π-π) interaction parameter μ, the competition between μ and χ, and the stiffness asymmetry parameter that resulted from the rod to coil length ratio ν. [119–121] Among the various types of rod-coil block copolymers system, poly(3-hexylthiophene) (P3HT) based rod-coil diblock copolymers have gathered a lot of attention. The P3HT block exhibits intriguing optical and electronic properties and is well applied in organic photovoltaic (OPV) studies as a p-type semiconductor in P3HT:PCBM blends. [105, 122, 123] In addition, the typical

exciton diffusion lengths in P3HT are around 10 nm, which can be well addressed by tailoring the nanoscale morphology of block copolymers. [7, 8, 124]

In this chapter, the morphology formation and the resulting optoelectronic properties of P3HT-*b*-PS:PCBM are characterized. Different blend ratios as a function of PCBM weight fraction are selected. Focus is put on resolving the influence of PCBM additive on the photophysical properties and nanoscale morphology of the P3HT-*b*-PS films. The first section illustrates the co-alternating of P3HT chain orientation alongside the variation of PCBM content (Section 5.1). The optoelectronic behavior of the P3HT-*b*-PS:PCBM blend films are examined by UV-Vis spectroscopy and photoluminescence spectroscopy (Section 5.2). The full morphology picture is revealed by various characterization techniques including both surface topography images and advance scattering techniques (Section 5.3). The extracted results exhibit good consistency with respect to the optoelectronic properties of the blend films.

5.1 Crystalline structure

The self-assembly behavior of rod-coil block copolymers is influenced by both microphase separation and the crystallization of the rod block. [125, 126] In order to reveal the crystallisation behavior within the P3HT-*b*-PS:PCBM blend films containing six different weight fractions of PCBM, grazing incidence X-ray diffraction (GI-XRD) measurements were conducted. Compared to the two dimensional (2D) grazing incidence wide angle X-ray scattering (GIWAXS) measurement, the extracted parameters from the applied one dimensional (1D) GI-XRD technique refer to the crystallites distributing along the substrate surface normal, i.e. the out-of-plane direction (q_z). In Figure 5.1a, a distinct reflection peak at $q_z \approx 3.8$ nm^{-1} is visible in sample containing the lowest PCBM weight fraction (9%) (purplish red curve), being indicative for the (100) reflection of the P3HT lamellar stacked backbone. More specificially, another two higher reflection orders, namely the (200) and (300) reflections are also apparent at $q_z > 6$ nm^{-1}, which suggests that the P3HT crystallites adopt a well-ordered edge-on orientation (as depicted in Figure 5.1b). [127, 128] However, no PCBM crystals are identifiable at this composite. It is reported that the interaction energy between PCBM with PS is larger with respect to that of PCBM with P3HT. [129] Herein, we hypothesize that the crystallization of P3HT block is not suppressed by a small PCBM weight fraction of 9% and the amorphous PCBM molecules are preferentially interact with the PS segment.

Upon increasing the PCBM content till 33%, the intensity of the (h00) reflection family diminishes due to a loss in P3HT crystalline order whereas another two interesting features arise at $q_z > 12$ nm^{-1}. Firstly, a broad peak locates at $q_z \approx 13.8$ nm^{-1} grows in

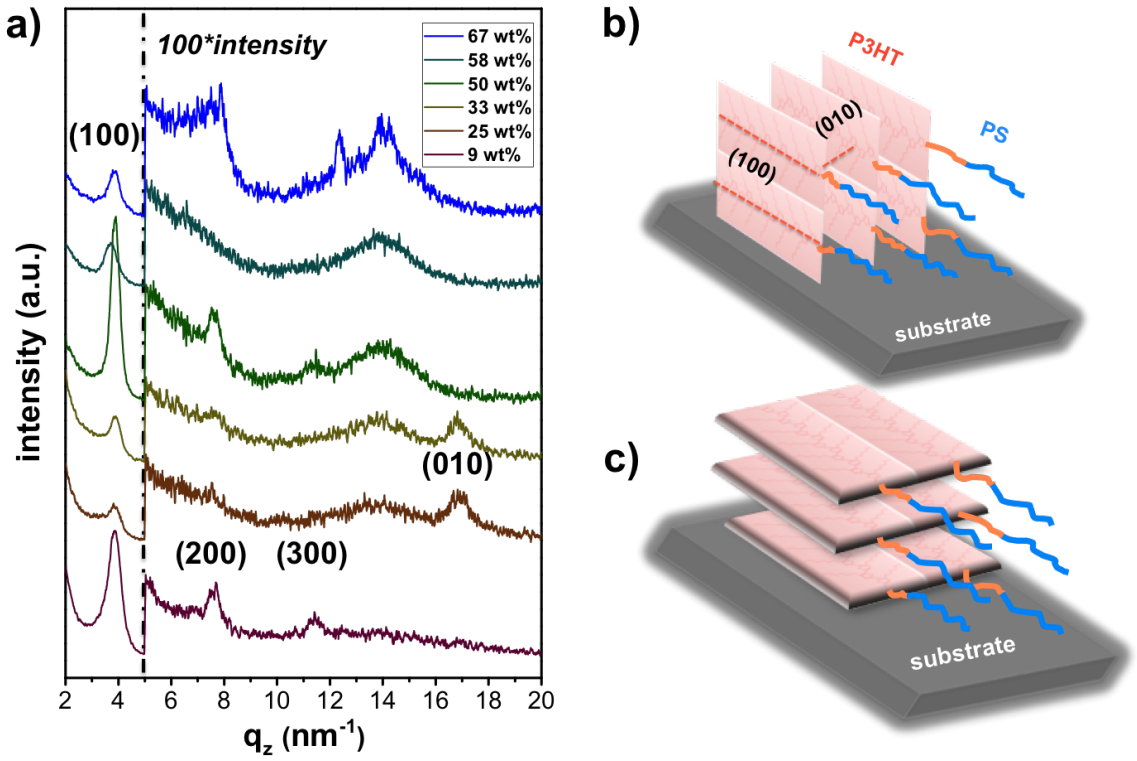

Figure 5.1: a) GI-XRD data of P3HT-*b*-PS:PCBM BHJ films with different blend ratios as indicated. The intensities at $q_z > 5$ nm^{-1} are multiplied by a factor of 100 to make the weak peaks visible. The obtained curves are shifted along the y-axis for clarity. Illustrations of P3HT crystallites with b) edge-on orientation and c) face-on orientation are depicted. Reproduced from Ref. [110] with permission from the Elsevier B.V.

intensity which can be ascribed to the PCBM crystallization. Secondly, a well define reflection peak appear at $q_z \approx 16.8$ nm^{-1}, being indicative for the kinetically favorable (010) reflection of the P3HT aromatic π-π stacking. [127] This feature suggests an additional face-on orientation emerge in samples contain PCBM weight fraction of 25% and 33%. The addition of fullerene molecule or nanoparticle into well developed diblock copolymer can lead entropic penalty as well as chain stretching to accommodate the additive, which generate disorder or macrophase separation. [130, 131] Therefore, a kinetic rather than thermodynamic mechanism is more likely dominated in samples with PCBM weight fraction of 25% and 33%.

The (010) reflection peak vanishes with further increasing the PCBM weight fraction above 50% whereas the higher orders of (h00) reflection are recovered, which is indicative

to an increased population of thermodynamically stable edge-on crystals are developed. Hereby, we can conclude that the P3HT crystallites adopt different molecular orientations with respect to the substrate at different blend ratios and PCBM molecules are better crystallized in sample containing a higher PCBM content. For a further analysis, two Gaussian-shaped peaks are used to represent the P3HT (100) reflection peak and the PCBM reflection peak. Detailed peak positions are extracted, which allows drawing conclusions on intermolecular distances (lattice constant) and crystal sizes of both P3HT and PCBM crystallites.

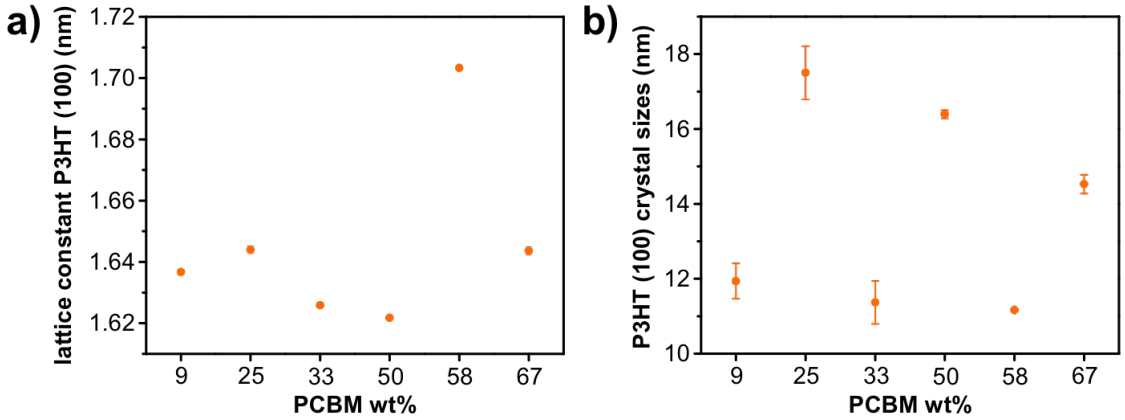

Figure 5.2: a) Intermolecular lattice constant and b) crystal sizes of P3HT (100) lamellar stacking in P3HT-*b*-PS:PCBM blend films with six different PCBM weight fractions.

The lattice constants of P3HT and PCBM are calculated from the peak center positions (q_{zc}) using equation $d = 2\pi/q_{zc}$. As shown in Figure 5.2, despite the sample with a PCBM weight fraction of 58%, similar lattice constant around 1.63 nm in (100) lamellar stacking are revealed, which is consistent with P3HT lattice constant reported in other studies. [132, 133] A larger P3HT lattice constant refers to a less developed long range ordering of polymer chains, which could have resulted from either diblock copolymer microphase separation or P3HT block crystallization. On the basis of the following grazing incidence small angle neutron scattering (GISANS) result (Section 5.3.3), the distinct large lattice constant at 58% can be attributed to the morphology transformation, in which higher ordering of the polymer chains are diminished. In Figure 5.2, the P3HT crystal size is found to be independent of the PCBM content. This scenario can be deduced by the interference with strong scattering signals of PCBM crystals and a comparable length scale of diblock copolymer domain structures that spans the similar q ranges.

In Figure 5.3a, a lattice constant around 0.47 nm for PCBM crystallites is found at all blend ratios. This value is smaller than the double fullerene radius (2×0.4 nm) and can be ascribed to the distance of two opposite faces of neighboring fullerene molecules. [134]

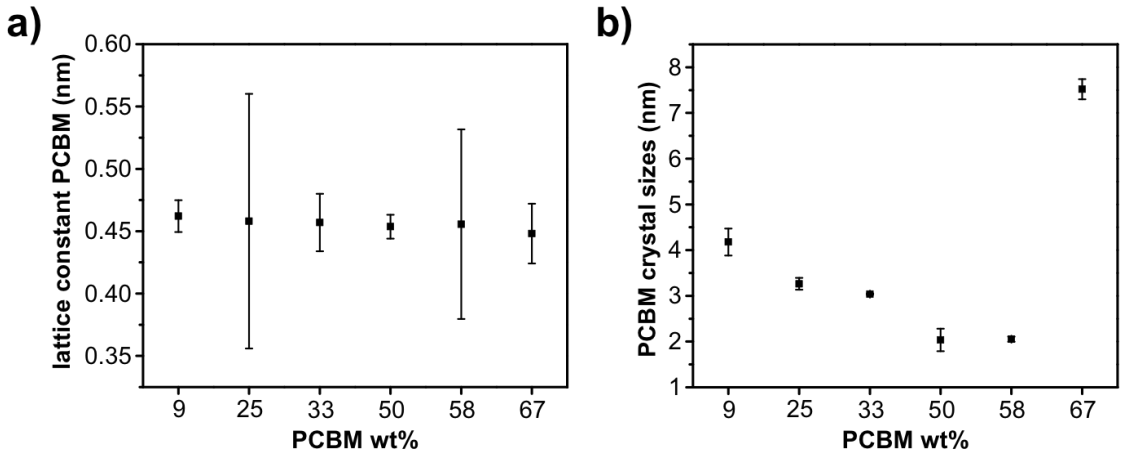

Figure 5.3: a) Intermolecular lattice constant and b) crystal sizes of PCBM crystallites in P3HT-*b*-PS:PCBM blend films with six different PCBM weight fractions.

In addition, the PCBM crystallite size grows from 2.1 nm to 7.5 nm while increasing the PCBM weight fraction from 58% to 67% (Figure 5.3b). This observed result indicates segregated PCBM domains can generate in sample containing a PCBM weight fraction of 67%.

5.2 Optical electronic properties

The understanding of the molecular order of polymer crystallite will have a close relationship with the charge carrier transportation, this will be important for future optoelectronic device fabrication. With this mind, the crystallite quality is investigated by means of optical spectroscopic techniques.

Figure 5.4a displays the absorbance data of all six blend films. The feature located at around 335 nm originates from PCBM and it increases in intensity upon loading a higher weight fraction of PCBM. The absorbance spectra at larger wavelength (> 400 nm) are dominated by three distinct features: the main absorbance peak of P3HT at around 500 nm; the vibronic 0-1 transition peak of P3HT at around 550 nm; and the vibronic 0-0 transition peak of P3HT at around 605 nm. [98, 135] Upon increasing the PCBM weight fraction, the position of the P3HT main absorbance peak blue shifts towards smaller wavelength, indicating an increase in the energy band gap. This result reflects that the crystallinity of P3HT block is disrupted by PCBM addition, which is in good agreement with the GI-XRD observations (Figure 5.1). A reasonable consideration is that the crystallization of PCBM molecules are rapidly developing upon thermal annealing, which competes the crystallization of the P3HT block. [11] In addition, it was also reported

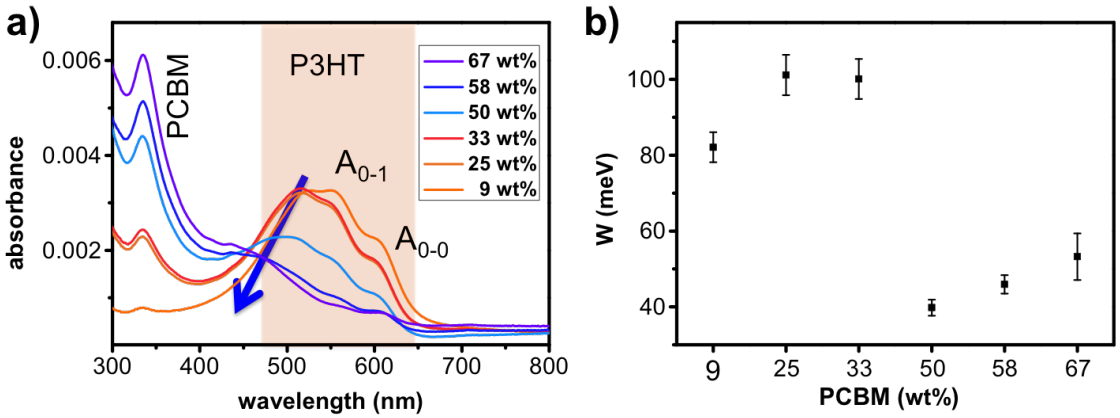

Figure 5.4: a) UV-Vis spectra of P3HT-*b*-PS:PCBM blend films with blend ratios as indicated. A blue shift of the P3HT main absorption peak is highlighted. b) Free exciton bandwidths W extracted from P3HT vibronic absorption features are plotted as a function of PCBM weight fraction. Images adapted from Ref. [110].

that the PCBM molecules not only purturb the P3HT interchain π-π stacking, but also contribute effect on the P3HT intrachian conjugation length. [136] In order to have a detailed understanding about the correlation between the different blend ratios and the resulted interchain coupling, further analysis is carried out to determine the free exciton bandwidth (W) using Equation 5.1 within the H aggregate model [45, 137]

$$\frac{A_{0-0}}{A_{0-1}} = \frac{n_{0-0}}{n_{0-1}} \left(\frac{1 - \frac{0.24W}{E_p}}{1 + \frac{0.073W}{E_p}} \right)^2 \tag{5.1}$$

where n_{0-i} denote the real part of the refractive index at the corresponding absorption bands and E_p is a constant value referring to the phonon energy of the electronically excited state. By assuming a refractive index ratio of ~1, Equation 5.1 can be rewritten to

$$W = \frac{E_p \left(1 - \sqrt{\frac{A_{0-0}}{A_{0-1}}} \right)}{0.073 \sqrt{\frac{A_{0-0}}{A_{0-1}}} + 0.24} \tag{5.2}$$

Equation 5.2 reflects that the free exciton bandwidth (W) is inversely proportional to the ratio of the 0-0 and 0-1 absorbance. Assuming the phonon energy E_p is equal to 0.18 eV, [45], the obtained exciton bandwidths in different blend ratios are plotted in Figure 5.4b. A small W value represents a large conjugation length with better P3HT crystallinity. The conjugation length of the P3HT block in the studied P3HT-*b*-PS:PCBM

blend films decreases with increasing the PCBM weight fraction from 9% to 33%, but this, notablly reverses with further adding PCBM content up to 67%. This result exhibits same trend as shown in Figure 5.2a, which gives indication that different mechanisms might dominate at different blend ratios. In addition, the obtained free exciton bandwidths in samples with a PCBM weight fraction above 50% are around 50 meV, which suggesting that the P3HT crystalline order fulfills the requirement for an efficient solar cell device. [132]

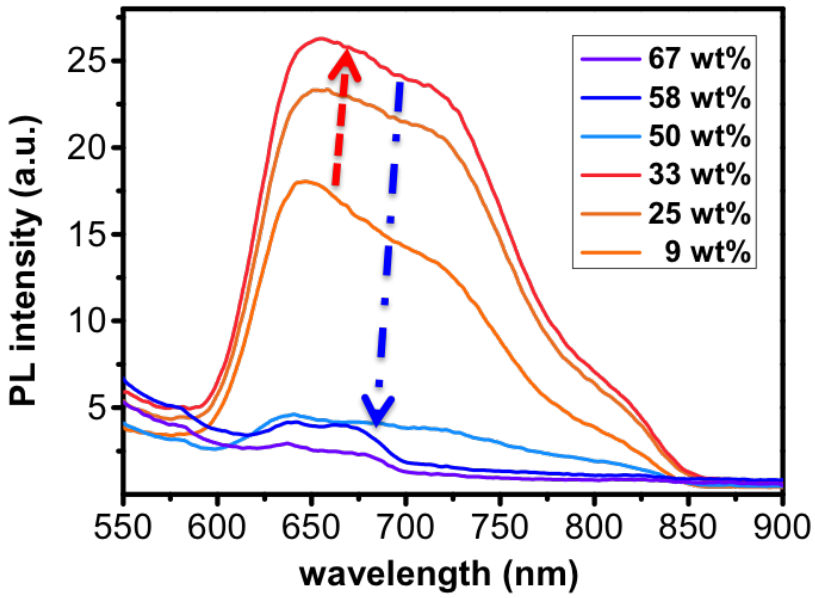

Figure 5.5: Photoluminescence (PL) spectra of P3HT-*b*-PS:PCBM blend films with six different blend ratios as indicated. Image adapted from Ref. [110].

Photoluminesence (PL) measurements are used to quantify the exciton dissociation quality in the P3HT-*b*-PS:PCBM blend films. The recorded PL intensity of the exciton radiative decay within the P3HT block in samples with different PCBM weight fractions are plotted in Figure 5.5. The PL intensity is found to first increase upon increasing the PCBM weight fraction from 9% to 33%, indicating well phase separated P3HT and PCBM domains. From literature, it was also reported that the PL intensity is sensitive to the P3HT chain order. [138] On the basis of the GI-XRD results (Figure 5.1a), the large disorder of the P3HT chains at 25% and 33% can also contribute effect on the increasing of the PL intensity. With further increasing the PCBM content, the PL intensity quenches three times from sample 33% to sample 67%. Considering the weight fraction of the P3HT block increases only by a value of 9%, the observed result can be ascribed as a fast photoinduced charge transfer between the P3HT electron donor and the PCBM electron

acceptor. [138] A quenched PL intensity indicates a successful exciton splitting at the interface between P3HT and PCBM, which is promising for real photovoltaic device. To deepen these findings, it is necessary to determine the morphology of the blend films.

5.3 Mesoscopic structure

In order to fully understanding the morphology in the P3HT-*b*-PS:PCBM blend films, different characterization methods are employed. X-ray reflectivity (XRR) measurements are carried out to reveal the vertical compositions of the resulting blend samples (Section 5.3.1) whereas the surface morphologies are studied with optical microscopy (OM) and with atomic force microscopy (AFM) (Section 5.3.2). To have a quantitative investigation of the domain structures as well as the self-assembly behavior of diblock copolymer inside the blends, grazing incidence small angle neutron scattering (GISANS) is applied (Section 5.3.3).

5.3.1 Vertical compositions

The phase separation of P3HT and PCBM in the film will generate morphological fine structures in both lateral and vertical directions. [133, 139, 140] In addition, the understanding of composition variation along the vertical direction in P3HT:PCBM blend is also important to guarantee a successful charge carriers extraction in standard optoelectronic devices, e.g. solar cells. [134, 141] In the present study, the vertical composition profiles in P3HT-*b*-PS:PCBM blend films are quantitatively resolved using XRR measurements. Figure 5.6 display the recorded XRR data of blend samples as a function of different PCBM weight fractions. Distinct fine Kiessig fringes are seen at all blend rations up to high q_z values (> 0.2 Å^{-1}). The film thicknesses are revealed to be 120 ± 20 nm from the frequency of the fringes. A composition dependent shoulder like intensity contribution can be seen at $q_z \approx 3.8$ nm^{-1}, which reflects the crystallization degree of the P3HT block at different blend ratios. This observation is in accordance to GI-XRD data.(Figure 5.1a)

To investigate the vertical composition profiles, the XRR data of the blend films are evaluated using the Motofit package by A. Nelson. [96] A best fit to the XRR data is obtained by modeling the reflectivity curves as a stack of three sub-layers with distinct X-ray scattering length density (SLD_{xr}).The three-layer model consists a surface enrichment layer, a uniform compact layer and an interface enrichment layer on top of the oxide-topped silicon substrate. A summary of the theoretical SLD_{xr} values are listed in table 5.1 Considering that PCBM exhibits a larger SLD_{xr} with respect to that of P3HT-*b*-PS, the revealed SLD_{xr} profiles essentially reflect the vertical distribution of PCBM across the

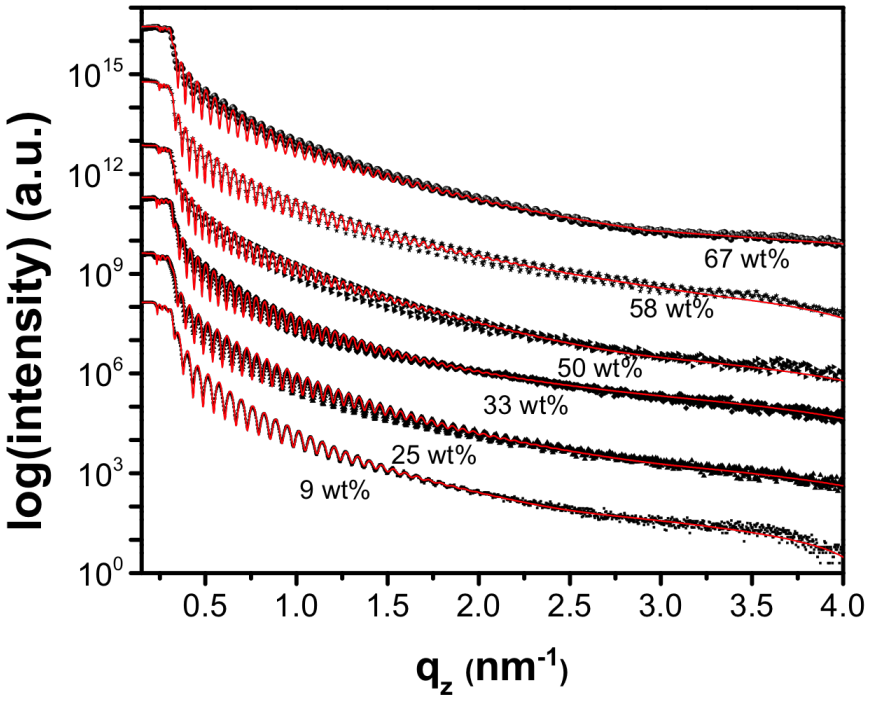

Figure 5.6: X-ray reflectivity (XRR) data (dots) with fits (red lines) of P3HT-*b*-PS:PCBM blend films with six different PCBM weight fractions as indicated in the image. The curves are shifted along the y-axis for clarity.

film. As shown in Figure 5.7, a bottom PCBM-enriched layer and a surface PCBM-depleted layer are observed at all blend ratios. This observation is in good agreement with the previous report in P3HT:PCBM blend films, in which it was speculated that these PCBM stratification layers at the film-substrate interface are formed by the PCBM molecules trapped in the residue solvent near the solid substrate. [140,142] Upon increasing the PCBM weight fraction, the PCBM molecules are slightly moving into the compact layer as indicated by the increasing in the SLD_{xr}. For the sample which contains the highest PCBM weight fraction (67%), the top surface PCBM-depleted layer is replaced by a layer having the PCBM concentration close to a level found in the bulk of the film (purple curve in Figure 5.7). This trend is consistent with photoluminescence results in Figure 5.5. The vertical phase separated polymer and PCBM weaken the quenching of fluorescence signal at lower PCBM content whereas successful exciton dissociation appears above a PCBM weight fraction value of 50%.

	SLD_{xr} (10^{-6} Å^{-2})
P3HT-*b*-PS	10.3
PCBM	12.9 [143]
SiO_2	22.7

Table 5.1: Summary of the X-ray scattering length density (SLD_{xr}) of P3HT-*b*-PS, PCBM and SiO_2.

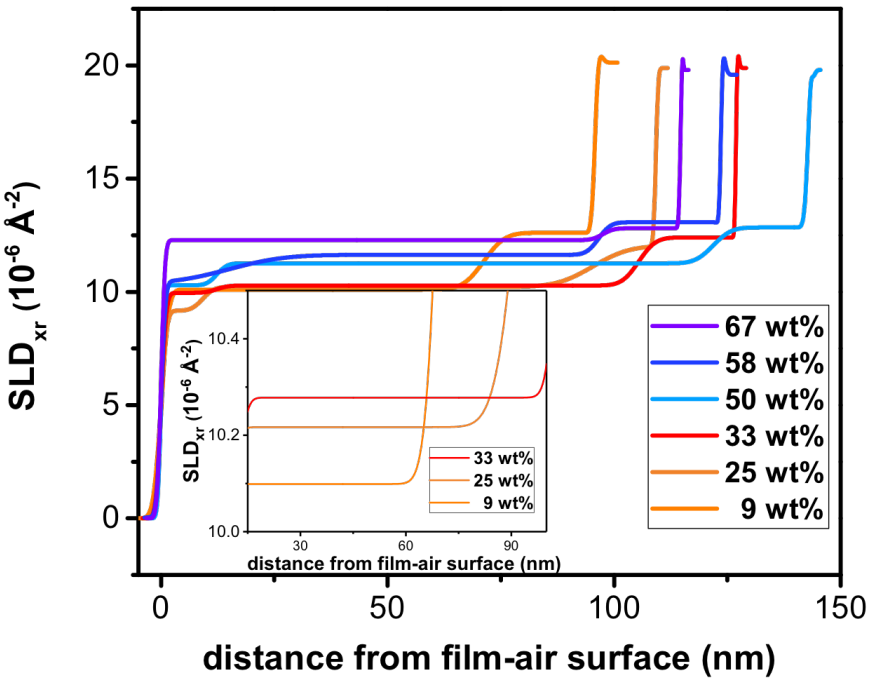

Figure 5.7: SLD profiles revealed by using the three sub-layers model as described in text. The inset displays a zoom-in view of the compact layers in sample contains PCBM weight fraction of 9%, 25% and 33% for better legibility.

5.3.2 Surface structure

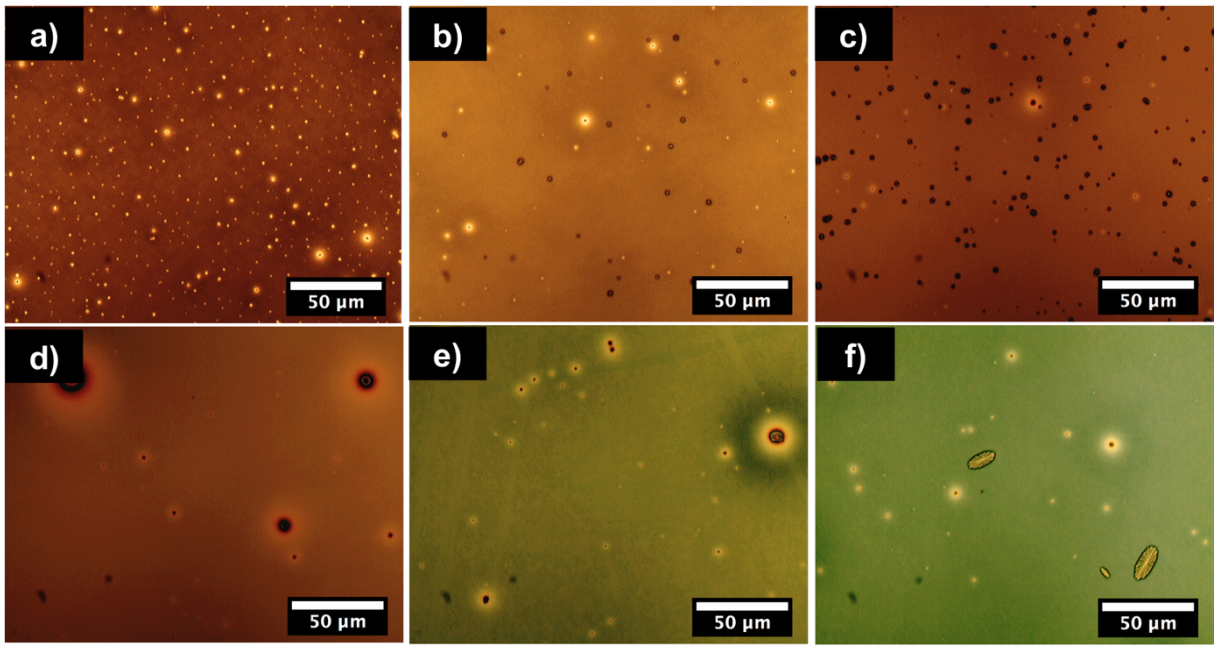

Figure 5.8: Optical microscopy images of the resulting P3HT-*b*-PS:PCBM blend films with a PCBM weight fraction of a) 9, b) 25, c) 33, d) 50, e) 58 and f) 67%. Reproduced from Ref. [110] with permission from the Elsevier B.V.

Figure 5.8 exhibits the micrometer scale surface structure of P3HT-*b*-PS:PCBM blend films with varying PCBM weight fractions. A uniform morphology within a relatively large area is observe for all samples at the applied scanning resolution. In addition, distinct clusters are revealed on all the sample surfaces, which are attributed to the PCBM crystallized agglomerates formed upon thermal annealing. [144, 145] The bright spots are steadily transforming into large dark crystals due to the increased crystal thickness at higher PCBM content. It was reported that the film/air surface offers space for crystal growth and thus leading the nucleation of crystal formation. [145] Notably, above a PCBM weight fraction of 33%, dark depletion areas become apparent around the bright PCBM crystals, which indicats that the PCBM crystals grow in size and stick out of the thin film surface plane. [144] At a PCBM weight fraction of 67%, enlongated flower-like PCBM crystals are observed. A similar result was reported by Wang et al. in the P3HT:PCBM BHJ system with organic solvent vapor post-treatment after thin film deposition. [132] However, these large crystals are not favorable in photovoltaic application since short circuits can form between the anode and the cathode.

To gain further insight into the surface morphology on the nanomater scale, all the blend films are probed by AFM. As shown in Figure 5.9a-f, the PCBM content has a strong

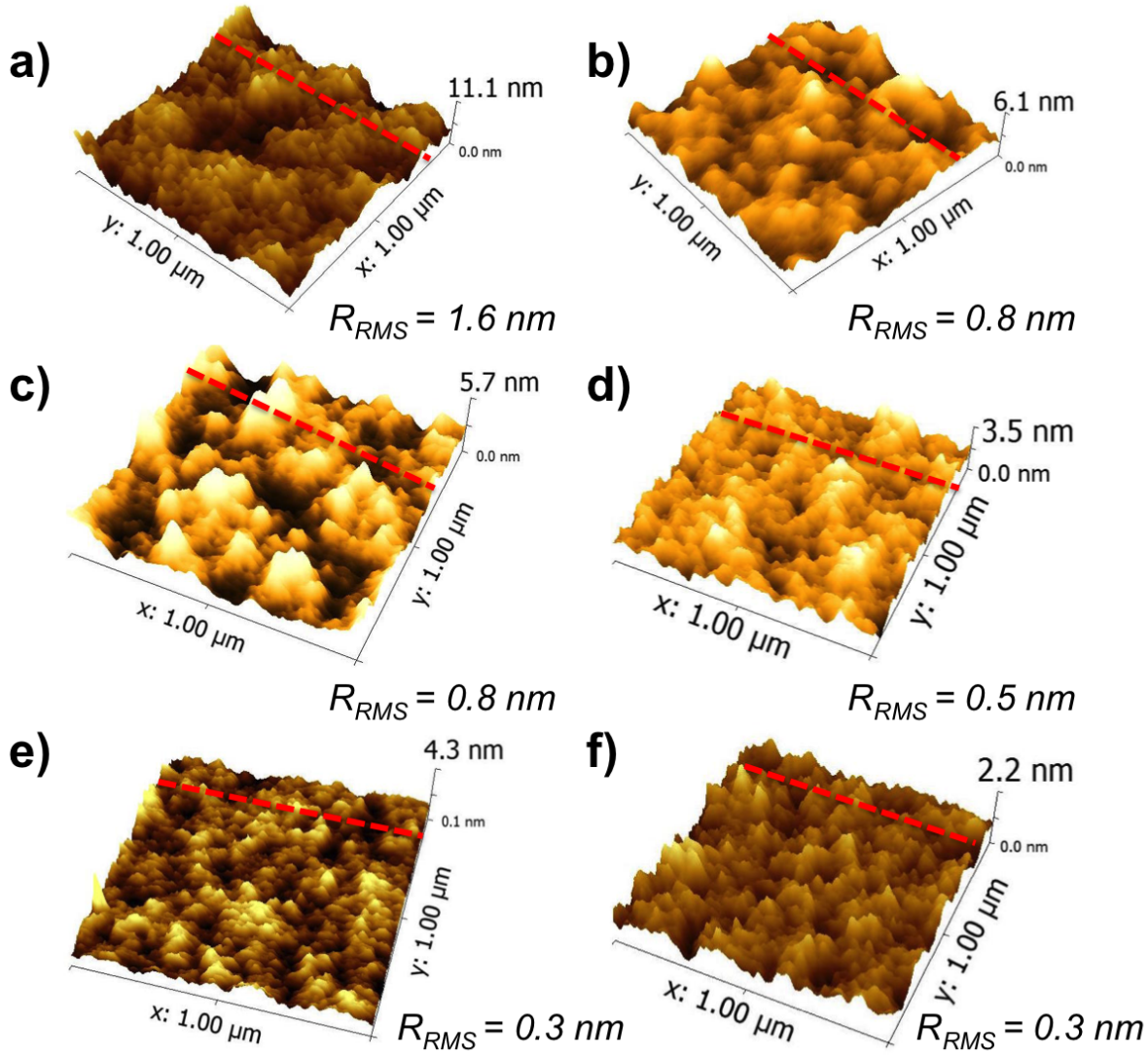

Figure 5.9: AFM topography images measured at a scan range of 1×1 μm^2 of the P3HT-*b*-PS:PCBM blend films with a PCBM weight fraction of a) 9, b) 25, c) 33, d) 50, e) 58 and f) 67%. The calculated RMS roughness values are indicated.

influence on the surface morphology. For the sample containing a PCBM weight fraction of 9% (Figure 5.9a), the surface is very rough with a root mean square (RMS) roughness value of 1.6 nm. The surface becomes smoother with increasing PCBM content. For the sample with the highest PCBM content (67%, Figure 5.9f), a RMS roughness of 0.3 nm is revealed. For a more detailed analysis, line profiles are taken on the individual samples (Figure 5.10). Stripe-like nanoscale fine structures around 20 nm width are revealed in sample contains a PCBM weight fraction of 9%. These fine structures disappear upon increasing the PCBM weight fraction up to 50% and is recovered in samples with PCBM weight fraction above 50%. In addition, hundreds of nanometer aggregates are observed at 33%, which are

likely due to the diblock copolymer self-assembly aggregation. Additional information on surface morphology are determined in the AFM phase images (Figure 5.11).

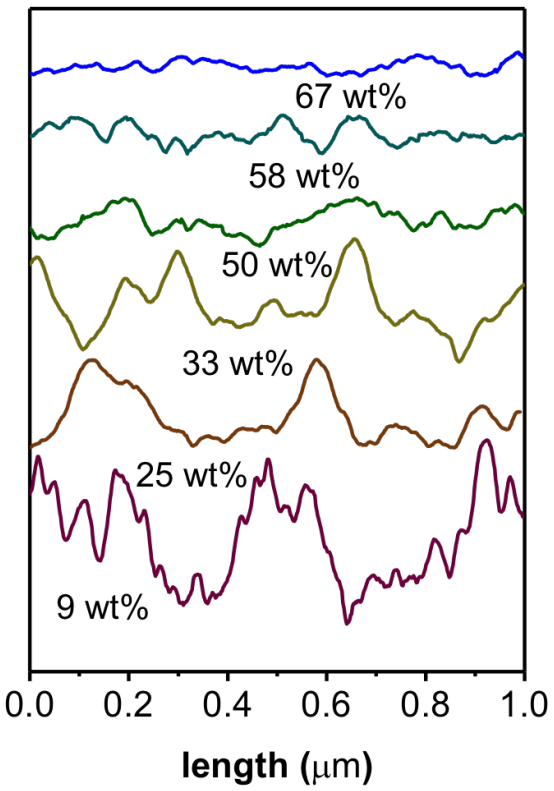

Figure 5.10: Line profiles of the six different composition samples extracted at positions marked with red dash lines in Figure 5.9.

In Figure 5.11a, microphase-separated randomly distributed lamellae structures are found which resemble well the morphology of the pure diblock copolymer film (Figure 5.12a). As it was already reported, these features comprise P3HT crystals. [146, 147] Upon further increasing the PCBM weight fraction up to 33%, the bright lamellae become less developed, as sizes of both length and width are diminished. This feature implies the crystallization mechanisms of the P3HT block are effected by the content variation of PCBM, which is in good agreement with the GI-XRD results. For samples with a PCBM weight fraction above 50%, the lamellar morphology is recovered, although the width is increased (Figure 5.11d,e). In Figure 5.11f, the surface structure in the sample containing the highest PCBM content becomes featureless and no distinguishable nanomorphology are visible at this probing length. For a quantitative analysis of structure

sizes, the power spectral density (PSD) curves are calcuated from the AFM topography data (Figure 5.12b).

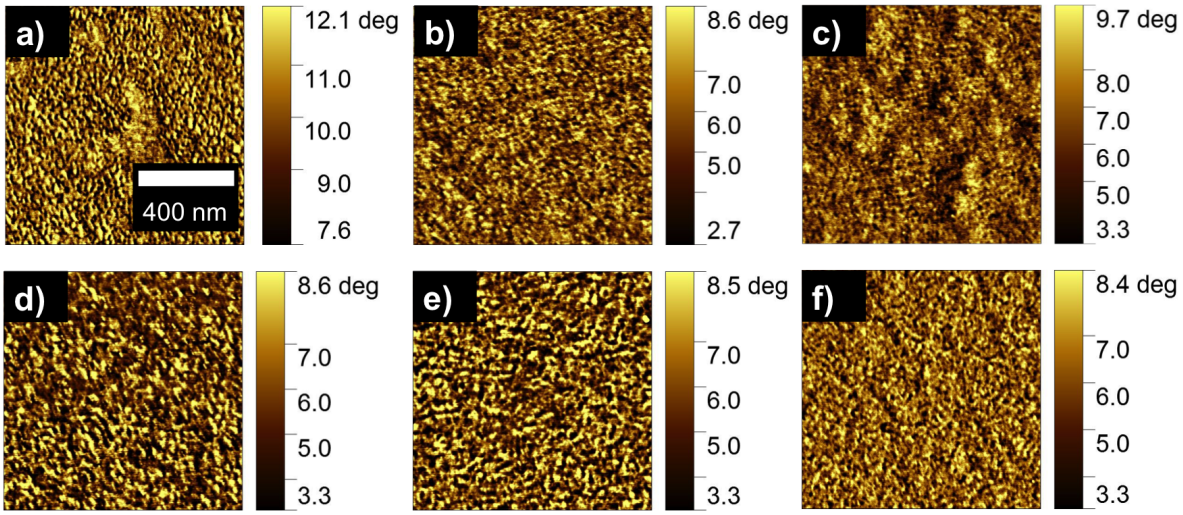

Figure 5.11: AFM phase images measured at a scan range of 1×1 μm^2 of the P3HT-*b*-PS:PCBM blend films with a PCBM weight fraction of a) 9, b) 25, c) 33, d) 50, e) 58 and f) 67%. Shift of phase angle is individually chosen as indicated. Reproduced from Ref. [110] with permission from the Elsevier B.V.

The characteristic peak and shoulder displayed in the PSD curves represent a corresponding characteristic length scale inside the sample. In Figure 5.12, a distinct shoulder-like intensity contribution is identifiable in the sample with the lowest PCBM weight fraction (9%), which shifts towards smaller q values with increasing PCBM content and also becomes less pronounced. Hereby, the characteristic length scale in the P3HT-*b*-PS:PCBM blend films increases at higher PCBM content and the corresponding surface structures are less well developed. In addition, the revealed morphology parameters are restricted to the sample surface.

5.3.3 Lateral structure

To gain a full understanding of the 3D morphology with higher statistics, GISANS measurements are performed to probe the buried lateral structures within the blend films. In the traditional P3HT:PCBM BHJ system, it was reported that a mixed phase of PCBM and polymer is coexisting with the pure P3HT and pure PCBM phases. [148] Consequently, the scattering contrast condition in the studied system is enhanced.

In Figure 5.13, the obtained 2D GISANS data of P3HT-*b*-PS:PCBM blend films with six different PCBM weight fractions are shown. Above the sample horizon, the recorded

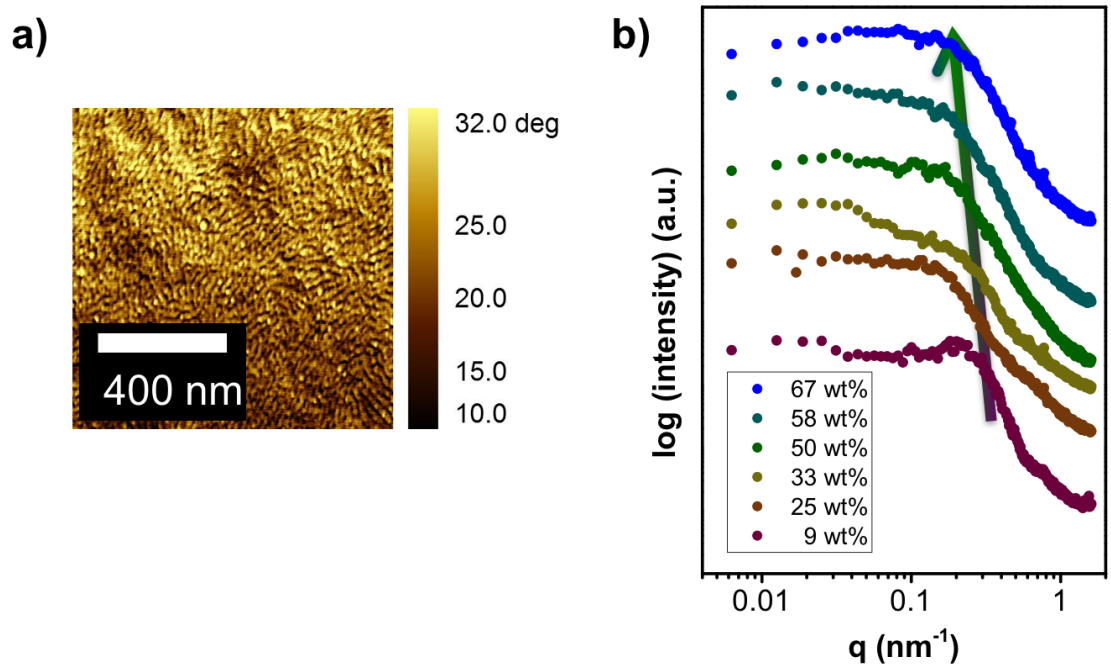

Figure 5.12: a) AFM phase image of neat P3HT-*b*-PS film measured at 1×1 μm^2. b) Power spectral density (PSD) curves calculated from AFM phase images (Figure 5.11). An arrow highlights the trend of the characteristic structure peak fading away with increasing PCBM content. Data are displayed in a double logarithmic presentation.

scattering intensities alter along the in-plane direction (q_y) rather than the surface normal (q_z), indicating a composition dependent lateral structure at different blend ratios. Upon increasing the PCBM content, a wing-like scattering feature arises along the q_y direction, which generates from the contrast enhanced nano-scale morphology within the samples. In more details, in samples containing PCBM weight fraction higher than 50% (panels d,e,f), the scattering intensity of these wing-like features segregates. Moreover, intensive peaks at $q_y \approx \pm 0.2$ nm^{-1} emerge in the sample containing the highest PCBM weight fraction (panel f, 67%). This observed result suggests that the interaction between P3HT-*b*-PS and PCBM promotes the development of microstructures with well-ordered correlation length. Notably, interesting scattering features are also generated in transmission signals alongside the altering of PCBM content. A scattering pattern of hexagonally packed cylinder morphology is observed in the sample with a PCBM weight fraction of 67% (panel f). The scattering pattern is not observed above sample horizon due to the limited GISANS statistics. In addition, more intensive peaks are distributing in the reflected signals rather than the transmitted signals, suggesting that the hexgonally packed

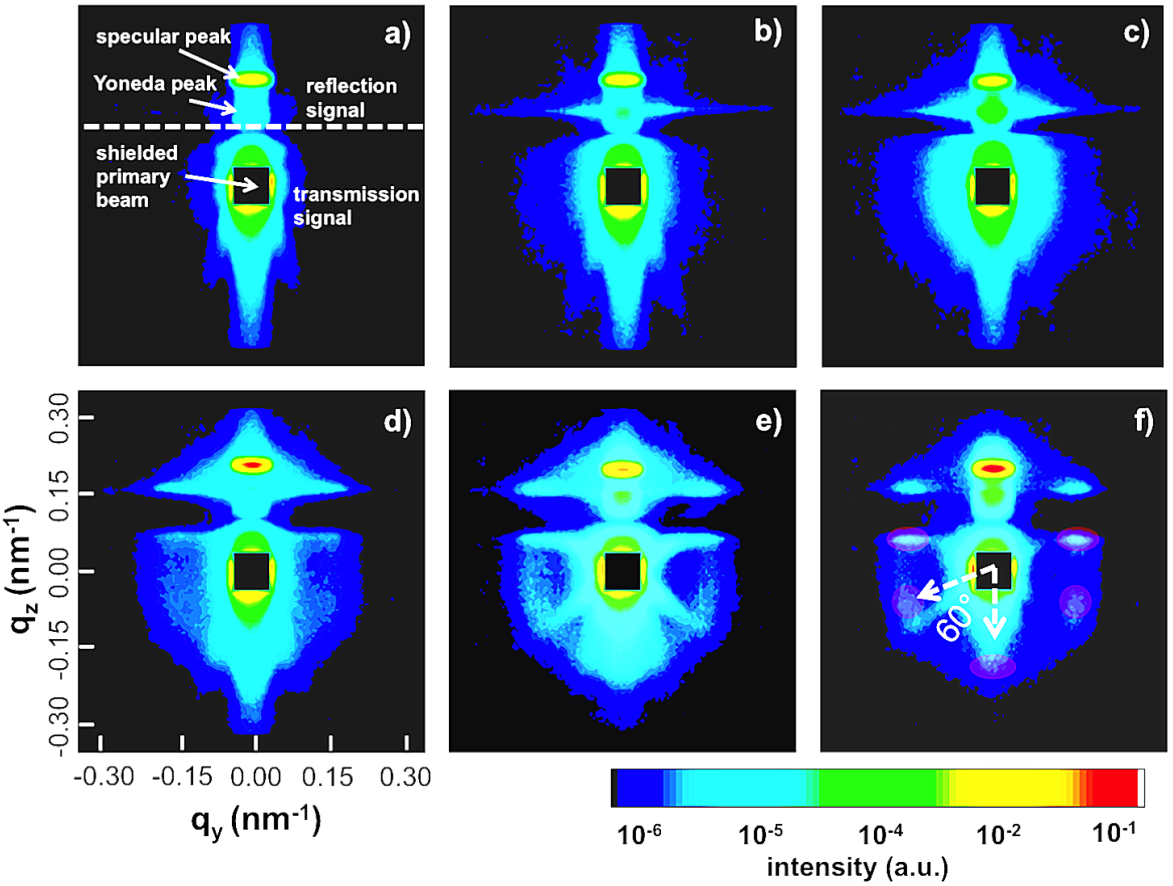

Figure 5.13: Two-dimensional (2D) GISANS data of P3HT-*b*-PS:PCBM blend films with a PCBM weight fraction of a) 9, b) 25, c) 33, d) 50, e) 58 and f) 67%. In panel a, a horizontal dashed line is used to mark the sample horizon to identify the reflection intensity and the transmitted intensity. The components of the scattering vector q_y and q_z represent the directions horizontal and normal to the sample surface, respectively. Distinct scattering features are indicated in panel a. Reproduced from Ref. [110] with permission from the Elsevier B.V.

cylinders present more close to the film surface. For a detailed quantitative analysis of the scattering data, vertical cuts along $q_y = 0$ and horizontal line cuts along the Yoneda peak positions are performed for all the six samples.

In Figure 5.14a, the Yoneda peak shifts to a larger q_z value upon increasing the PCBM weight fraction. Compared to P3HT-*b*-PS, PCBM possesses a larger value of neutron scattering length density (SLD_n) (Table 5.2). The shift of Yoneda peak reveals the amount of PCBM embedded in the diblock copolymer. [98] Another interesting feature is observed with increasing the PCBM content. A broad shoulder-like peak at $q_z \approx$ -0.2 nm^{-1} steadily develops at PCBM weight fraction above 50%, which is identical to the q_y position of the side maximum peaks along the horizontal line cuts. Considering the unambiguous change of the molecular order of P3HT block observed from GI-XRD (Figure 5.1a), we speculate

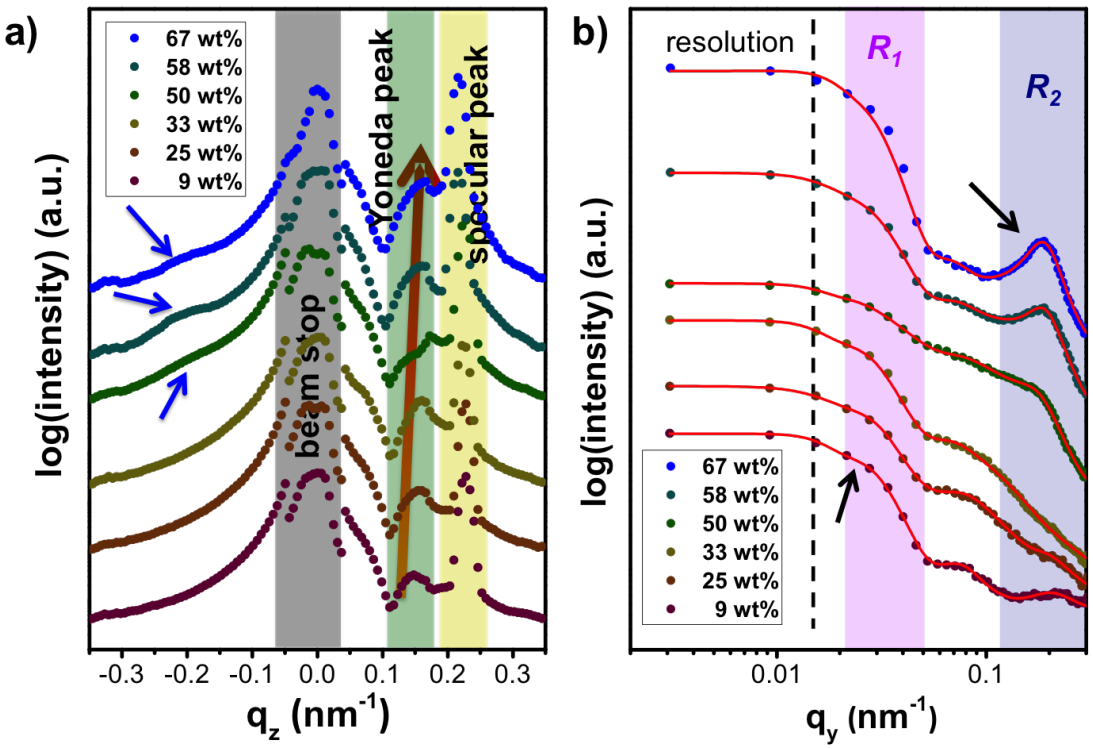

Figure 5.14: a) Veritical line cuts along $q_y = 0$ nm^{-1} of blend films with six different PCBM weight fractions. The distinct scattering features of the beam stop, the Yoneda peak and the specular peak are marked with black, green and yellow boxes, respectively. An purplish arrow highlights the shift of Yoneda peak position. The shoulder like scattering peaks in sample 50%, 58% and 67% are indicated by blue arrows. b) Horizontal line cuts along the Yoneda peak positions of blend films with PCBM contents as indicated. The extracted data is displayed associated with the red fit lines. The two mesoscale (R_1) and nanoscale (R_2) substructures applied in the data fitting are indicated with arrows and highlighted with colored boxes. The dash line marks the resolution limit. Images adapted from Ref. [110].

that a phase transition process from a lamellar- into a cylindrical-morphology occurred within the diblock copolymer P3HT-b-PS at a PCBM weight fraction higher than 50%. In order to have a deeper understanding about the resulting morphological parameters at different compositions, a fitting model using two cylinder-like substructures are applied to represent the mesoscale and nanoscale in-plane domains within the samples. The morphological parameters are determined in terms of domain sizes and the associated spatial distribution of the domains.

In Figure 5.15b, the revealed domains (S_1) are around 120 nm on the mesoscale, which is

	SLD_n (10^{-6} Å^{-2})
P3HT-*b*-PS	0.914
PCBM	4.3

Table 5.2: Summary of the neutron scattering length density (SLD_n) of P3HT-*b*-PS and PCBM.

similar to the length scale previously reported for homopolymer P3HT:PCBM blends. [98] The unusually value at 50% can be ascribed to the starting of the morphology transformation. From the literature, it is well established that the scattering intensity correlates to the SLD_n difference in the studied system. [149, 150] Hence, the difference in scattering intensity can be used as a probe to determine the mixing between the PCBM and the diblock copolymer. A increasing scattering intensity can be ascribed to a system with better contrast condition while a decreased value reveals a better mixture of PCBM and P3HT-*b*-PS. The average scattering intensity originates from the mesoscale domains regime R_1 in Figure 5.15b, and are plotted in Figure 5.15a as a function of PCBM weight fraction. The extracted value increases by about 8 times from 9% to 33% sample. This indicates that a well phase separated morphology of PCBM and P3HT-*b*-PS is formed in the sample with a PCBM weight fraction of 33%. However, this value quenches dramatically upon increasing the PCBM weight fraction to 50%. The mobility of PCBM is higher than that of the polymer. [11] Therefore, the observed low contrast at 50% suggests the formation of PCBM crystals in between polymer domains on hundred nanometer scale. This result is identical to our observed PL spectra (Figure 5.5). Better phase separated morphology in samples with PCBM weight fractions 25% and 33% restricts the exciton dissociation, whereas fast photoinduced charge transfer occurs in sample 50%. By further increasing the PCBM weight fraction above 50%, segregated PCBM domains present on the mesoscale. However, with respect to the important exciton dissociation length scales on the order of 10 nm [151], it is crucial that scattering features from smaller domains are determined.

In Figure 5.14b, a shoulder like scattering feature is visible at $q_y \approx 0.2$ nm^{-1}, being indicative to a spatial correlation length of around 30 nm. On the basis of the molecular structure of P3HT-*b*-PS and the GI-XRD result, we speculate that the diblock copolymer adopts a lamellar morphology which is driven by the P3HT block crystallization. The shoulder-like scattering feature loses intensity upon increasing the PCBM content till 33%, while surprisingly recovers in intensity at 50%. Furthermore, intensive scattering peaks can be seen in samples with PCBM weight fractions of 58% and 67%. The full width at half maximum (FWHM) of the scattering peak determines the degree order of the block copolymer. A smaller value of FWHM reflects a system with well developed ordering

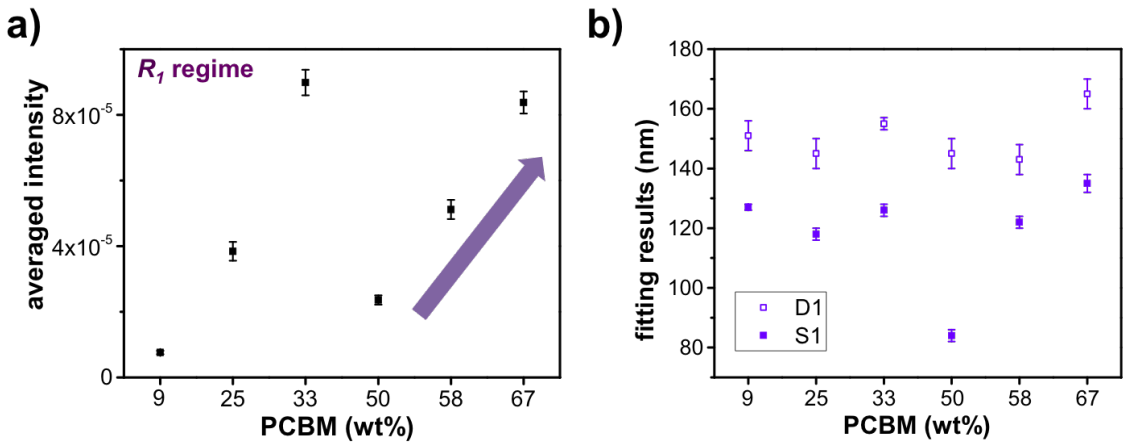

Figure 5.15: a) Average scattering intensities by normalized the recorded intensity for each blend sample in R_1 regime in Figure 5.14b to 1 hr counting time. A purple arrow highlights the contrast development in samples containing PCBM weight fraction above 50%. b) The extracted domain sizes (S_1) and the distances (D_1) between different domains for the mesoscale substructure in the blend films. Images adapted from Ref. [110]

morphology. [131, 152, 153] Guassian peaks are used to represent the scattering feature at R_2 regime in Figure 5.14b, the extracted FWHM values are shown in Figure 5.16a. The P3HT-*b*-PS:PCBM blend films lose structure ordering with increasing the PCBM weight fraction from 9% to 33%, but this, reverses upon further increasing the PCBM content above 50%. Taking into account that the crystallinity of the P3HT block decreases in the 67% sample with respect to that in sample 50%. We estimate that the better spatial correlation order in sample 67% results from the beneficial impact of the P3HT-*b*-PS microphase separation. A similar result was reported by in their study of diblock copolymer and homopolymer blends. [154] However, the absence of gyroid nanostructure during morphology transformation is speculated due to the weak driving force of the gyroid phase. [155]

The domain size (S_2 in Figure 5.16b) revealed from the fitting model increases from 13 ± 2 nm to 21 ± 0.5 nm for a PCBM weight fraction increasing from 9% to 67%. Thus, the PCBM is incorporated in the P3HT-*b*-PS alongside the block copolymer domain swelling. In addition, distances between the copolymer domains are also increasing with higher PCBM content. To deepen these findings, a simplified comparison between one-dimensional surface area ratio (ξ) of one diblock cylinder to the hexagonal lattice matrix is performed as illustrated in Figure 5.17a for samples with a PCBM weight fraction above 50%. The applied model can be described in equation

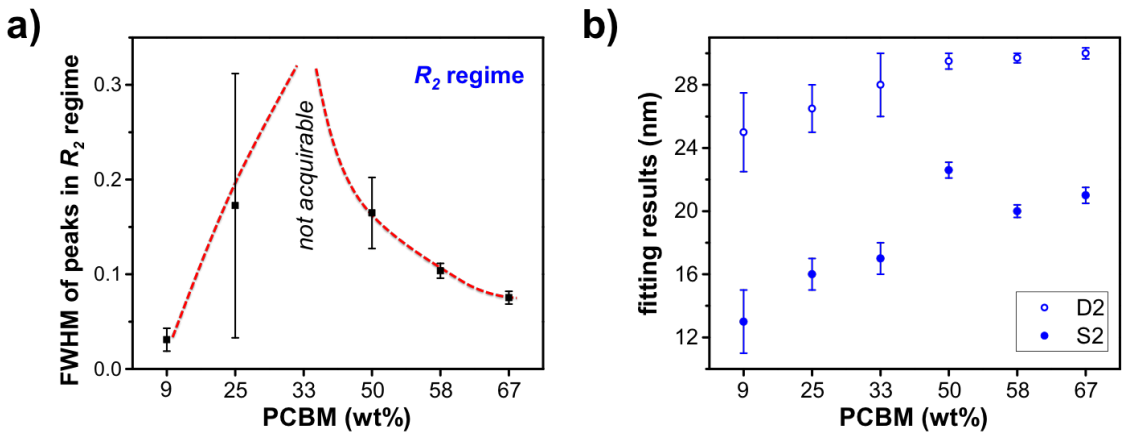

Figure 5.16: a) Full width at half maximum (FWHM) of the scattering peaks and b) the morphological parameters extracted from fittings in R_2 regime in Figure 5.14b. The revealed data is plotted as a function of different PCBM weight fractions. Reproduced from Ref. [110] with permission from the Elsevier B.V.

$$\xi = \frac{3\pi {R_1}^2}{\pi {R_2}^2} \tag{5.3}$$

where R_1 and R_2 denote the radii of one single cylinder and three cylinders, respectively. Taking the morphological parameters S_2 (domain size) and D_2 (domain distance) obtained from GISANS data fitting to represent R_1 and R_2, equation 5.3 can be rewritten to

$$\xi = \frac{3\left(\frac{S_2}{2}\right)^2}{\left(\frac{D_2}{2\cos 30°} + \frac{S_2}{2}\right)^2} \tag{5.4}$$

The obtained values shown in Figure 5.17b elucidate that the PCBM domains leaving hexgonal packed cylinder lattice upon increasing PCBM weight fraction from 58% to 67%.

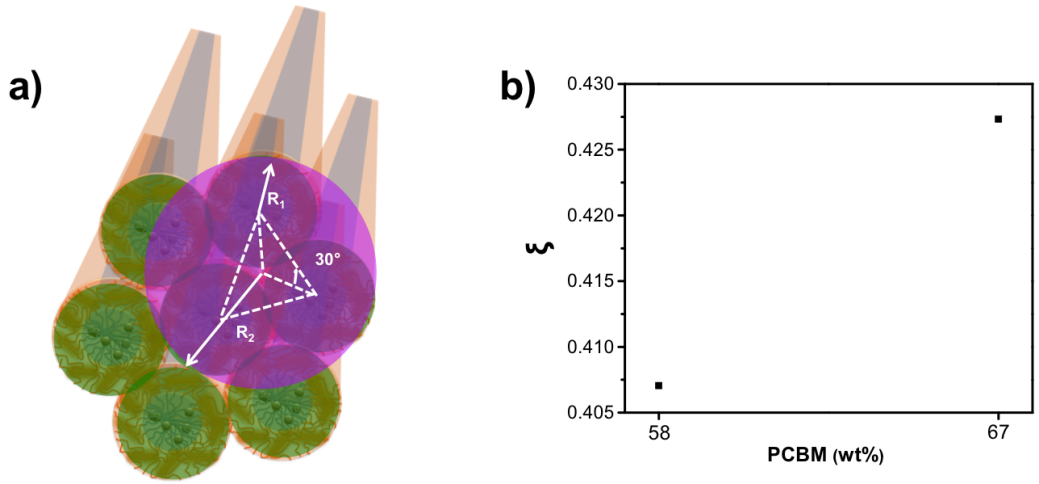

Figure 5.17: a) Schematic description of equation 5.4. The surface areas of one cylinder and three cylinders are indicated with green and purple circles, respectively. b) Estimation of surface area ratio (ξ) of one cylinder to a three cylinder lattice for samples containing PCBM weight fractions of 58% and 67%. Reproduced from Ref. [110] with permission from the Elsevier B.V.

5.3.4 Results

The morphology evolution in P3HT-*b*-PS films upon the addition of PCBM is schematically illustrated in Figure 5.18. The local film morphology can be identified in four different stages: (1) The P3HT-*b*-PS:PCBM blend film preserves a lamellar morphology in conformity with the pure diblock copolymer at the lowest PCBM weight fraction (9%), which is driven by the P3HT block crystallization. At this composite, PCBM tends to interact with the PS block with poor crystallization degree and distributes near the substrate surface; (2) Upon increasing the PCBM content (25% and 33%), PS block swells to accommodate the PCBM whereas the nanoscale morphology in the blend becomes less developed and the kinetically favored face-on P3HT orientation appears as revealed in GI-XRD. Meanwhile, the extra PCBM molecules appear to present in the bulk; (3) For even higher PCBM weight fractions (50%, 58%), larger PCBM aggregates present among the polymer domains on the mesoscale, as the GISANS contrast diminishes. In addition, the diblock copolymer phase transition occurs; (4) For sample containing the highest PCBM weight fraction (67%), segregated PCBM domains are better developed on the mesoscale whereas large PCBM aggregates appear on the film surface. The cylindrical diblock copolymers are distributed in a well organized hexagonal lattice.

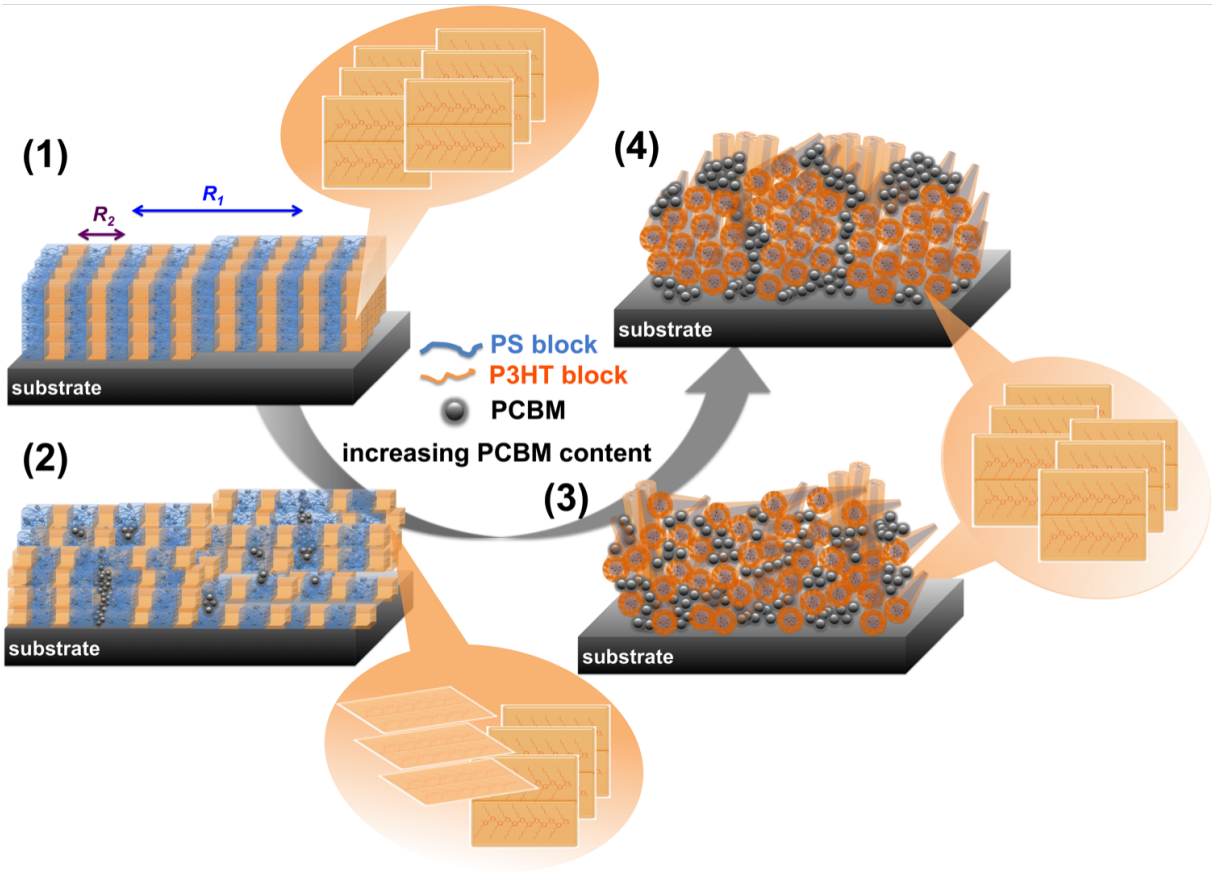

Figure 5.18: Schematic illustration of the morphology dependance of P3HT-*b*-PS films on the addition of PCBM. The two blocks of the diblock copolymer are depicted in orange (P3HT) and blue (PS) whereas PCBM is shown as black spheres. P3HT crystalline orders are depicted in a zoom-in view. Films with higher PCBM content exhibit a better segregated domain structure on the hundred nanometer scale as well as a hexagonally packed cylinder morphology. Reproduced from Ref. [110] with permission from the Elsevier B.V.

5.4 Summary

In this chapter, the influence of PCBM addition on the crystalline structure, the opto-electronic properties and the mesoscopic morphology of P3HT-*b*-PS bulk heterojunction systems are investigated. The crystallinity of the P3HT block, the fluorescence intensity as well as the ordering degree of the nanoscale morphology in the P3HT-*b*-PS:PCBM blends are revealed to exhibit nonmonotonic dependence on the increasing of PCBM content. Different mechanisms are proven to drive the formation of the final morphology. Interestingly, it has been demonstrated that the exact morphology resulting from the interaction between PCBM and P3HT-*b*-PS has a direct impact on the exciton dissociation

in the blend films. For full understanding, the complete vertical and lateral morphology have been determined.

The findings indicate that the crystallinity of P3HT block is perturbed by adding the PCBM till a threshold weight fraction of 33%. Simultaneously, the kinetically favored face-on orientation appears, which consequently destroys the well-ordered lamellar morphology that developed in sample with a PCBM weight fraction of 9%. Upon further increasing the PCBM content above that value, the microphase separation dominates the morphology evolution in the P3HT-*b*-PS:PCBM blends whereas, a hexagonally packed cylinder morphology is revealed in sample with a PCBM weight fraction of 67%. GISANS reveals that better segregated domains are formed on the mesoscale for samples with a higher PCBM content. Notably, the microphase separation induced domains distribute on a length scale of around ten to twenty nanometer, which increase in size upon the addition of more PCBM into the BHJ films.

The free exciton bandwidths are determined by a weakly coupled H-aggregated model. Combining all our observations, we propose that blend films with a PCBM weight fraction higher than 50% appear promising with respect to the potential application of the studied system in organic solar cells. Last but not least, an optimization of the diblock copolymer molecular structure might be necessary to guarantee the achievement of a outstanding working device. Such studies reported here could provide an alternative view to select promising candidates to be further processed into optoelectronic devices in the future.

6 Nanostructuring of mixed dimensional lead bromide perovskite thin films

Parts of this chapter have been published in the article: Preferential Orientation of Crystals Induced by Incorporation of Organic Ligands in Mixed-Dimensional Hybrid Perovskite Films. [156] (R. Wang et al., Advanced Optical Materials, 2018, 6, 1701311.)

Organometal halide perovskite, the new-born old materials have gathered considerable attention among researchers as photoactive materials for optoelectronic applications. The early studies of perovskite materials date back to late 1980s, when the research focused mainly on their intriguing dielectric properties. [12] However, these materials also exhibt many remarkable properties, such as a tunable band structure to secure optical absorption upon the entire solar spectrum, [13] a long charge-carrier diffusion length over 1 µm, [64] the ambipolar charge-transport property, [157, 158] an outstanding photoluminescence quality (full width at half maximum, FWHM $\approx$ 20 nm), [159] and a small capture cross-section of trap states. [160] Consequently, all these intrinsic characteristics have manifested perovskite materials as a versatile candidate for optoelectronics, for example as solar cells, [52, 161–164] light-emitters, [53, 165, 166] lasers, [54, 167] and photodetectors. [168, 169]

The chemical formula of organometal halide perovskite materials is adopted from the calcium titanate ($CaTiO_3$) crystal structure, which is generally labeled as ABX_3. In perovskite crystals, A is 12-fold cubooctahedral coordinated with X anions among $[BX_6]^{4-}$ octahedral clusters that generating a 3D ABX_3 crystalline frameworks [170,171]. Notably, by choosing appropriately large size organic cations, such as octylammonium ($CH_3(CH_2)_7NH_3^+$), butylammonium ($CH_3(CH_2)_3NH_3^+$) or benzylammonium ($C_6H_5CH_2NH_3^+$) [15, 172, 173], the 3D bulk perovskite crystal can be synthetically altered into 2D layered platelets (so-called as Ruddlesden–Popper perovskite), [15, 174–176] 1D nanowires, [177, 178] and even 0D nanoparticles. [14] Due to the intrinsically large size, the long organic cation cannot diffuse in between the $[BX_6]^{4-}$ octahedra slabs and therefore terminates the 3D crystal

growth. In the 2D structure, the $[BX_6]^{4-}$ octahedra are distributed in layers and separated by the organic dielectric layers whereas in the 1D structure the $[BX_6]^{4-}$ octahedra are connected in chains. In the 0D structure, the $[BX_6]^{4-}$ octahedra are isolated and surrounded by organic cations. The resulting size of low-dimensional perovskite can be tuned to as small as one atomic layer thin. As a consequence, quantum-size effects as well as advanced photoelectric properties are achievable.

Among the aforementioned low-dimensional perovskite structures, 2D layered perovksite have gained increasing interest due to the following reasons: (1) electrons are confined into planes without interlayer interactions, which generates prospects for advanced microelectronics; (2) weak interaction is possessed among interlayers whereas the in-plane skeleton is mainly confined by van der Waals forces, which can provide good mechnical properties; (3) thin-film structure in atomic level making them applicable in transparent and flexible devices.

Our approach in this present chapter is to leverage this concept, aiming combine the advantages of 3D and 2D perovskite crystals. Herein, organic ligands of methylammonium bromide (MABr) and octylammonium bromide (OABr) with a various ratios are prepared to achieve mixed-dimensional (a combination of both 3D bulk and 2D layered perovskite crystals) perovskite films. The long organic ligand OABr is expected to affect the film morphology. Referring to the applied OABr mole ratio, samples are named as PeOA0 (0%), PeOA10 (10%), PeOA20 (20%), PeOA40 (40%) and PeOA100 (100%). In this chapter, the dependence of the optical properties of resulting thin films on the tailored morphology are investigated. The optical properties of the mixed dimensional perovskite films with respect to the optoelectronic properties as well as the photoemission dynamics (Section 6.1). This is followed by a thorough morphological investigation (Section 6.2) and the ASE properties (Section 6.3). The results obtained imply good expectation of using these mixed dimensional perovskite films within optical gain devices.

6.1 Optical properties

6.1.1 Optoelectronic properties

In order to quantify the optical electronic properties of the resulting mixed dimensional perovskite thin films, UV-Vis absorption and photoluminescence (PL) spectroscopies were employed. Figure 6.1 displays the obtained data. Changes in absorption and fluorescence results originate from the compositional variation are observed.

As shown in Figure 6.1a, the absorption spectrum of sample that prepared using neat OABr (PeOA100) is dominated by a single sharp excitonic feature at 396 nm, which can

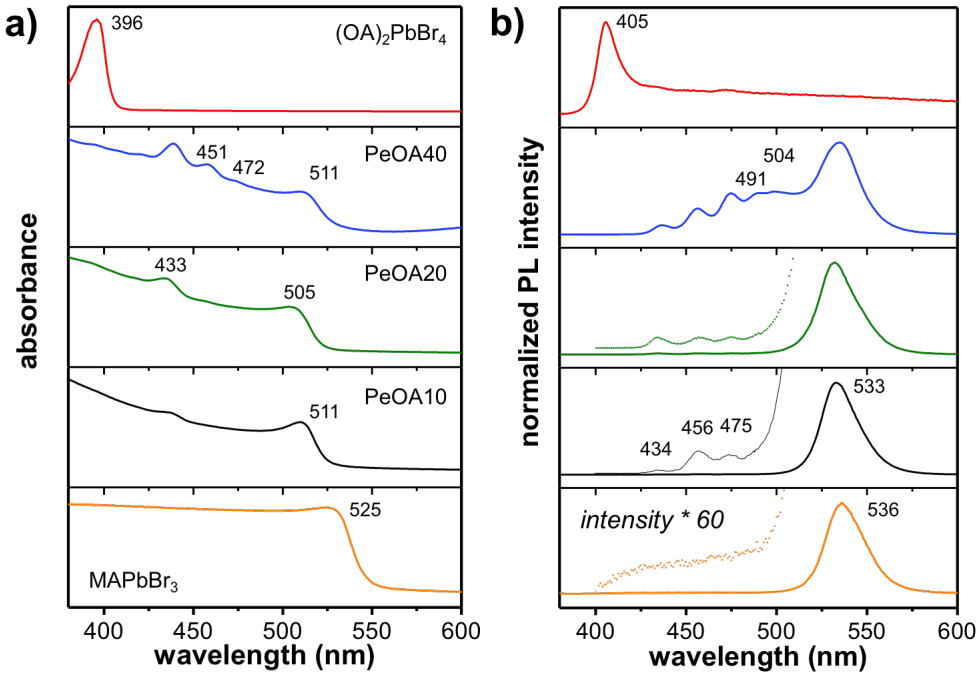

Figure 6.1: a) UV-Vis and b) PL spectra of the resulting samples with varying OABr contents. PL peaks lie to the higher energy edge are magnified and displayed in dash lines, which can be attributed to the 2D perovskite platelets. Spectra for 3D bulk $MAPbBr_3$ (PeOA0) and 2D layered $(OA)_2PbBr_4$ (PeOA100) perovskite are presented as well to illustrate better comparison. Prominent peak positions are marked in the curves. Reproduced from Ref. [156] with permission from the John Wiley & Sons, Inc.

be ascribed to exctions formed inside the thin $(OA)_2PbBr_4$ layers. [179] The sample containing an OABr mole ratio of 10% (PeOA10) exhibits a main band edge around 511 nm, in consistent with the 3D $MAPbBr_3$ bulk crystals but slightly blue-shifted. More specifically, further contribution arised at around 433 nm, which can be attributed to the 2D perovskite platelets with one perovskite unit cell (n) thickness. [180] Upon substituting MABr with OABr, additional sharp excitonic absorption features become more apparent in the absorption spectra at 396, 451 and 472 nm, indicating that quantum confinement arises inside the films. [15, 16] From the literature, these peaks are identifiable as 2D perovskite platelets with perovskite unit cell thickness (n) of 0, 3 and 4, respectively. [15, 16] The 0 value of unit cell thickness represents 2D platelets of one single layer of corner shared $[PbBr_6]^{4-}$ octahedra which is isolated by organic cations. Interestingly, the absorption maximum within the mixed dimensional perovskite thin films do not show a monotonic blue-shift behavior. However, the absorption maximum first blue-shifts from 511 nm in sample PeOA10 to 505 nm in sample PeOA20 and returns backward to 511 nm in sample

PeOA40. This result suggests that the interaction between 2D and 3D perovskite crystals becomes weaker when increasing the OABr mole ratio from 20% (PeOA20) to 40% (PeOA40). Here, we propose that the 2D platelets firstly coexistent with 3D crystals by surface adsorption (in sample PeOA10 and PeOA20), and the interaction becomes weaker in sample PeOA40 with further increasing OABr content. A further discussion is carried out in the following section (Section 6.2.1).

Figure 6.1b displays the PL emission spectra of samples with a variation of OABr mole ratio. In sample PeOA10, the emission peak is blue-shifted by 3 nm as compared to the 3D bulk $MAPbBr_3$ whereas additional higher energy emission peaks appeared. These peaks can be ascribed to the aforementioned 2D perovskite platelets with perovskite unit cell thickness of n = 1 (434 nm), n = 3 (456 nm), and n = 4 (475 nm). [16] In sample with the highest OA content (PeOA40), thicker 2D platelets with n = 5 (491 nm) and n = 6 (504 nm) perovskite unit cell are seen. [16] Meanwhile, although 2D platelets 1 unit cell thick contribute a strong absorption peak in sample PeOA10, the corresponding PL emission intensity is relatively weak. This result suggests that the energy transfer is efficient in sample containing the lowest OABr content, which will be further discussed in section 6.3. [181, 181] Upon further substituting of MABr with OABr to a value of 20%, the main emission peak becomes broader and the higher energy emission peaks increase in intensity. In the sample containing an OABr mole ratio of 40% (PeOA40), the emission peaks of 2D platelets are clearly identifiable with no magnification. This is consistent with the absorption result that the 2D platelets are first adsorbed on the 3D crystal surface, and with a further increase in OABr content, the 2D platelets form as isolated aggregates.

Considering that OABr and MABr exhibit different crystallization mechanisms on the perovskite crystal, double side PL measurements are performed to investigate how these lower dimensional perovskite crystals grow inside the film. In Figure 6.2a, in contrast to the front excitation (from the air-film interface), the back excitated (from the substrate-film interface) PL spectra of the sample PeOA10 exhibits distinguishable emissions at the higher energy side. This observation indicates that a larger content of 2D perovskite platelets are located closer to the substrate in comparison to the air. Notablly, the 3D crystals are speculated to grow on top of the 2D platelets as the main emission peak (533 nm) presents a stronger blue-shift in the back excitation spectra. However, with increasing the OABr content to 40%, the 2D platelets are distributed all along the film with no remarkable differences on the main emission peak. Therefore, we estimate that the 2D platelets prefer to locate close to the substrate side in sample containing a lower OABr content whereas this preferential distribution disappears with increasing the OABr content. This result is in good agreement with the GIWAXS results as presented in Section 6.2.

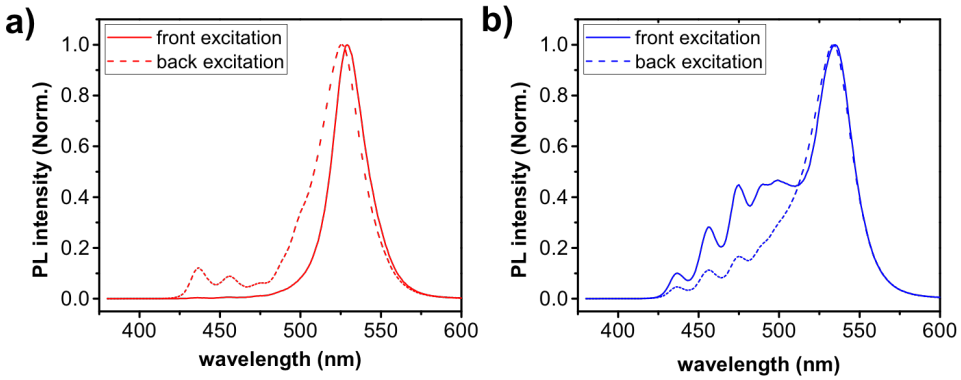

Figure 6.2: PL spectra of samples a) PeOA10 and b) PeOA40 obtained by photoexcitation from the air-film (front excitation) and the substrate-film (back excitation) interfaces.

6.1.2 Time-resolved photoemission dynamics

In order to further quantify the PL kinetics inside the mixed dimensional perovskite samples, time-resolved fluorescence measurements were carried out. The obtained results reveal that the variation of OABr content stark affects the PL decay lifetimes. To have an integrated comparison, the individual samples are compared by assessing the time by which the intensity dropped to $1/e$ of its original intensity (Figure 6.3a). As shown in Figure 6.3b, the PL decay time for sample PeOA10 is remarkably extended as compared to the neat 3D bulk perovskite $MAPbBr_3$. This result suggests that OABr might enhance the surface passivation effect and simultaneously reduce the trap-assisted recombination. [182, 183] However, upon further increasing the OABr content, the fluorescence spectra decays faster. From the optical spectra presented in Section 6.1, we speculate that a larger amount of perovskite platelets are formed in samples with higher OABr content. Therefore, the decreased PL lifetimes can be resulted from the increased exciton binding energy through the transition from a 3D bulk-like perovskite in to a mixture of 3D/2D multi-dimensional perovskite system. [184] Additionally, the PL quantum yields (PLQY) in the mixed dimensional perovskite samples progressively increases with increasing the OABr content. This result can be ascribed to 3D perovskite crystal growth confined by a high amount of organic bulky ligand OABr. As a consequence, the surface of perovskite nanocrystals is passivated. [185] However, a determination of radiative and non-radiative decay rates is not possible due to the dimensionally inhomogeneous in samples. [186] A full summary of the extracted parameters are listed in Table 6.1.

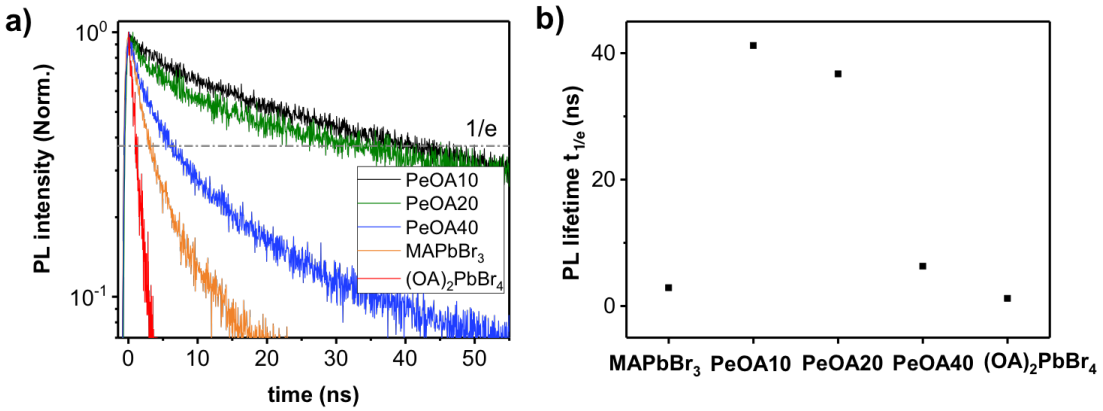

Figure 6.3: a) PL dynamics of resulting perovskite films with varying mole ratio% of OABr. Data obtained from samples with neat MABr (PeOA0, $MAPbBr_3$) and OABr (PeOA100, $(OA)_2PbBr_4$) are shown for comparison. The time by which the PL intensity dropped to its $1/e$ intensity is denoted by a dash line. b) The decay lifetimes ($\tau_{1/e}$) for samples with varied OABr content. Images adapted from Ref. [156].

	PeOA10	PeOA20	PeOA40
PL lifetime $\tau_{1/e}$ (ns)	41.2	36.7	6.3
PLQY (%)	0.41	0.96	1.62

Table 6.1: PL lifetime $\tau_{1/e}$ (ns) and PL quantum yields (PLQY) of mixed dimensional perovskite films with varying OABr content.

6.2 Morphological evolution in mixed dimensional perovskite films

The morphology development in the mixed dimensional perovskite films on different compositions are determined in terms of the evolution of both crystal structure (Section 6.2.1) and domain structure (the surface structure is illustrated in Section 6.2.2, and the inner morphology is discussed in Section 6.2.3).

6.2.1 Crystal structure

The atomic and molecular structures of the perovskite films were analyzed with x-ray diffraction (XRD) and with grazing incidence wide angle/small angle x-ray scattering (GIWAXS/GISAXS). Benefits from the combination of both conventional and modern

scattering techniques, a full picture including the crystalline phase as well as crystal preferential orientation is obtained.

XRD

The crystal structures of the mixed dimensional perovskite thin films are first studied with XRD. Figure 6.4 shows the XRD patterns of samples with varying OABr content. In addition, the diffraction patterns of the OABr and $PbBr_2$ precursors are also presented for comparison. The XRD pattern of sample without OABr cation (PeOA0) exhibits peaks at 1.05, 1.49, 2.10, 2.35, 2.57, 2.97 and 3.15 $Å^{-1}$, which can be respectively assigned to the (001), (101), (002), (102), (112), (202) and (003) crystal plane. The obtained lattice parameter of 5.9 Å demonstrates a stable cubic *Pm3m* phase. [187] In sample PeOA100 that uses neat OABr, the XRD pattern confirms the formation of 2D layered perovskite platelets (i.e., $(OA)_2PbBr_4$). [59,179] For samples containing mixtures of OABr and MABr, the XRD patterns display distinct reflection peaks at bigger q values ($q > 1$ $Å^{-1}$) which originate from the single cubic phase of $MAPbBr_3$. While at smaller q range ($q < 1$ $Å^{-1}$), additional features pops up alongside increasing the OABr content, which due to either the formation of perovskite platelets with several nanometer thickness, or the unreacted precursor residues. Since most reflections above 1 $Å^{-1}$ originate from (00l) family, a high degree of crystal orientation is suggested. Notably, for samples containing an OABr mole ratio up to 20%, no identifiable reflections from $(OA)_2PbBr_4$ are revealed in the XRD patterns. With further increasing the OABr content, the XRD pattern displays a mixed crystal families of both $(OA)_2PbBr_4$ and $MAPbBr_3$. This obtained result approves our previous hypothesis that the 2D perovskite plateletes first adsorb on the surface of the 3D crystals at low OABr mole ratio up to 20% whereas with further increasing the OABr mole ratio, in addition to the 2D platelets, layered perovskite crystals are formed.

In Figure 6.5, the crystal size calculated by using the Scherrer equation slightly decreases with increasing the OABr content. Therefore, it suggests that the OABr behaves as a capping ligand, which confines the crystal growth of 3D perovskite.

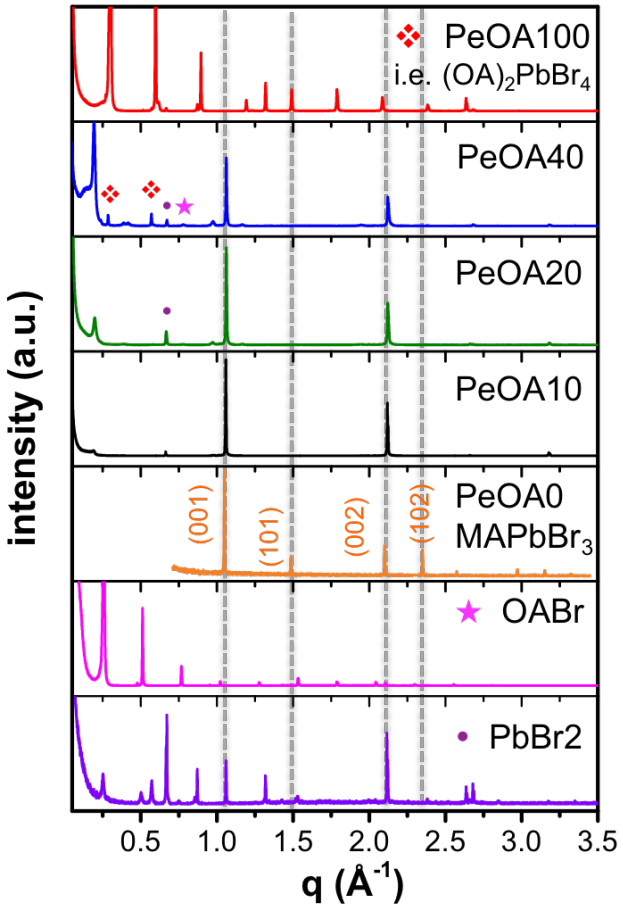

Figure 6.4: XRD patterns of perovksite films with varying OABr content. XRD patterns of OABr and $PbBr_2$ are showed for comparasion. The grey lines highlight the reflection planes originated from 3D $MAPbBr_3$ perovskite crystal. Reproduced from Ref. [156] with permission from the John Wiley & Sons, Inc.

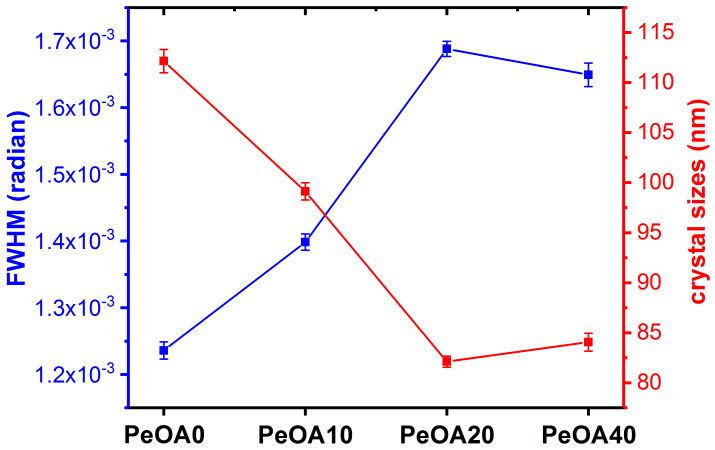

Figure 6.5: Development of crystal size in the perovskite thin films with varying OABr content. The individual FWHM is obtained by fitting the (001) reflection peak using Gaussian peak function.

GIWAXS

To further study the crystalline quality of the mixed dimensional perovskite films, GIWAXS and GISAXS were employed to investigate the 3D and 2D perovskite crystals, respectively. Figure 6.6 shows the 2D GIWAXS data for perovskite films derived from five different OABr contents, in which q_z is the component of the scattering vector perpendicular to the sample surface whereas $q_r = ({q_x}^2 + {q_y}^2)^{1/2}$ is the component of the scattering vector in parallel the substrate of the total momentum transfer q. The wedge of inaccessible data in GIWAXS patterns occurs due to the reciprocal space conversion of raw detector images. Stark differences are revealed in the 2D GIWAXS patterns alongside increasing the mole ratio of OABr.

A Debye Scherrer intensity ring with tinny sharp spots, at around q = 1 $Å^{-1}$ can be observed in the sample PeOA0 without loading any OABr cation (Figure 6.6a). In comparison to our previous XRD result, this intensity ring can be identified as the (001) reflection plane of the 3D $MAPbBr_3$ crystal with no preferential crystal orientation with respect to the substrate. In addition, the minor intensity features in reciprocal space give a strong indication of the existence of large size crystals inside the sample. Along the substitution of MABr with OABr, considerable differences are revealed in the 2D GIWAXS diffraction patterns. First, upon loading the OABr cation up to a value of 40% (Figure 6.6d), the reflection rings of 3D $MAPbBr_3$ crystal vanish in azimuthal intensity and remarkably sharp, discrete Bragg peaks arise, indicating that the 3D bulk $MAPbBr_3$ crystals in all the three mixed cations samples have strong preferential crystal orientation with respect to the substrate. This result implies that charge carriers are expected to enjoy more efficient diffusion among the 3D crystals in comparison to a random crystal orientation, since a lower number of defects are expected to form at the grain boundaries. [188] In addition, the diffraction peak intensity at q < 1 $Å^{-1}$ gradually grows with increasing the OABr content, as is corroborated by the XRD data. This phenomenon will be further discussed in the following GISAXS section. Furthermore, for the sample prepared using neat OABr (PeOA100), the 2D GIWAXS pattern is dominated by scattering features of the 2D layered perovskite. In order to further quantify the 3D crystal orientation in the mixed dimensional samples, intensity-integration along the (001) reflection peaks with respect to the azimuthal angle (χ) are performed for samples PeOA0, PeOA10, PeOA20, and PeOA40.

Figure 6.7 displays the integration results. In the case of sample containing neat 3D $MAPbBr_3$ crystals (PeOA0), higher scattering intensities are observed at $\chi \approx$ -45°, illustrating that the 3D crystals distribute in an edge-up orientation with (101) planes parallel to the substrate. In addition, from the 2D GIWAXS pattern shown in Figure 6.6 a), a side intensity maximum can also been observed for the (101) reflection plane at $\chi \approx \pm 45°$,

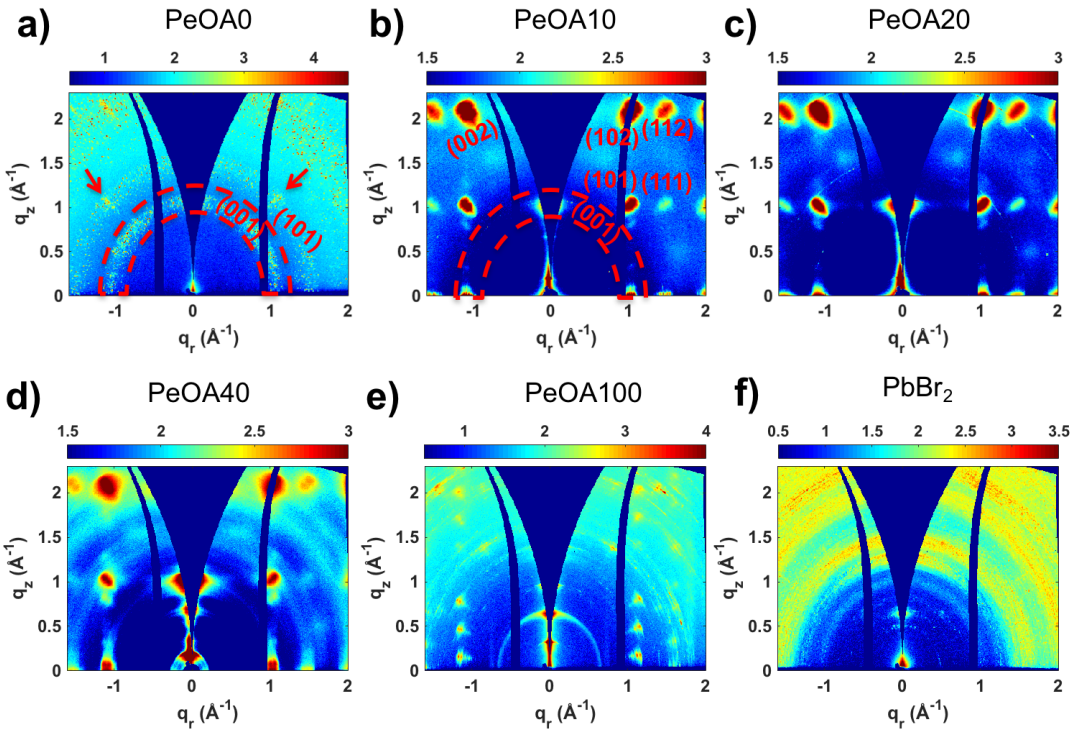

Figure 6.6: 2D GIWAXS data for the resulting perovskite films with an OABr mole ratio of: a) 0% (PeOA0), b) 10% (PeOA10), c) 20% (PeOA20), d) 40% (PeOA40), and e) 100%(PeOA100). The 2D GIWAXS data for pure $PbBr_2$ is showed in f) for comparison. Reproduced from Ref. [156] with permission from the John Wiley & Sons, Inc.

which indicates that the 3D crystals are also partially orientated with their (001) planes parallel to the substrate surface, i.e., face-up orientation. However, due to the experimental set-up, the corresponding intensity signals of (101) for the edge-up orientation as well as (001) for the face-up orientation are not approachable due to the inaccessible data in the missing wedge. With substitution of MABr with OABr, we can first observe a nearly isotropic face-up orientation in sample PeOA10 and the intensity of (001) peak gradually grows along the azimuthal angle (χ) with increasing the OABr mole ratio. This result implies a minor fraction of 3D crystal reoriented (Figure 6.7b). Therefore, one can speculate that the long organic cation OABr contributes strongly to the crystal conversion process.

GISAXS

In Figure 6.8, the GISAXS data of the mixed dimensional perovskite films displays sharp Bragg peaks at q_z = 0.19, 0.23, and 0.39 $Å^{-1}$, which correspond to a lattice d-spacing

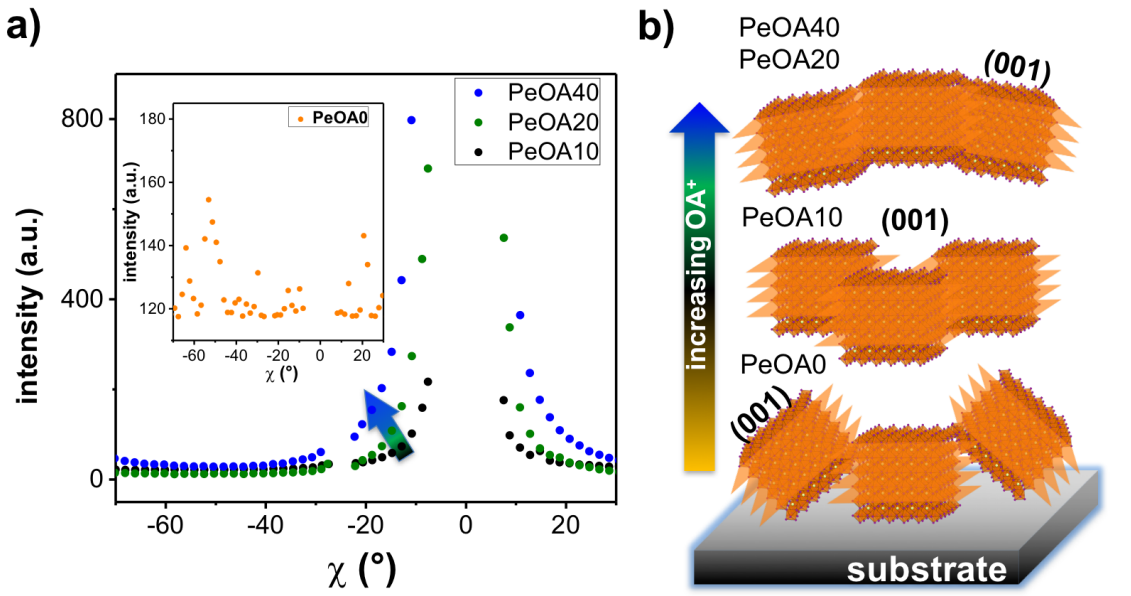

Figure 6.7: a) Azimuthal integrations of (001) reflection peaks of the (001) reflection plane at q = 1.06 $Å^{-1}$. b) Schematic illustration of varing crystal orientation in perovskite films with different compositions.

of 33.1, 27.3, and 16.1 Å, respectively. These spcaings can be attributed to 2D platelets with perovskite unit cell thickness (n) of 3, 2 and 0 (i.e. single layer of lead bromide), respectively. [15, 16] At $q_z > 0.5$ $Å^{-1}$, the scattering patterns are dominated by three intensive peaks at $q_z = 0.59$, 0.67, and 0.72 $Å^{-1}$. As compared to the GISAXS data of the neat OABr sample (PeOA100) (Figure 6.8d) and pure $PbBr_2$ precursor (Figure 6.8e), the Bragg peaks at $q_z = 0.59$ $Å^{-1}$ and $q_z = 0.67$ $Å^{-1}$ can be respectively identified as $(OA)_2PbBr_4$ and $PbBr_2$. On the basis of the XRD data that were discussed in the previous section, the peak at $q_z = 0.72$ $Å^{-1}$ can be assigned as the (003) reflection plane of the crystallized OABr. [179] In Figure 6.8a, the absence of Bragg peaks along q_r direction in sample PeOA10 indicates that the 2D platelets as well as the residue precursors are highly orientated in parallel to the substrate surface, which is identical to 3D bulk $MAPbBr_3$ crystals. However, for samples containing higher OABr mole ratio (Figure 6.8b,c), additional varied scattering intensity emerged depending on the azimuthal angle for the reflection peaks of 2D platelets (n = 3, 2) and OABr. In contrast, the orientation of 2D platelets with single lead layer (n = 0) and $(OA)_2PbBr_4$ shows no variation on composition. We speculate this results from the interface effect. The applied substrates for film deposition were pre-acid cleaned and thus producing a hydrophilic surface. As a consequence, the polar NH_3^+ group were first deposited at the interface between the substrate and film, leading an enrichment layer of thinner platelets distributed at the bottom part

inside the films. This is consistent with PL emission spectra measured with front and back excitations in Figure 6.2. The GISAXS 2D data is further investigated by azimuthal integration around q = 0.72, 0.67 and 0.19 $Å^{-1}$, corresponding to the respective diffraction rings of OABr, $PbBr_2$ and 2D perovskite platelets (n = 3). These Bragg peaks are chosen because they exhibit strong intensity and not obscured by higher order reflections at the large q range.

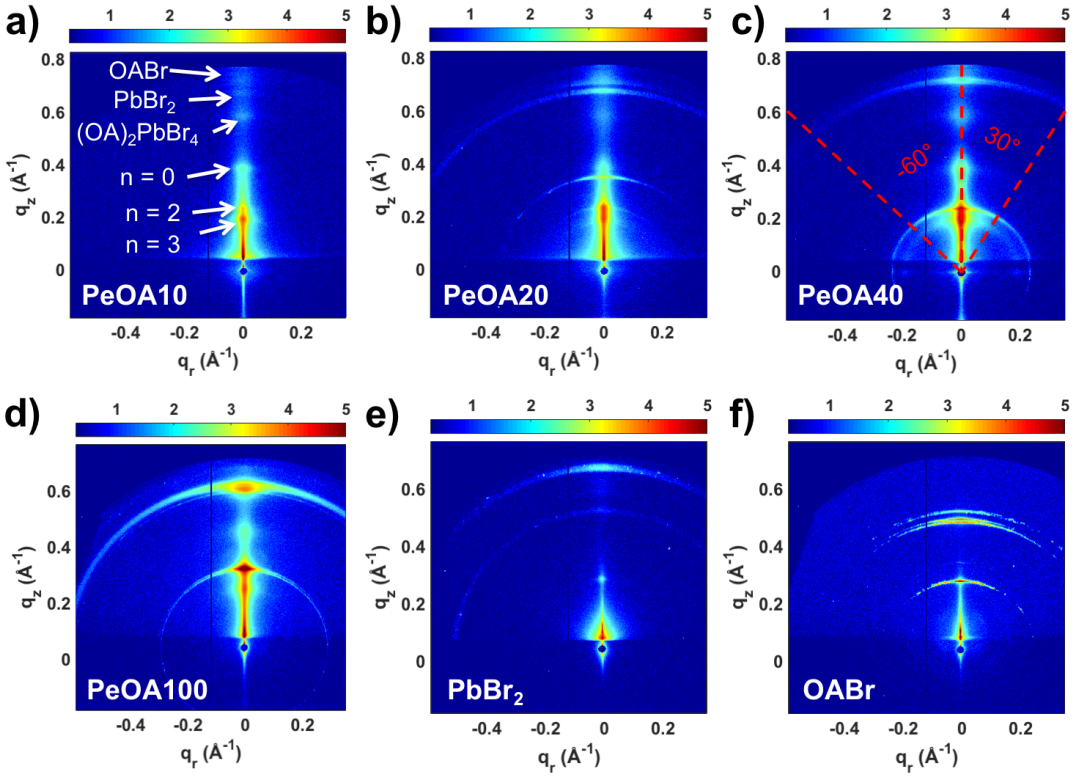

Figure 6.8: 2D GISAXS data for the resulting perovskite films with an OABr mole ratio of: a) 10% (PeOA10), b) 20% (PeOA20), c) 40% (PeOA40), and d) 100% (PeOA100). The scattering patterns of applied precursors are shown in e) $PbBr_2$ and f) OABr. Reproduced from Ref. [156] with permission from the John Wiley & Sons, Inc.

In Figure 6.9, the azimuthal integration results show that the OABr crystal in the sample PeOA10 highly orients in parallel to the substrate. In addition, this is likely to suppress the crystal buildup along surface normal and allow perovskite crystal to grow more efficiently along the in-plane direction, leading the formation of a full surface coverage with larger grain sizes. On the other hand, upon further increasing the OABr mole ratio up to 40%, additional strong preferential orientation at $\chi \approx \pm 10°$ starts to appear, indicating that a partial reorientation of OABr crystals. Similarly, additional shoulder-like intensities at around $\chi \approx \pm 20°$ appear for the 2D perovskite platelets (n = 3). However,

there is no relationship on crystal orientation between 2D perovskite platelets and $PbBr_2$ (Figure 6.9c). Provided that the longer organic chain of OABr can only fit either in the periphery of the corner-sharing $[PbBr_6]^{4-}$ octahedral or adsorb at the perovskite crystal surface, we speculate that during crystal conversion an isotropically orientated OABr sheet will provide more channels for precursor intercalation, as a consequence the crystal orientation condition becomes diverse.

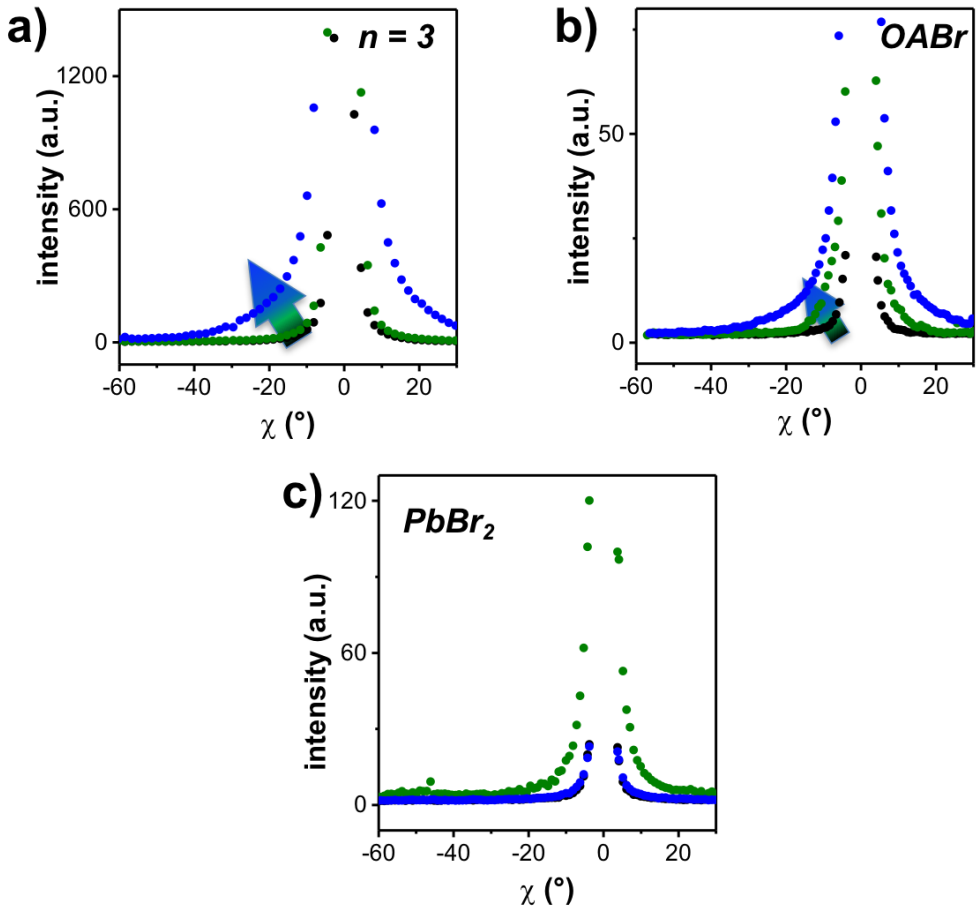

Figure 6.9: Azimuthal integrations of peaks: a) at q = 0.77 Å^{-1} for OABr, b) 0.67 Å^{-1} for $PbBr_2$and c) at q = 0.19 Å^{-1} for 2D platelets with three unit cells thickness (n = 3). Reproduced from Ref. [156] with permission from the John Wiley & Sons, Inc.

6.2.2 Surface structure

The surface morphology of the mixed dimensional perovskite films are characterized by means of scanning electron microscopy (SEM) and atomic force microscopy (AFM).

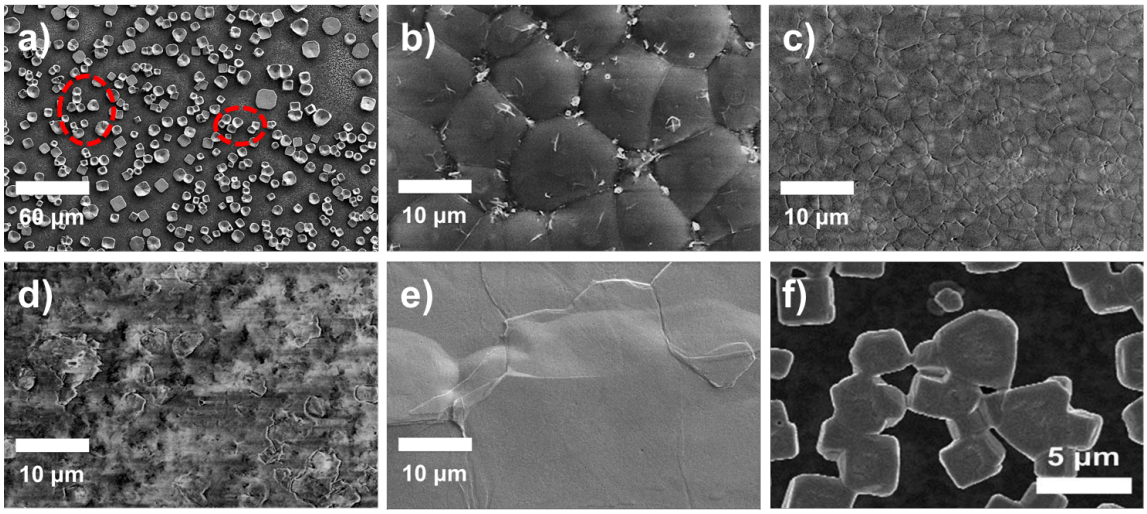

Figure 6.10: SEM top-view images of the resulting mixed dimensional perovskite films with varying OABr mole ratio a) 0% (PeOA0, $MAPbBr_3$), b) 10% (PeOA10), c) 20% (PeOA20), d) 40% (PeOA40), e) 100% (PeOA100, $(OA)_2PbBr_4$). f) SEM image of perovskite film prepared from neat MABr, image adapted from [189].

As shown in Figure 6.10, distinct differences on surface morphology alongside increasing OABr mole ratio are revealed. In Figure 6.10a, sample containing 100% MABr exhibits isolated $MAPbBr_3$ crystals on submicrometer scale. This result corroborates the previous report (Figure 6.10f) that it is relatively difficult to use one-step solution-processed spin coating technique to achieve continuously $MAPbBr_3$ films from neat DMF solution. [189, 190] Although it is elucidated that big domains are formed in this sample by the aggregation of smaller cuboid crystals, the discontinuously morphology is prospected to generate a poor in-plane path for charge carriers transportation. In the sample PeOA10, uniform domains on tens micrometer scale are formed by substituting 10% of MABr with OABr whereas no clear gaps can be observed on the surface. Upon further increasing the OABr content up to 40%, these micrometer domains shrink in size and the surface uniformity decreases. For sample with a OABr mole ratio of 40% (Figure 6.10d), gaps emerge on the surface and stacked-layer structures are likely formed, which suggests the existence of 2D perovskite in the sample. In Figure 6.10e, the sample surface becomes very smooth and featureless at the applied probing length. On the basis of the GISAXS results (Figure 6.8), the appearance of the upper surface OABr likely retards the crystal growth along the surface normal, additionally, continuously large grains grow along the in-plane direction in sample with lower mole ratio of OABr. However, the orientation of OABr diversified in film volume at higher OABr content (Figure 6.9b) and therefore leads to the decrease of crystal size (Figure 6.5). For sample with the highest OABr content

(PeOA40), the low dimensional perovskite platelets flake off easily due to low binding force.

Another interesting observation has been noticed is the degradation of perovskite crystal under electron beam. Figure 6.11 displays the perovskite crystal structure exposed for different times under the electron beam. After long exposure time, gaps appear on perovskite crystals and expand even broader. This result is comparable with the previous report which highlighted the difficulties of using SEM to acquire perovskite morphology information on nanometer scale. [93] Therefore, AFM is employed as a complementary solution to study the surface structure of perovskite films.

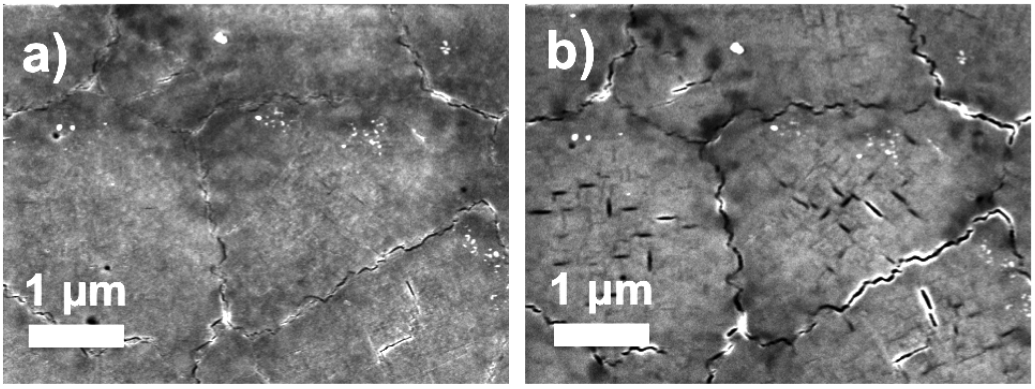

Figure 6.11: Electron beam degradation effect on the perovskite crystal. a) PeOA20, b) PeOA20 after 2 min electron beam irradiation.

In Figure 6.12a, layered structures are clearly seen in sample with the lowest OABr content (PeOA10). More specifically, a bright quadrate-like platelet with thickness of ≈ 3 nm appeared at the top left corner (Figure 6.12d). Compared to the previous report, structure with thickness of 3 nm can be assigned to the 2D perovskite platelets with 2-3 perovskite unit cells, which is in good accordance to the GISAXS results (Figure 6.8). [15, 16] By further increasing the OABr concentration, the platelets structure increases in content and aggregates formed by platelets stacking are clearly illustrated in sample PeOA40. Additionally, the layered structure becomes thicker at higher OABr content (Figure 6.12f).

6.2.3 Inner film morpology

In order to have a statistical understanding about the inner film morphology on both mesoscale and nanoscale, samples are probed by grazing incidence small angle neutron scattering (GISANS) and GISAXS, respectively. Grazing incidence small angle scattering using X-ray or neutron as probe has been proved to be a unique technique to characterize

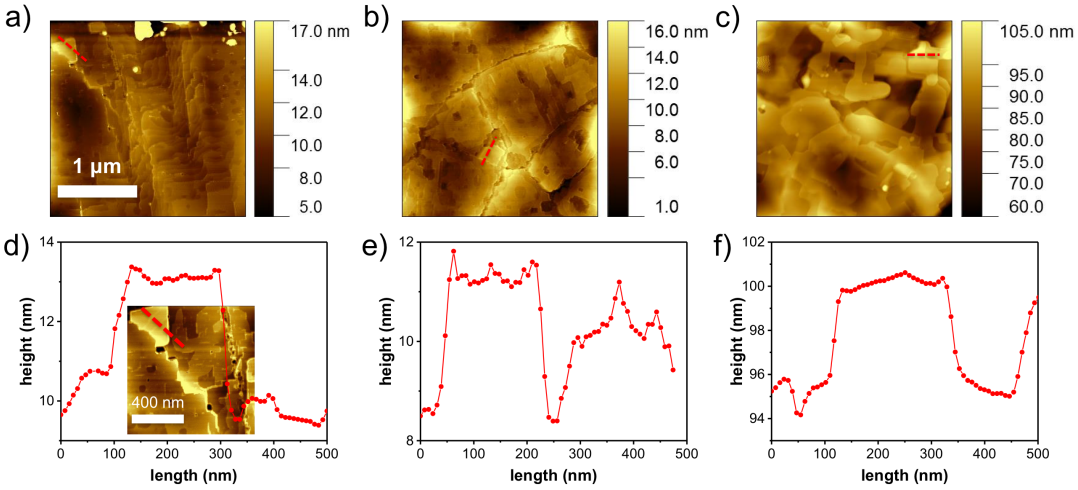

Figure 6.12: AFM topography images (scale bar 1 μm) (a-c) and line profiles (d-f) of the mixed dimensional perovskite films with varying % OABr content:a,d) 10% (PeOA10), b,e) 20% (PeOA20), and c,f) 40% (PeOA40). The corresponding extracted positions are marked with red lines in AFM images. Localed structure of sample PeOA10 with larger magnification (scale bar 400 nm) is shown in d) as inset. Reproduced from Ref. [156] with permission from the John Wiley & Sons, Inc.

polymer thin films, and more recently its versatility has also been applied to organometal halide perovskite thin films. [133, 191–194] The obtained scattering data are analyzed in two steps: (1) quantitative scattering object behavior analysis using scattering power-law; (2) lateral domain structures revealed by fitting the scattering signal along the Yoneda peak position within the distorted wave Born approximation (DWBA).

An incidence angle of 0.7°, which is above the critical angle of the investigated material, is applied for all GISANS measurements to guarantee a completely penetration over the probed sample volume. As shown in Figure 6.13a, the scattering pattern at $q_z \geq 0$ nm^{-1} is dominated by two prominent scattering features. The material-sensitve Yoneda peak that emerges at the critical angle of the investigated material is located at small q_z values whereas the specular peak is at higher q_z values due to the incident angle selection. In addition, a wing-like scattering feature at around the Yoneda peak position along the q_y direction is captured on the 2D detector, which arises from the domain structure inside the investigated films. In order to understand the development of differently sized mesoscale crystals, line cuts are performed along the wing-like scattering signals for all the three samples(6.13b). In the first step, the scattering profiles of all three samples in the middle q range (0.01-0.05 nm^{-1}) exhibit the behavior of power law scattering ($I(q) \propto q_y^{-\alpha}$), reflecting the characteristic of a mass fractal ($2 < \alpha < 3$) behavior over hundred

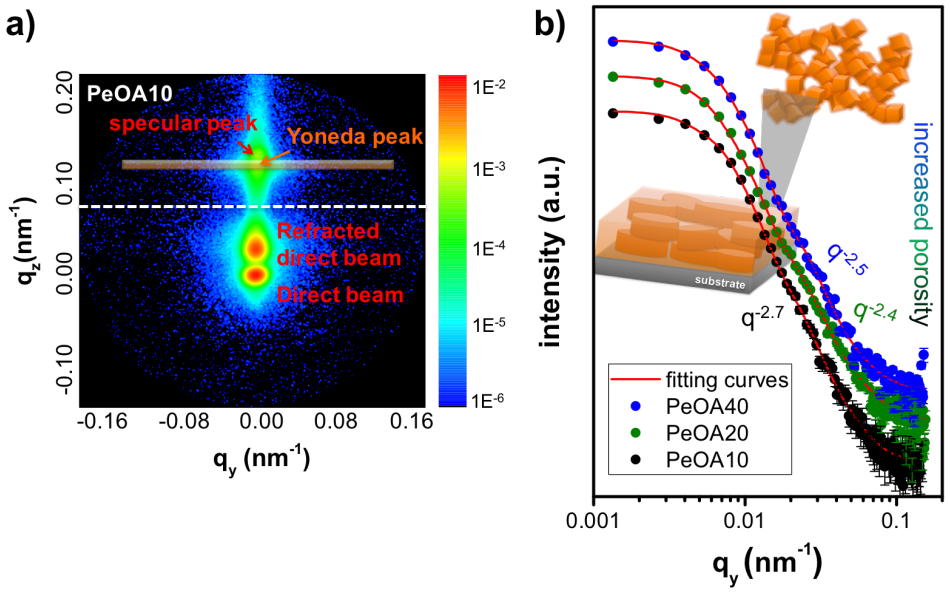

Figure 6.13: a) 2D GISANS pattern of sample containing an OABr mole ratio of 10% (PeOA10). Color coding labels the representative scattering features on the 2D detector. The position of sample horizon is indicated by a white dashed line. Due to the transparency of silicon substrate to neutrons, both direct beam and refracted direct beam are seen below the horizon. b) Horizontal line cuts of the GISANS data (symbols) and the corresponding fits (solid lines) of three mixed-dimensional perovskite films. The curves are shifted in log scale for a better comparison. A representative mass fractal morphology of mesoscale perovskite domain structure is depicted in inset. Images adapted from Ref. [156].

nanometer length scale. [150, 194, 195] The mass fractal depicts a self-similar packing of domains as schematically illustrated in the inset of Figure 6.13b. [196] Compared to previous report that the fractal morphology in $MAPbI_3$ films were explained by the fractal-like diffusion of MAI into PbI_2 films, [194] we estimate in the presented samples, the mass fractal morphology is formed by the grains aggregation alongside the presence of voids in the films. Moreoever, the value of the exponent gives the indication of the compactness of the perovskite domain arrangement, with a smaller value of α referring to a less dense film. [197, 198] As shown in Figure 6.13b, a lower exponent value is determined at higher OABr content, which represents the formation of a less dense film. This result is in good agreement with the AFM topography result while in a more quantitative view. Secondly, the obtained curves are modeled with three independent 1D cylinder-like paracrystals in the framework of the DWBA using the local monodisperse approximation (LMA) to reveal the morphological parameters in terms of domain sizes and pore sizes. Compared

with the surface structure reveled by SEM measurements (Figure 6.10), the cylinder-like paracrystals are expected to establish a good reproduction of the scattering signal.

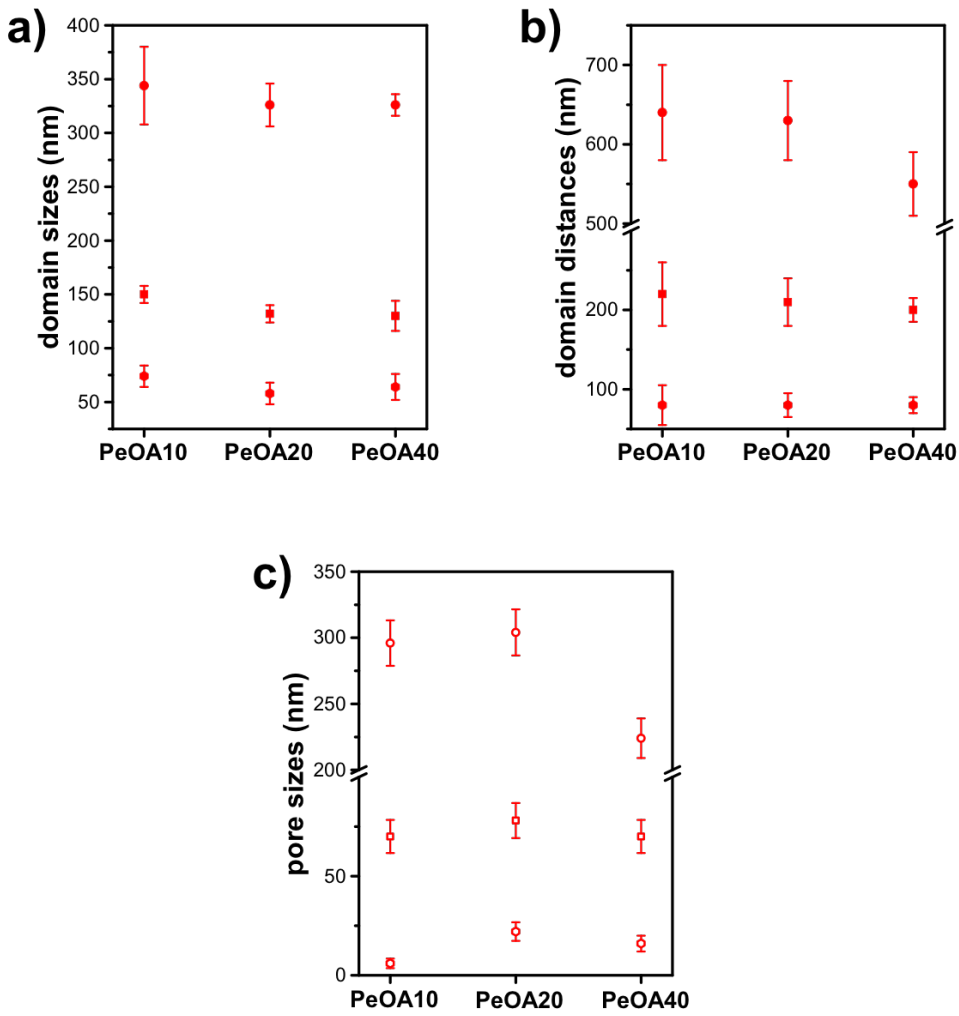

Figure 6.14: Morphological parameters extracted through model fitting of GISANS data: a) form factors that represent the domain sizes, b) structure factors that represent the domain center to center distances, c) pore sizes calculated by deducting domain distances with the corresponding domain sizes. Images adapted from Ref. [156].

From this analysis, three substructures describing rather large domains that bigger than 300 nm, medium size domains which around 150 nm and small domains that below 80 nm, along with the corresponding center-to-center distances of around 600 nm, 200 nm and 100 nm are extracted (Figure 6.14). In Figure 6.14a, the domain sizes seem to first slightly shrink with increasing OABr content from 10% to 20% and grow in sizes upon further increasing OABr content up to 40%. Based on the previous SEM (Figure 6.10)

and AFM (Figure 6.12) studies, this inconsistent result can be identified as the long organic cation OABr first terminates the domain growth in lateral direction from sample PeOA10 to PeOA20 whereas in sample PeOA40, a larger population of 2D perovskite platelets arises associated with bigger aggregations formed by stacking of 2D platelets. This hypothesis is further supported as both domain distances and pore sizes decreased from sample PeOA20 to sample PeOA40. However, due to an upper resolution limit for the employed GISANS setup, domain structures smaller than 50 nm are not accessible. Since the cation substitution is also prospected to influence on domain structure on the scale range of tens nanometer, GISAXS is employed as a complementary method to reveal the nanoscale domains inside the films.

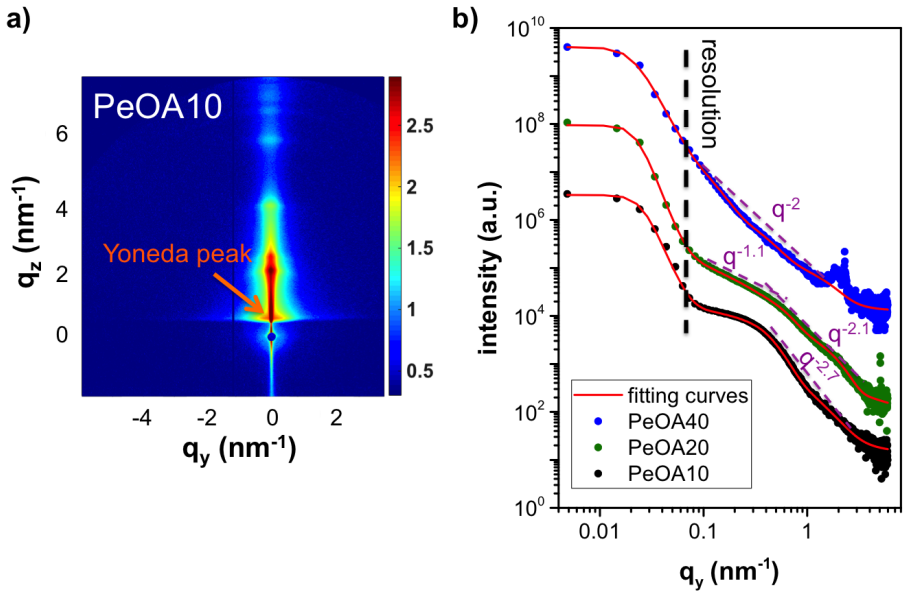

Figure 6.15: a) 2D GISAXS pattern of sample containing an OABr mole ratio of 10% (PeOA10), b) Horizontal line cuts of the mixed dimensional perovskite thin films. The power law scattering behaviors at individual q_y range are marked along the corresponding curves. Images adapted from Ref. [156].

In Figure 6.15a, a representative 2D scattering images of the film with an OABr content of 10% is shown. The sample sensitive Yoneda peak position is highlighted by an arrow. In order to extract the nanoscale domain information within the investigated films, three horizontal line cuts are taken at the corresponding Yoneda peak positions of the 2D GISAXS data for all the three samples. As shown in Figure 6.15b, the obtained scattering signals extend the q_y value down to 4 nm^{-1}, covering a structure length scale approaching to 1 nm. At $q_y \approx 0.3$ nm^{-1}, a prominent shoulder-like intensity distribution

in sample PeOA10 is visible, originating from the correlated domain structures span a range of 5-25 nm. Upon loading more OABr content, the shoulder becomes broader in sample PeOA20 and vanishes in sample PeOA40. In sample PeOA10, the scattering curve contributes a mass fractal with dimension $\alpha \approx 2.7$ at $0.3 < q_y < 2$ whereas at low q_y values ($q_y < 0.3$), the scattering curve exhibits a flat Guinier scattering behavior. Alongside the increasing of OABr mole ratio to 20 %, the scattering curve at high q ($q_y > 0.3$) delivers a q^{-2} thin platelet-like power law scattering and at low q, these platelets tend to form rod-like aggregates which is described by q^{-1}. For sample with the highest OABr concentration (PeOA40), the scattering curve displays an uniform q^{-2} power law scattering which corresponds to a platelet-like structure over the probed structure sizes from 2 to 22 nm. In addition, the morphological ordering in the sample is reflected in the shape of its scattering curve. [152] That is, a system with higher degree of order exhibits a more prominent scattering feature. [131] Therefore, the morphological uniformity decreases in sample PeOA40 in comparison to sample PeOA10.

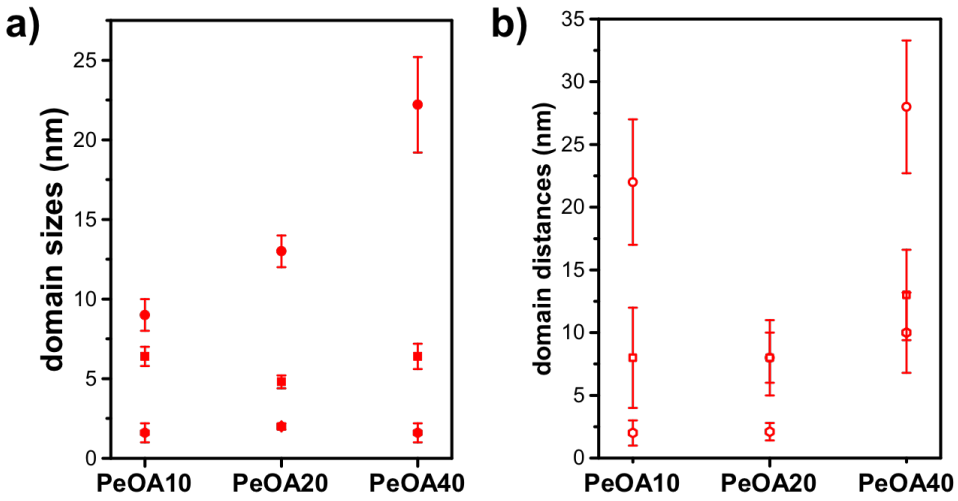

Figure 6.16: Morphological parameters extracted through model fitting of GISAXS data: a) form factors that represent the domain sizes, b) structure factors that represent the domain center to center distances. Images adapted from Ref. [156].

In order to extract the lateral domain structures from the horizontal line cuts, an analogous model using three cylinder-like paracrystals as applied in the GISANS analysis was also applied to fit the GISAXS data. The obtained model curves are plotted as red lines, together with the horizontal line cuts in Figure 6.15b. This fitting model describes the scattering signals as the superposition of scattering from individual cylinder centers with three different sizes. Figure 6.16 shows the extracted morphological parameters. The scat-

tering contrast is originated from the electron density difference between the perovskite crystals and the crystallized organic OABr ligand, herein the obtained domain information is identified as the 2D perovskite platelets. From this analysis, it is demonstrated that the sub structure size describing the rather large domains steadily grows from 8 nm to 22 nm upon increasing OABr content. This result is supported by the GIWAXS results that the OABr ligands are predominantly distribute along the surface normal direction. As a consequence, the 2D perovskite crystallites are prospected to grow along the lateral direction. The other two small sub structures are not considered in the present analysis, because the structure sizes are already close to the thickness of 2D platelets.

6.2.4 Results

The effect of OABr content in tailoring the morphology of mixed dimensional perovskite films is thoroughly studied by a combination of imaging microscopy (SEM & AFM) and advanced scattering techniques (GISANS, GIWAXS, GISAXS). A schematic description of morphological evolution in mixed dimensional perovskite films is shown in Figure 6.17. Alongside increasing OABr, the growth of 3D bulk-like crystals is restricted, whereas an increased content of 2D platelets-like crystals are identifiable from optical spectroscopy (Figure 6.1) and GISAXS (Figure 6.8). Moreover, the 2D platelets locate close to the bottom substrate in sample PeOA10, while they tend to distribute all along the film volume at higher OABr content (Figure 6.2). The micrometer scale domain on the film surface in sample PeOA10 shrinks in size with formations of large pinholes in sample PeOA40 (Figure 6.10 and Figure 6.12). It is revealed by GIWAXS (Figure 6.7) and GISAXS (Figure 6.9) that OABr has a function of directionally control the perovsktie crystal growth. Both, the ordering degree of domain and crystal orientation diminish upon increasing OABr content.

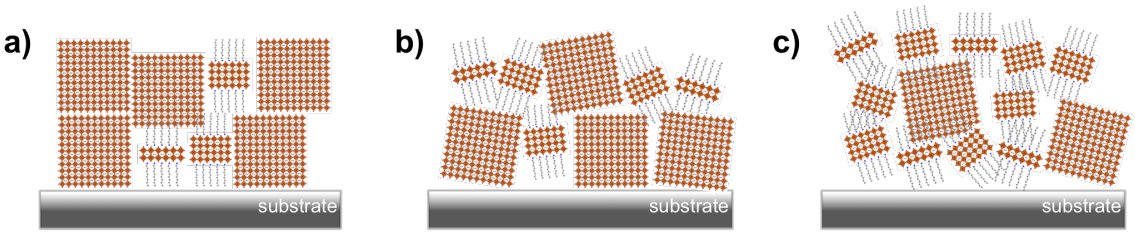

Figure 6.17: Schematic illustration of the resulting morphology in a) PeOA10, b) PeOA20 and c) PeOA40. Reproduced from Ref. [156] with permission from the John Wiley & Sons, Inc.

6.3 Amplified spontaneous emission in mixed dimensional perovskite films

To investigate the morphological impact on the quality of optical properties, the prepared samples are studied by amplified spontaneous emission (ASE) in collaboration with Prof. Jochen Feldmann (Lehrstuhl für Photonik und Optoelektronik, LMU). ASE measurements were performed by Aurora Manzi in the Feldmann group.

6.3.1 The arise of ASE

As shown in Figure 6.18a, sample PeOA10 at pump fluence below 15 µJ/cm^2 exhibits a standard fluorescence spectra with a single spontaneous emission (SE) peak centered at 530 nm. Above this value, a second peak at 548 nm with narrower FWHM arises and rapidly gains in intensity as compared to the original peak (Figure 6.18d). This peak is given by the emergence of amplified spontaneous emission (ASE). In order to extract the emergence threshold, the areas of the SE and ASE peaks are respectively integrated in Figure 6.19a. A clear kink is revealed in the total area of SE and ASE peaks, which gives a ASE threshold of 17.8 µJ/cm^2 for sample PeOA10. PeOA20 and PeOA40 were analyzed with the same method to compare the individual trends and results are shown in Figure 6.19b and Figure 6.19c, respectively. A similar trend is revealed in sample PeOA20 whereas the ASE threshold slightly shifts to a larger value of 20.5 µJ/cm^2. For sample PeOA40 which contains a even higher OABr content of 40%, no ASE can be observed which means the ASE behavior in the mixed dimensional perovskite samples vanishes upon increasing OABr content.

6.3.2 Effect of energy transfer and morphological changes on the evolution of ASE quality

As previous discussed in section 6.2.4, the homogeneity of perovskite domain structure as well as the identical crystal orientation diminished alongside increasing OABr content. The ASE behavior in the mixed-dimensional perovskite films seems to be correlated with the content of the organic ligand. However, due to the mixed-dimensionality of perovskite crystals, it is necessary to examine additional factors that could impact in this process, such as energy transfer between domains and carriers confinement in 2D perovskite platelets.

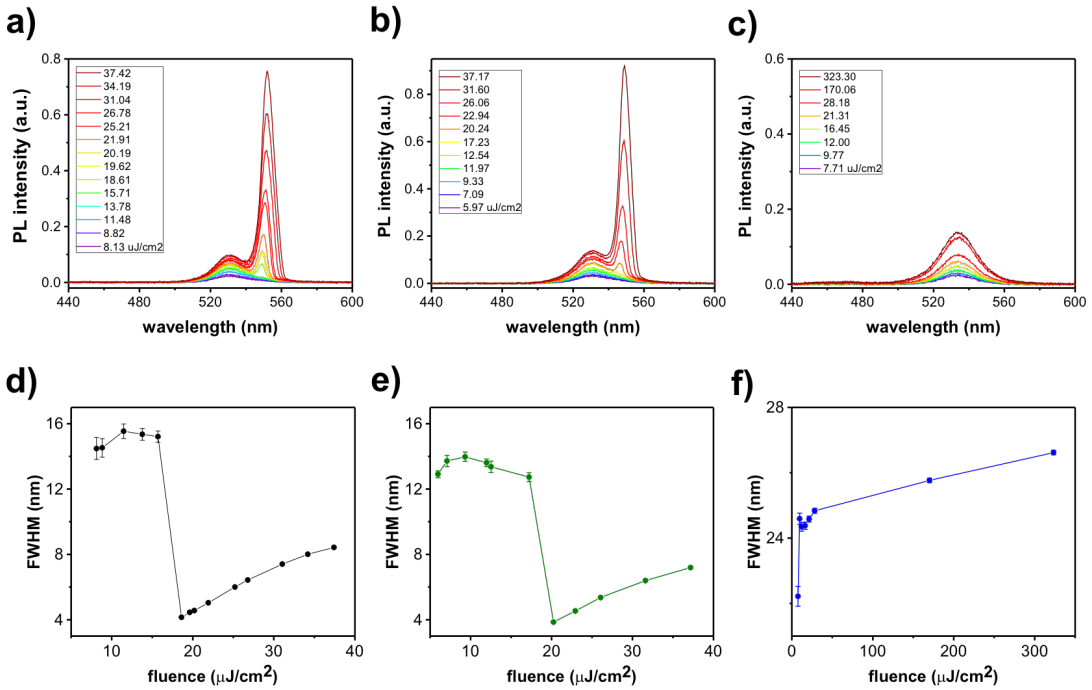

Figure 6.18: Power-dependent emission spectra of a) PeOA10, b) PeOA20 and c) PeOA40. Changes of FWHM in ASE peaks as a function of the excitation fluence of d) PeOA10, e) PeOA20 and f) PeOA40. Reproduced from Ref. [156] with permission from the John Wiley & Sons, Inc.

The PL-excitation (PLE) spectra (Figure 6.20) of the mixed dimensional perovskite films detected at 560 nm are contributed by both 2D perovskite platelets and 3D bulk perovskite crystals. The high PLE contributions of 2D platelets in sample PeOA10 and sample PeOA20 demonstrate the existence of energy transfer from 2D platelets to 3D bulk perovskite crystals. The PLE of thin 2D platelets (n = 1, 3) vanish upon increasing the OABr content. In sample PeOA40, the spectrum is dominated by features that originated from thicker platelets and bulk-like crystals. This marked difference evidences that the energy transfer from thin 2D platelets to 3D perovskite crystals is more efficient in sample containing lower OABr content, which probably due to the higher proximity of the crystals (Figure 6.17).

The exciton binding energy is considerably increased in 2D perovsktie platelets in comparison with 3D bulk-like crystal. (${E_B}^{2D} = 4{E_B}^{3D}$). [199] Upon increasing OABr content, the system is transforming from a 3D bulk-like perovskite in to a mixture of 3D/2D multi-dimensional perovskite system. Therefore, a quantification of mixed morphologies is necessary.

The GIWAXS data shown in Figure 6.6 is detailed studied. As shown in Figure 6.21d, the 2D platelets at $q_z = 0.19$ Å^{-1}, 0.23 Å^{-1} are clearly visible below the missing wedge.

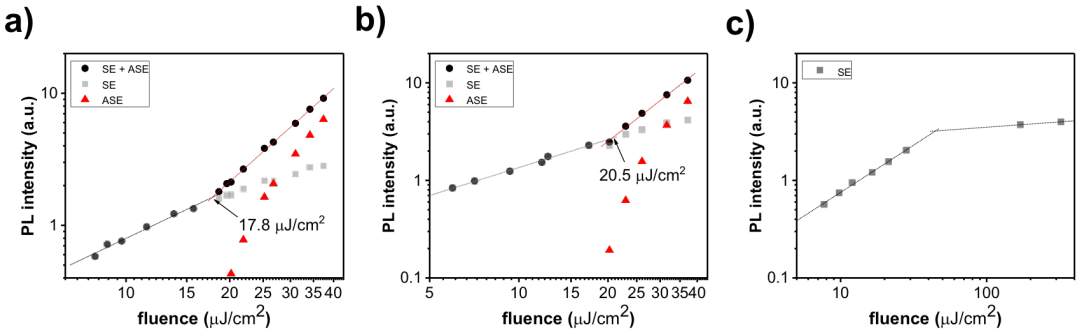

Figure 6.19: The integrated PL intensity as a function of the excitation fluence of a) PeOA10, b) PeOA20 and c) PeOA40. Images adapted from Ref. [156].

Additionally, the 2D platelets are highly oriented in samples containing lower OABr content (Figure 6.21a,b), whereas in sample PeOA40 (Figure 6.21c) additional intensities at an increasing range of azimuthal angles are observed. This result is consistent with the findings from the 2D GISAXS data (Figure 6.8), which implies that the 2D platelets orientation diversify at higher OABr content. Both 3D bulk perovskite crystals and quasi-2D perovskite platelets contribute intensity at $q > 1$ Å^{-1}. Therefore, by integrating over the 2D reflection peaks (Figure 6.21a-c) and the (101) reflection peak (Figure 6.6b-d) of the individual GIWAXS pattern, one can determine the amount of 2D perovskite platelets in the specific sample. The total amount of crystals is relatively constant at different compositions (Figure 6.21e), whereas the amount of 2D platelets increased by a factor of 2 in sample PeOA40 compared to sample PeOA10 (Figure 6.21f). Accordingly, excitons are more easily confined in samples with large OABr content. In addition, photons are expected to interact with less crystals in sample PeOA40 due to the low degree of morphological order and the large amount of pinholes (Figure 6.17c).

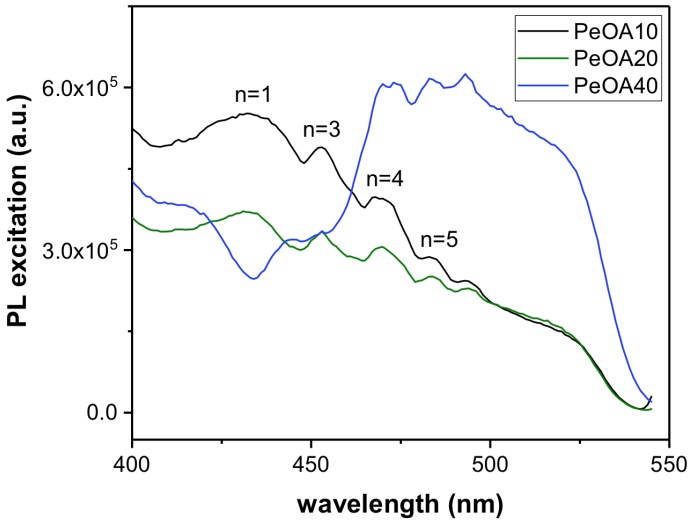

Figure 6.20: PLE spectra of the resulting samples with varying OABr contents.The 2D perovskite platelets are indexed in terms of perovskite unit cell thickness (n). Reproduced from Ref. [156] with permission from the John Wiley & Sons, Inc.

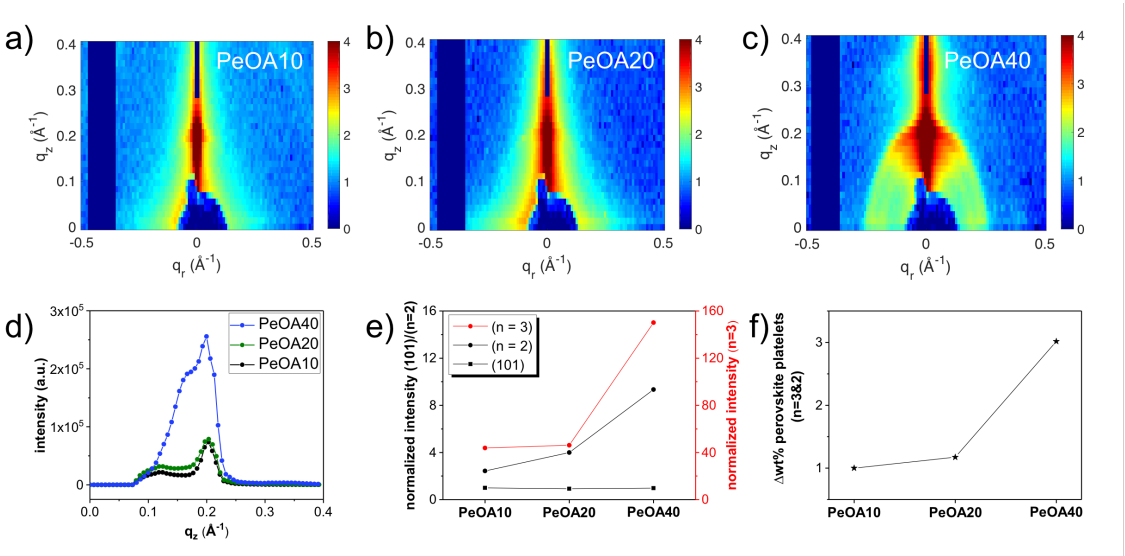

Figure 6.21: a-c) 2D GIWAXS data at low q ranges of perovskite films PeOA10, PeOA20, and PeOA40. d) Vertical cuts of the 2D GIWAXS data. e) Normalized intensity integration of the (101) and the 2D platelets reflection peaks. f) Calculated amount variation of perovskite platelets in samples containing different OABr contents. Images adapted from Ref. [156].

6.3.3 Results

The outstanding ASE threshold in sample PeOA10 is attributed to a perfectly ordered morphology, in which excitons being funneled into the bulk-like crystals under the beneficial impact of large grains and homogeneous crystal orientation. As a consequence, population inversion is promoted (Figure 6.22).

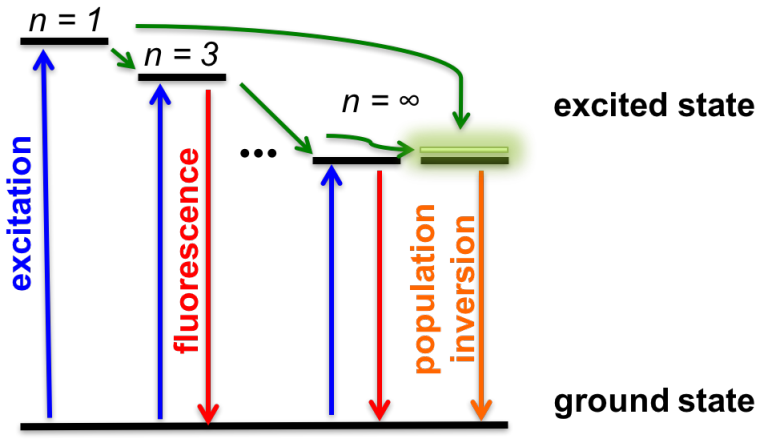

Figure 6.22: Schematic diagram of the charge carrier diffusion mechanism in the mixed dimensional perovskite films. Images adapted from Ref. [156].

6.4 Summary

In this chapter, we have correlated the morphological quality of the mixed dimensional perovskite films with its optical gain properties. It is demonstrated that the perovskite crystal orientation can be effectively manipulated by varying the OABr content. A dense film with micrometer scale domain structure is obtained in sample with 10% mole ratio of OABr. Notably, no additional solution washing or any additives is necessary for the achievement of the good quality film. Both, the film compactness as well as preferential crystal orientation are revealed loss alongside increasing OABr content. PL lifetime diminished alongside the loss in film compactness as well as identical crystal orientation. A preferential crystal orientation, together with a compact film morphology as well as a concentrated exciton population in 3D perovsktie through energy transfer from 2D quantum confined perovskite platelets secure the achievement of a ASE threshold as low as 17.8 $\mu J/cm^2$. All in all, the obtained results render these perovskite films highly interesting candidates for application as optical gain media.

7 Conclusion and outlook

In the present thesis, the main focus is to obtain a deeper understanding about the structure-property correlation of solution processed semiconductor thin films. Two material systems, P3HT-*b*-PS:PCBM BHJ blends and mixed dimensional lead bromide perovskite are investigated for their potential application of OPV and optical devices, respectively. The obtained results provide answers to questions raised at the beginning of this thesis. The addition of PCBM in P3HT-*b*-PS remarkably affects the molecular ordering of the P3HT block, the self-assembly behavior of P3HT-*b*-PS, and the vertical composition as well as the lateral domain structures of the resulting thin films. Accordingly, this morphological transformation interrelates with the variation of optoelectronic properties.

In more detail, different weight fractions of PCBM are used in preparing the P3HT-*b*-PS:PCBM BHJ blends. Both, the resulting film morphology and the optoelectronic properties closely depend on the applied PCBM content. Interestingly, different mechanisms are revealed to drive the formation of the resulting film morphology. P3HT-*b*-PS first preserves a lamellar phase in sample with the lowest PCBM weight fraction (9%), which is driven by the P3HT-block crystallization and in consistent with pure diblock copolymer. In addition, PCBM tends to interact with the PS block at this composition and distributes close to the substrate. Afterwards, the PS block swells to accommodate more PCBM molecules and a kinetically mechanism dominates in samples with moderate PCBM weight fractions (25%, 33%). Simultaneously, the ordering degree of P3HT-*b*-PS becomes less developed. On the molecular scale, the P3HT-block adopts both edge-on and face-on orientations in the films. This phase separated morphology between P3HT and PCBM hampers the exciton dissociation at the donor/acceptor interface. Therefore, the fluorescence intensity increases in both samples in comparison with sample 9%. Upon further increasing the PCBM content, a phase transition of P3HT-*b*-PS occurs on microscale and PCBM is found to distribute among the polymer domains on mesoscale (50%, 58%). Within such intermixing morphology, larger interface between P3HT and PCBM is provided and excitons can successfully split into free charge carriers. Accordingly, the fluorescence intensity dramatically quenched. In sample with the highest PCBM content (67%), microphase separation of P3HT-*b*-PS dominates and cylinders of P3HT-*b*-PS are found to pack in well developed hexagonal lattice. At this composite, PCBM forms seg-

regated domains on mesoscale. Particularly, the free exciton bandwidths of samples with a PCBM weight fraction above 50% are around 50 meV and well meets the requirement of functional solar cell device. [110]

For mixed dimensional perovskite thin films, a succinctly solution based method is established to prepare high quality planer peorvskites thin films. The crystal orientation, film compactness and domain structures can be efficiently tuned by using different amounts of the organic ligand. The ASE behavior of the resulting films closely depend on the tailored morphology, providing an alternative view for further boost its application for optical gain devices.

In more detail, the influence of the long organic ligand OABr on the morphology and optical properties of mixed dimensional lead bromide perovskite films are studied. Three different mole ratios of OABr are used in sample preparation. It is found that OABr effects as morphological template on both the preferential orientation of perovskite crystals and the domain structures. In sample containing a small mole ratio of OABr (10%), OABr adopts a perfect surface normal orientation and leads to the formation of an identical crystal orientation between 3D bulk and 2D platelets perovskite crystals. This identical crystal orientation between different dimensions of crystals is very beneficial for energy transfer between 2D platelets and 3D bulk perovskite crystals. In addition, micrometer size crystalline domains tend to grow along the in-plane direction and forms compact film. At this composition, most of 2D perovskite platelets distribute close to the film substrate. Upon increasing the OABr mole ratio from 10% to 40%, the amount of 2D platelets in the resulting thin films increased by a factor of 2 in the full film volume and accordingly excitons generated in 2D platelets are easily confined. Simultaneously, the preferential orientation of OABr vanishes and an isotropic orientation of 2D platelets accordingly arises. In addition, the film compactness and the domain size decrease. As a consequence, energy transfer from 2D platelets to 3D bulk crystals become less competent. A considerable low ASE threshold of 17.8 $\mu J/cm^2$ is determined for the sample with OABr mole ratio of 10%, which is ascribed to perfectly oriented crystals, good film compactness, longer PL lifetime and efficient energy transfer. [156]

Based on the obtained results in present thesis, several research approaches can be explored in the future investigation. Hybrid solar cells based on P3HT and ZnO are promising for OPV application due to its combined advantages of both inorganic and organic materials. [200] In the standard geometry for this kind of hybrid solar cell, P3HT is infiltrated into mesoporous ZnO network to prepare the photoactive layer. [201] To obtain high surface-to-volume ratio for sufficiently exciton dissociation, the mesoporous ZnO layer is generally nanostructured. However, this leads to great challenges to successfully fill P3HT on the nanoscale. As an alternative approach, ZnO nanoparticles that surface

coated with the same chemical nature as the non-conjugated block, can be blended with conjugated diblock copolymers. Morphological control on nanoscale and large interface areas induced by copolymer microphase separation are expected to facilitate the charge carriers separation. In order to preserve good absorption quality and the consequently solar cell performance, conjugated diblock copolymer with high molecular weight is necessary. For organometal halide perovskite, mixed dimensional perovskite thin films prepared through long organic ligand with different lengths attract interest. The selectively controllable interlayer thickness offers the possibility to stepwise understand the interaction between different perovskite layers. Secondly, in-situ understanding of the environmental influences on the morphology and optoelectronic property of perovskite nanocrystals is highly attractive. This can be carry out using small angle neutron scattering coupled with spectroscopy characterization techniques. With respect towards high environmental stability, fully inorganic low dimensional perovskite thin films attract research attention due to the replacement of water soluble ammonium constituent.

Bibliography

[1] A. Nel, T. Xia, L. Mädler, and N. Li, "Toxic potential of materials at the nanolevel," *Science*, vol. 311, no. 5761, pp. 622–627, 2006.

[2] P. V. Kamat, "Meeting the clean energy demand: nanostructure architectures for solar energy conversion," *The Journal of Physical Chemistry C*, vol. 111, no. 7, pp. 2834–2860, 2007.

[3] P. Bruce, B. Scrosati, and J.-M. Tarascon, "Nanomaterials for rechargeable lithium batteries," *Angewandte Chemie International Edition*, vol. 47, no. 16, pp. 2930–2946, 2008.

[4] A. M. Derfus, W. C. W. Chan, and S. N. Bhatia, "Probing the cytotoxicity of semiconductor quantum dots," *Nano Letters*, vol. 4, no. 1, pp. 11–18, 2004.

[5] A. E. Nel, L. Mädler, D. Velegol, T. Xia, E. M. V. Hoek, P. Somasundaran, F. Klaessig, V. Castranova, and M. Thompson, "Understanding biophysicochemical interactions at the nano–bio interface," *Nature Materials*, vol. 8, pp. 543 EP –, 06 2009.

[6] A. S. Aricò, P. Bruce, B. Scrosati, J.-M. Tarascon, and W. van Schalkwijk, "Nanostructured materials for advanced energy conversion and storage devices," *Nature Materials*, vol. 4, pp. 366 EP –, 05 2005.

[7] W. Ma, A. Gopinathan, and A. Heeger, "Nanostructure of the interpenetrating networks in poly(3-hexylthiophene)/fullerene bulk heterojunction materials: Implications for charge transport," *Advanced Materials*, vol. 19, no. 21, pp. 3656–3659, 2007.

[8] M.-Y. Chiu, U.-S. Jeng, M.-S. Su, and K.-H. Wei, "Morphologies of self-organizing regioregular conjugated polymer/fullerene aggregates in thin film solar cells," *Macromolecules*, vol. 43, no. 1, pp. 428–432, 2010.

[9] J. Y. Cheng, A. M. Mayes, and C. A. Ross, "Nanostructure engineering by templated self-assembly of block copolymers," *Nat Mater*, vol. 3, pp. 823–828, 11 2004.

[10] J. Cheng, C. Ross, H. Smith, and E. Thomas, "Templated self-assembly of block copolymers: Top-down helps bottom-up," *Advanced Materials*, vol. 18, no. 19, pp. 2505–2521, 2006.

[11] R. Dattani, J. H. Bannock, Z. Fei, R. C. I. MacKenzie, A. A. Y. Guilbert, M. S. Vezie, J. Nelson, J. C. de Mello, M. Heeney, J. T. Cabral, and A. J. Nedoma, "A general mechanism for controlling thin film structures in all-conjugated block copolymer:fullerene blends," *J. Mater. Chem. A*, vol. 2, pp. 14711–14719, 2014.

[12] T. Ishihara, J. Takahashi, and T. Goto, "Exciton state in two-dimensional perovskite semiconductor (c10h21nh3)2pbi4," *Solid State Communications*, vol. 69, no. 9, pp. 933 – 936, 1989.

[13] E. R. Dohner, E. T. Hoke, and H. I. Karunadasa, "Self-assembly of broadband white-light emitters," *Journal of the American Chemical Society*, vol. 136, no. 5, pp. 1718–1721, 2014. PMID: 24422494.

[14] L. C. Schmidt, A. Pertegás, S. González-Carrero, O. Malinkiewicz, S. Agouram, G. Mínguez Espallargas, H. J. Bolink, R. E. Galian, and J. Pérez-Prieto, "Nontemplate synthesis of ch3nh3pbbr3 perovskite nanoparticles," *Journal of the American Chemical Society*, vol. 136, no. 3, pp. 850–853, 2014. PMID: 24387158.

[15] J. A. Sichert, Y. Tong, N. Mutz, M. Vollmer, S. Fischer, K. Z. Milowska, R. García Cortadella, B. Nickel, C. Cardenas-Daw, J. K. Stolarczyk, A. S. Urban, and J. Feldmann, "Quantum size effect in organometal halide perovskite nanoplatelets," *Nano Letters*, vol. 15, no. 10, pp. 6521–6527, 2015. PMID: 26327242.

[16] P. Tyagi, S. M. Arveson, and W. A. Tisdale, "Colloidal organohalide perovskite nanoplatelets exhibiting quantum confinement," *The Journal of Physical Chemistry Letters*, vol. 6, no. 10, pp. 1911–1916, 2015. PMID: 26263268.

[17] M. Yuan, L. N. Quan, R. Comin, G. Walters, R. Sabatini, O. Voznyy, S. Hoogland, Y. Zhao, E. M. Beauregard, P. Kanjanaboos, Z. Lu, D. H. Kim, and E. H. Sargent, "Perovskite energy funnels for efficient light-emitting diodes," *Nature Nanotechnology*, vol. 11, pp. 872 EP –, 06 2016.

[18] T. M. Koh, V. Shanmugam, J. Schlipf, L. Oesinghaus, P. Müller-Buschbaum, N. Ramakrishnan, V. Swamy, N. Mathews, P. P. Boix, and S. G. Mhaisalkar, "Nanostructuring mixed-dimensional perovskites: A route toward tunable, efficient photovoltaics," *Advanced Materials*, vol. 28, no. 19, pp. 3653–3661, 2016.

[19] "1: Glossary of basic terms in polymer science (1996)," in *Compendium of Polymer Terminology and Nomenclature: IUPAC Recommendations 2008* (R. G. Jones, J. Kahovec, R. Stepto, E. S. Wilks, M. Hess, T. Kitayama, and W. V. Metanomski, eds.), pp. 3–21, The Royal Society of Chemistry, 2009.

[20] G. Strobl, *The Physics of Polymers: Concepts for Understanding their Structures and Behavior*. Springer Berlin Heidelberg, 3rd ed., 2007.

[21] W. Ring, I. Mita, A. D. Jenkins, and N. M. Bikales, "Source-based nomenclature for copolymers," *Pure and Appl. Chem.*, vol. 57, no. 10, pp. 1427–1440, 1985.

[22] N. P. Balsara, L. J. Fetters, N. Hadjichristidis, D. J. Lohse, C. C. Han, W. W. Graessley, and R. Krishnamoorti, "Thermodynamic interactions in model polyolefin blends obtained by small-angle neutron scattering," *Macromolecules*, vol. 25, no. 23, pp. 6137–6147, 1992.

[23] M. L. Huggins, "Thermodynamic properties of solutions of long-chain compounds," *Annals of the New York Academy of Sciences*, vol. 43, no. 1, pp. 1–32, 1942.

[24] P. J. Flory, "Thermodynamics of high polymer solutions," *The Journal of Chemical Physics*, vol. 10, pp. 51–61, 2017/05/26 1942.

[25] Y.-C. Tseng and S. B. Darling, "Block copolymer nanostructures for technology," *Polymers*, vol. 2, no. 4, pp. 470–489, 2010.

[26] F. S. Bates and G. H. Fredrickson, "Block copolymer thermodynamics: Theory and experiment," *Annual Review of Physical Chemistry*, vol. 41, pp. 525–557, 2017/05/28 1990.

[27] A. Salleo, T. W. Chen, A. R. Völkel, Y. Wu, P. Liu, B. S. Ong, and R. A. Street, "Intrinsic hole mobility and trapping in a regioregular poly(thiophene)," *Phys. Rev. B*, vol. 70, p. 115311, Sep 2004.

[28] M. Neumann, *Time-resolved imaging of the micro-mechanical behavior of elastomeric polypropylene.* PhD thesis, Technische Universität Chemnitz, Chemnitz, Germany, 2015.

[29] G. Strobl, "Colloquium," *Rev. Mod. Phys.*, vol. 81, pp. 1287–1300, Sep 2009.

[30] M. V. Massa and K. Dalnoki-Veress, "Homogeneous crystallization of poly(ethylene oxide) confined to droplets: The dependence of the crystal nucleation rate on length scale and temperature," *Phys. Rev. Lett.*, vol. 92, p. 255509, Jun 2004.

[31] R. Becker, "Die keimbildung bei der ausscheidung in metallischen mischkristallen," *Annalen der Physik*, vol. 424, no. 1-2, pp. 128–140, 1938.

[32] F. P. Price, *Nucleation.* Dekker, 1969.

[33] K. Tashiro, S. Sasaki, N. Gose, and M. Kobayashi, "Microscopically-viewed structural change of polyethylene during isothermal crystallization from the melt i. time-resolved ft-ir spectral measurements," *Polym J*, vol. 30, pp. 485–491, 06 1998.

[34] G. Strobl, "From the melt via mesomorphic and granular crystalline layers to lamellar crystallites: A major route followed in polymer crystallization?," *The European Physical Journal E*, vol. 3, no. 2, pp. 165–183, 2000.

[35] G. Strobl, "Crystallization and melting of bulk polymers: New observations, conclusions and a thermodynamic scheme," *Progress in Polymer Science*, vol. 31, no. 4, pp. 398 – 442, 2006.

[36] C. K. Chiang, C. R. Fincher, Y. W. Park, A. J. Heeger, H. Shirakawa, E. J. Louis, S. C. Gau, and A. G. MacDiarmid, "Electrical conductivity in doped polyacetylene," *Phys. Rev. Lett.*, vol. 39, pp. 1098–1101, Oct 1977.

[37] M. Pope and C. E. Swenberg, *Electronic Processes in Organic Crystals and Polymers*. Oxford University Press, 2nd ed., 1999.

[38] V. Shrotriya, J. Ouyang, R. J. Tseng, G. Li, and Y. Yang, "Absorption spectra modification in poly(3-hexylthiophene):methanofullerene blend thin films," *Chemical Physics Letters*, vol. 411, no. 1, pp. 138 – 143, 2005.

[39] F. Beniere, S. Haridoss, J. Louboutin, M. Aldissi, and J. Fabre, "Doping of polyacetylene by diffusion of iodine," *Journal of Physics and Chemistry of Solids*, vol. 42, no. 8, pp. 649 – 654, 1981.

[40] H. Koizumi, H. Dougauchi, and T. Ichikawa, "Mechanism of dedoping processes of conducting poly(3-alkylthiophenes)," *The Journal of Physical Chemistry B*, vol. 109, no. 32, pp. 15288–15290, 2005. PMID: 16852936.

[41] D. Hertel and H. Bässler, "Photoconduction in amorphous organic solids," *ChemPhysChem*, vol. 9, no. 5, pp. 666–688, 2008.

[42] S. Barth and H. Bässler, "Intrinsic photoconduction in ppv-type conjugated polymers," *Phys. Rev. Lett.*, vol. 79, pp. 4445–4448, Dec 1997.

[43] F. C. Spano, "The spectral signatures of frenkel polarons in h- and j-aggregates," *Accounts of Chemical Research*, vol. 43, no. 3, pp. 429–439, 2010. PMID: 20014774.

[44] P. J. Brown, D. S. Thomas, A. Köhler, J. S. Wilson, J.-S. Kim, C. M. Ramsdale, H. Sirringhaus, and R. H. Friend, "Effect of interchain interactions on the absorption and emission of poly(3-hexylthiophene)," *Phys. Rev. B*, vol. 67, p. 064203, Feb 2003.

[45] J. Clark, C. Silva, R. H. Friend, and F. C. Spano, "Role of intermolecular coupling in the photophysics of disordered organic semiconductors: Aggregate emission in regioregular polythiophene," *Phys. Rev. Lett.*, vol. 98, p. 206406, May 2007.

[46] L. Lüer, H.-J. Egelhaaf, D. Oelkrug, G. Cerullo, G. Lanzani, B.-H. Huisman, and D. de Leeuw, "Oxygen-induced quenching of photoexcited states in polythiophene films," *Organic Electronics*, vol. 5, no. 1, pp. 83 – 89, 2004. Current Trends in Crystalline Organic Semiconductors: Growth Modelling and Fundamental Properties.

[47] T. Stübinger and W. Brütting, "Exciton diffusion and optical interference in organic donor–acceptor photovoltaic cells," *Journal of Applied Physics*, vol. 90, pp. 3632–3641, 2017/06/12 2001.

[48] L. Onsager, "Initial recombination of ions," *Phys. Rev.*, vol. 54, pp. 554–557, Oct 1938.

[49] C. L. Braun, "Electric field assisted dissociation of charge transfer states as a mechanism of photocarrier production," *The Journal of Chemical Physics*, vol. 80, no. 9, pp. 4157–4161, 1984.

[50] C. Deibel, V. Dyakonov, and C. J. Brabec, "Organic bulk-heterojunction solar cells," *IEEE Journal of Selected Topics in Quantum Electronics*, vol. 16, pp. 1517–1527, Nov 2010.

[51] N. S. Sariciftci, L. Smilowitz, A. J. Heeger, and F. Wudl, "Photoinduced electron transfer from a conducting polymer to buckminsterfullerene," *Science*, vol. 258, no. 5087, pp. 1474–1476, 1992.

[52] M. Liu, M. B. Johnston, and H. J. Snaith, "Efficient planar heterojunction perovskite solar cells by vapour deposition," *Nature*, vol. 501, pp. 395–398, 09 2013.

[53] Z.-K. Tan, R. S. Moghaddam, M. L. Lai, P. Docampo, R. Higler, F. Deschler, M. Price, A. Sadhanala, L. M. Pazos, D. Credgington, F. Hanusch, T. Bein, H. J. Snaith, and R. H. Friend, "Bright light-emitting diodes based on organometal halide perovskite," *Nat Nano*, vol. 9, pp. 687–692, 09 2014.

[54] G. Xing, N. Mathews, S. S. Lim, N. Yantara, X. Liu, D. Sabba, M. Grätzel, S. Mhaisalkar, and T. C. Sum, "Low-temperature solution-processed wavelength-tunable perovskites for lasing," *Nat Mater*, vol. 13, pp. 476–480, 05 2014.

[55] Y. Chen, M. He, J. Peng, Y. Sun, and Z. Liang, "Structure and growth control of organic–inorganic halide perovskites for optoelectronics: From polycrystalline films to single crystals," *Advanced Science*, vol. 3, no. 4, pp. 1500392–n/a, 2016. 1500392.

[56] V. M. Goldschmidt, "Die gesetze der krystallochemie," *Naturwissenschaften*, vol. 14, no. 21, pp. 477–485, 1926.

[57] M. A. Green, A. Ho-Baillie, and H. J. Snaith, "The emergence of perovskite solar cells," *Nat Photon*, vol. 8, pp. 506–514, 07 2014.

[58] C. Li, X. Lu, W. Ding, L. Feng, Y. Gao, and Z. Guo, "Formability of ABX_3 (X = F, Cl, Br, I) halide perovskites," *Acta Crystallographica Section B*, vol. 64, pp. 702–707, Dec 2008.

[59] D. B. Mitzi, "Templating and structural engineering in organic-inorganic perovskites," *J. Chem. Soc., Dalton Trans.*, pp. 1–12, 2001.

[60] S. A. Veldhuis, P. P. Boix, N. Yantara, M. Li, T. C. Sum, N. Mathews, and S. G. Mhaisalkar, "Perovskite materials for light-emitting diodes and lasers," *Advanced Materials*, vol. 28, no. 32, pp. 6804–6834, 2016.

[61] M. A. Green, K. Emery, Y. Hishikawa, W. Warta, E. D. Dunlop, D. H. Levi, and A. W. Y. Ho-Baillie, "Solar cell efficiency tables (version 49)," *Progress in Photovoltaics: Research and Applications*, vol. 25, no. 1, pp. 3–13, 2017. PIP-16-252.

[62] S. De Wolf, J. Holovsky, S.-J. Moon, P. Löper, B. Niesen, M. Ledinsky, F.-J. Haug, J.-H. Yum, and C. Ballif, "Organometallic halide perovskites: Sharp optical absorption edge and its relation to photovoltaic performance," *The Journal of Physical Chemistry Letters*, vol. 5, no. 6, pp. 1035–1039, 2014. PMID: 26270984.

[63] L. M. Herz, "Charge-carrier dynamics in organic-inorganic metal halide perovskites," *Annual Review of Physical Chemistry*, vol. 67, pp. 65–89, 2016.

[64] S. D. Stranks, G. E. Eperon, G. Grancini, C. Menelaou, M. J. P. Alcocer, T. Leijtens, L. M. Herz, A. Petrozza, and H. J. Snaith, "Electron-hole diffusion lengths exceeding 1 micrometer in an organometal trihalide perovskite absorber," *Science*, vol. 342, no. 6156, pp. 341–344, 2013.

[65] N. Kitazawa, Y. Watanabe, and Y. Nakamura, "Optical properties of ch3nh3pbx3 (x = halogen) and their mixed-halide crystals," *Journal of Materials Science*, vol. 37, pp. 3585–3587, Sep 2002.

[66] G. E. Eperon, S. D. Stranks, C. Menelaou, M. B. Johnston, L. M. Herz, and H. J. Snaith, "Formamidinium lead trihalide: a broadly tunable perovskite for efficient planar heterojunction solar cells," *Energy Environ. Sci.*, vol. 7, pp. 982–988, 2014.

[67] C. Sheng, C. Zhang, Y. Zhai, K. Mielczarek, W. Wang, W. Ma, A. Zakhidov, and Z. V. Vardeny, "Exciton versus free carrier photogeneration in organometal trihalide perovskites probed by broadband ultrafast polarization memory dynamics," *Phys. Rev. Lett.*, vol. 114, p. 116601, Mar 2015.

[68] T. C. Sum, N. Mathews, G. Xing, S. S. Lim, W. K. Chong, D. Giovanni, and H. A. Dewi, "Spectral features and charge dynamics of lead halide perovskites: Origins and interpretations," *Accounts of Chemical Research*, vol. 49, no. 2, pp. 294–302, 2016. PMID: 26820796.

[69] J. Tilchin, D. N. Dirin, G. I. Maikov, A. Sashchiuk, M. V. Kovalenko, and E. Lifshitz, "Hydrogen-like wannier–mott excitons in single crystal of methylammonium lead bromide perovskite," *ACS Nano*, vol. 10, no. 6, pp. 6363–6371, 2016. PMID: 27249335.

[70] C. Wehrenfennig, G. E. Eperon, M. B. Johnston, H. J. Snaith, and L. M. Herz, "High charge carrier mobilities and lifetimes in organolead trihalide perovskites," *Advanced Materials*, vol. 26, no. 10, pp. 1584–1589, 2014.

[71] S. Keppler, A. Sävert, J. Körner, M. Hornung, H. Liebetrau, J. Hein, and M. C. Kaluza, "The generation of amplified spontaneous emission in high-power cpa laser systems," *Laser Photonics Reviews*, vol. 10, no. 2, pp. 264–277, 2016.

[72] J. V. I. Pelant, *Luminescence Spectroscopy of Semiconductors*. New York: Oxford University Press, 2012.

[73] M. Tolan, *X-Ray Scattering from Soft-Matter Thin Films*. Springer Berlin Heidelberg, 1999.

[74] R. James, *The Optical Pinciples of the Diffraction of X-rays*. Woodbridge, Connecticut: OxBow Press., 1962.

[75] P. Müller-Buschabum, *Polymer Surfaces and Interfaces: Characterization, Modification and Applications*, ch. Structure Determination in Thin Film Geometry Using Grazing Incidence Small-Angle Scattering, pp. 17–46. Springer Berlin Heidelberg, 2008.

[76] P. Müller-Buschbaum, "Gisaxs and gisans as metrology technique for understanding the 3d morphology of block copolymer thin films," *European Polymer Journal*, vol. 81, pp. 470 – 493, 2016.

[77] H. Dosch, *Critical phenomena at surfaces and interfaces: evanescent X-ray and neutron scattering*. Berlin: Springer-Verlag, 1992.

[78] H. Dosch, B. W. Batterman, and D. C. Wack, "Depth-controlled grazing-incidence diffraction of synchrotron x radiation," *Phys. Rev. Lett.*, vol. 56, pp. 1144–1147, Mar 1986.

[79] W. Rodrigues, "X-ray scattering studies of surfactant mediated epitaxial growth of si/ge/si(001) heterostructures," *Journal of Applied Physics*, vol. 88, pp. 2391–2394, 2017/05/09 2000.

[80] L. G. Parratt, "Surface studies of solids by total reflection of x-rays," *Phys. Rev.*, vol. 95, pp. 359–369, Jul 1954.

[81] L. Nevot and P. Croce, "Characterization of surfaces by grazing x-ray reflection–application to the study of polishing of some silicate glasses," *Rev. Phys. Appl.*, vol. 15, no. 761, 1980.

[82] H. Kiessig, "Interferenz von röntgenstrahlen an dünnen schichten," *Ann. Phys.*, vol. 10, pp. 769–788, 1931.

[83] A. Guinier, *X-ray diffraction in crystals, imperfect crystals, and amorphous bodies*. Dover Publications, 1994.

[84] T. Hippler, S. Jiang, and G. Strobl, "Block formation during polymer crystallization," *Macromolecules*, vol. 38, no. 22, pp. 9396–9397, 2005.

[85] O. F. Pascui, R. Lohwasser, M. Sommer, M. Thelakkat, T. Thurn-Albrecht, and K. Saalwächter, "High crystallinity and nature of crystal−crystal phase transformations in regioregular poly(3-hexylthiophene)," *Macromolecules*, vol. 43, no. 22, pp. 9401–9410, 2010.

[86] J. Rivnay, S. C. B. Mannsfeld, C. E. Miller, A. Salleo, and M. F. Toney, "Quantitative determination of organic semiconductor microstructure from the molecular to device scale," *Chemical Reviews*, vol. 112, no. 10, pp. 5488–5519, 2012. PMID: 22877516.

[87] R. Lazzari, "*IsGISAXS*: a program for grazing-incidence small-angle X-ray scattering analysis of supported islands," *Journal of Applied Crystallography*, vol. 35, pp. 406–421, Aug 2002.

[88] S. K. Sinha, E. B. Sirota, S. Garoff, and H. B. Stanley, "X-ray and neutron scattering from rough surfaces," *Phys. Rev. B*, vol. 38, pp. 2297–2311, Aug 1988.

[89] V. Holý and T. Baumbach, "Nonspecular x-ray reflection from rough multilayers," *Phys. Rev. B*, vol. 49, pp. 10668–10676, Apr 1994.

[90] Y. Yoneda, "Anomalous surface reflection of x rays," *Phys. Rev.*, vol. 131, pp. 2010–2013, Sep 1963.

[91] Z. Jiang, "*GIXSGUI*: a MATLAB toolbox for grazing-incidence X-ray scattering data visualization and reduction, and indexing of buried three-dimensional periodic nanostructured films," *Journal of Applied Crystallography*, vol. 48, pp. 917–926, Jun 2015.

[92] Z. Jiang, *Documentation for gixsgui - 1.6.1.*

[93] N. Klein-Kedem, D. Cahen, and G. Hodes, "Effects of light and electron beam irradiation on halide perovskites and their solar cells," *Accounts of Chemical Research*, vol. 49, no. 2, pp. 347–354, 2016. PMID: 26807647.

[94] J. S. Bendat and A. G. Piersol, *Random Data: Analysis and Measurement Procedures*. New York: Wiley-Interscience, 1971.

[95] J. S. Gutmann, P. Muller-Buschbaum, and M. Stamm, "Complex pattern formation by phase separation of polymer blends in thin films," *Faraday Discuss.*, vol. 112, pp. 285–297, 1999.

[96] A. Nelson, "Co-refinement of multiple-contrast neutron/x-ray reflectivity data using motofit," *Journal of Applied Crystallography*, vol. 39, pp. 273–276, Apr 2006.

[97] J. C. f. N. S. Forchungszentrum Jülich, "Galaxi: Gallium anode low-angel x-ray instrument," *Journal of large-scale research facilities*, vol. 2, p. A61, 2016.

[98] M. A. Ruderer, R. Meier, L. Porcar, R. Cubitt, and P. Müller-Buschbaum, "Phase separation and molecular intermixing in polymer–fullerene bulk heterojunction thin films," *The Journal of Physical Chemistry Letters*, vol. 3, no. 6, pp. 683–688, 2012. PMID: 26286273.

[99] H. M.-L. Z. et al., "Kws-1: Small-angle scattering diffractometer," *Journal of large-scale research facilities*, vol. 1, no. A28, 2015.

[100] H. M.-L. Z. et al., "Kws-3: Very small angle scattering diffractometer with focusing mirror," *Journal of large-scale research facilities*, vol. 1, no. A31, 2015.

[101] M. Sommer, S. Lindner, and M. Thelakkat, "Microphase-separated donor–acceptor diblock copolymers: Influence of homo energy levels and morphology on polymer solar cells," *Advanced Functional Materials*, vol. 17, no. 9, pp. 1493–1500, 2007.

[102] J. U. Lee, A. Cirpan, T. Emrick, T. P. Russell, and W. H. Jo, "Synthesis and photophysical property of well-defined donor-acceptor diblock copolymer based on regioregular poly(3-hexylthiophene) and fullerene," *J. Mater. Chem.*, vol. 19, pp. 1483–1489, 2009.

[103] M. T. Dang, L. Hirsch, and G. Wantz, "P3ht:pcbm, best seller in polymer photovoltaic research," *Advanced Materials*, vol. 23, no. 31, pp. 3597–3602, 2011.

[104] C. J. Brabec, N. S. Sariciftci, and J. C. Hummelen, "Plastic solar cells," *Advanced Functional Materials*, vol. 11, no. 1, pp. 15–26, 2001.

[105] R. H. Friend, R. W. Gymer, A. B. Holmes, J. H. Burroughes, R. N. Marks, C. Taliani, D. D. C. Bradley, D. A. D. Santos, J. L. Bredas, M. Logdlund, and W. R. Salaneck, "Electroluminescence in conjugated polymers," *Nature*, vol. 397, pp. 121–128, 01 1999.

[106] P. Müller-Buschbaum, N. Hermsdorf, S. V. Roth, J. Wiedersich, S. Cunis, and R. Gehrke, "Comparative analysis of nanostructured diblock copolymer films," *Spectrochimica Acta Part B: Atomic Spectroscopy*, vol. 59, pp. 1789–1797, 10 2004.

[107] D. W. Schubert and T. Dunkel, "Spin coating from a molecular point of view: its concentration regimes, influence of molar mass and distribution," *Materials Research Innovations*, vol. 7, no. 5, pp. 314–321, 2003.

[108] M. Saliba, K. W. Tan, H. Sai, D. T. Moore, T. Scott, W. Zhang, L. A. Estroff, U. Wiesner, and H. J. Snaith, "Influence of thermal processing protocol upon the crystallization and photovoltaic performance of organic–inorganic lead trihalide perovskites," *The Journal of Physical Chemistry C*, vol. 118, pp. 17171–17177, 07 2014.

[109] J. H. Heo, D. H. Song, and S. H. Im, "Planar ch3nh3pbbr3 hybrid solar cells with 10.4crystallization in the spin-coating process," *Advanced Materials*, vol. 26, no. 48, pp. 8179–8183, 2014.

[110] R. Wang, Z.-Y. Di, P. Müller-Buschbaum, and H. Frielinghaus, "Effect of pcbm additive on morphology and optoelectronic properties of p3ht-b-ps films," *Polymer*, vol. 121, pp. 173 – 182, 2017.

[111] T. Smart, H. Lomas, M. Massignani, M. V. Flores-Merino, L. R. Perez, and G. Battaglia, "Block copolymer nanostructures," *Nano Today*, vol. 3, no. 3–4, pp. 38 – 46, 2008.

[112] J. Bang, U. Jeong, D. Y. Ryu, T. P. Russell, and C. J. Hawker, "Block copolymer nanolithography: Translation of molecular level control to nanoscale patterns," *Advanced Materials*, vol. 21, no. 47, pp. 4769–4792, 2009.

[113] L. Leibler, "Theory of microphase separation in block copolymers," *Macromolecules*, vol. 13, no. 6, pp. 1602–1617, 1980.

[114] H.-C. Kim, S.-M. Park, and W. D. Hinsberg, "Block copolymer based nanostructures: Materials, processes, and applications to electronics," *Chemical Reviews*, vol. 110, no. 1, pp. 146–177, 2010. PMID: 19950962.

[115] E. Metwalli, M. Rasool, S. Brunner, and P. Müller-Buschbaum, "Lithium-salt-containing high-molecular-weight polystyrene-block-polyethylene oxide block copolymer films," *ChemPhysChem*, vol. 16, no. 13, pp. 2882–2889, 2015.

[116] K. Kataoka, A. Harada, and Y. Nagasaki, "Block copolymer micelles for drug delivery: design, characterization and biological significance," *Advanced Drug Delivery Reviews*, vol. 47, no. 1, pp. 113 – 131, 2001. Nanoparticulate Systems for Improved Drug Delivery.

[117] S.-H. Lin, C.-C. Ho, and W.-F. Su, "Cylinder-to-gyroid phase transition in a rod-coil diblock copolymer," *Soft Matter*, vol. 8, pp. 4890–4893, 2012.

[118] H.-A. Klok and S. Lecommandoux, "Supramolecular materials via block copolymer self-assembly," *Advanced Materials*, vol. 13, no. 16, pp. 1217–1229, 2001.

[119] B. D. Olsen and R. A. Segalman, "Nonlamellar phases in asymmetric rod−coil block copolymers at increased segregation strengths," *Macromolecules*, vol. 40, no. 19, pp. 6922–6929, 2007.

[120] N. Sary, L. Rubatat, C. Brochon, G. Hadziioannou, J. Ruokolainen, and R. Mezzenga, "Self-assembly of poly(diethylhexyloxy-p-phenylenevinylene)-b-poly(4-vinylpyridine) rod−coil block copolymer systems," *Macromolecules*, vol. 40, no. 19, pp. 6990–6997, 2007.

[121] C.-C. Ho, Y.-H. Lee, C.-A. Dai, R. A. Segalman, and W.-F. Su, "Synthesis and self-assembly of poly(diethylhexyloxy-p-phenylenevinylene)-b-poly(methyl methacrylate) rod−coil block copolymers," *Macromolecules*, vol. 42, no. 12, pp. 4208–4219, 2009.

[122] U. Scherf, S. Adamczyk, A. Gutacker, and N. Koenen, "All-conjugated, rod-rod block copolymers-generation and self-assembly properties," *Macromolecular Rapid Communications*, vol. 30, no. 13, pp. 1059–1065, 2009.

[123] M. A. Ruderer and P. Muller-Buschbaum, "Morphology of polymer-based bulk heterojunction films for organic photovoltaics," *Soft Matter*, vol. 7, pp. 5482–5493, 2011.

[124] C. R. McNeill, B. Watts, L. Thomsen, H. Ade, N. C. Greenham, and P. C. Dastoor, "X-ray microscopy of photovoltaic polyfluorene blends: relating nanomorphology to device performance," *Macromolecules*, vol. 40, no. 9, pp. 3263–3270, 2007.

[125] V. Ho, B. W. Boudouris, B. L. McCulloch, C. G. Shuttle, M. Burkhardt, M. L. Chabinyc, and R. A. Segalman, "Poly(3-alkylthiophene) diblock copolymers with ordered microstructures and continuous semiconducting pathways," *Journal of the American Chemical Society*, vol. 133, no. 24, pp. 9270–9273, 2011. PMID: 21608996.

[126] B. W. Boudouris, C. D. Frisbie, and M. A. Hillmyer, "Polylactide−polythiophene−polylactide triblock copolymers," *Macromolecules*, vol. 43, no. 7, pp. 3566–3569, 2010.

[127] H. Yang, S. W. LeFevre, C. Y. Ryu, and Z. Bao, "Solubility-driven thin film structures of regioregular poly(3-hexyl thiophene) using volatile solvents," *Applied Physics Letters*, vol. 90, no. 17, p. 172116, 2007.

[128] C.-W. Chu, H. Yang, W.-J. Hou, J. Huang, G. Li, and Y. Yang, "Control of the nanoscale crystallinity and phase separation in polymer solar cells," *Applied Physics Letters*, vol. 92, no. 10, p. 103306, 2008.

[129] Z. Sun, K. Xiao, J. K. Keum, X. Yu, K. Hong, J. Browning, I. N. Ivanov, J. Chen, J. Alonzo, D. Li, B. G. Sumpter, E. A. Payzant, C. M. Rouleau, and D. B. Geohegan, "Ps-b-p3ht copolymers as p3ht/pcbm interfacial compatibilizers for high efficiency photovoltaics," *Advanced Materials*, vol. 23, no. 46, pp. 5529–5535, 2011.

[130] Y. Lin, V. K. Daga, E. R. Anderson, S. P. Gido, and J. J. Watkins, "Nanoparticle-driven assembly of block copolymers: A simple route to ordered hybrid materials," *Journal of the American Chemical Society*, vol. 133, no. 17, pp. 6513–6516, 2011. PMID: 21480650.

[131] Y. Lin, J. A. Lim, Q. Wei, S. C. B. Mannsfeld, A. L. Briseno, and J. J. Watkins, "Co-operative assembly of hydrogen-bonded diblock copolythiophene/fullerene blends for photovoltaic devices with well-defined morphologies and enhanced stability," *Chemistry of Materials*, vol. 24, no. 3, pp. 622–632, 2012.

[132] W. Wang, S. Guo, E. M. Herzig, K. Sarkar, M. Schindler, D. Magerl, M. Philipp, J. Perlich, and P. Muller-Buschbaum, "Investigation of morphological degradation

of p3ht:pcbm bulk heterojunction films exposed to long-term host solvent vapor," *J. Mater. Chem. A*, vol. 4, pp. 3743–3753, 2016.

[133] M. A. Ruderer, S. Guo, R. Meier, H.-Y. Chiang, V. Körstgens, J. Wiedersich, J. Perlich, S. V. Roth, and P. Müller-Buschbaum, "Solvent-induced morphology in polymer-based systems for organic photovoltaics," *Advanced Functional Materials*, vol. 21, no. 17, pp. 3382–3391, 2011.

[134] C. J. Schaffer, J. Schlipf, E. Dwi Indari, B. Su, S. Bernstorff, and P. Müller-Buschbaum, "Effect of blend composition and additives on the morphology of pcpdtbt:pc71bm thin films for organic photovoltaics," *ACS Applied Materials & Interfaces*, vol. 7, no. 38, pp. 21347–21355, 2015. PMID: 26355854.

[135] F. C. Spano, J. Clark, C. Silva, and R. H. Friend, "Determining exciton coherence from the photoluminescence spectral line shape in poly(3-hexylthiophene) thin films," *The Journal of Chemical Physics*, vol. 130, no. 7, p. 074904, 2009.

[136] P. E. Shaw, A. Ruseckas, and I. D. W. Samuel, "Exciton diffusion measurements in poly(3-hexylthiophene)," *Advanced Materials*, vol. 20, no. 18, pp. 3516–3520, 2008.

[137] Y. Gao, T. P. Martin, E. T. Niles, A. J. Wise, A. K. Thomas, and J. K. Grey, "Understanding morphology-dependent polymer aggregation properties and photocurrent generation in polythiophene/fullerene solar cells of variable compositions," *The Journal of Physical Chemistry C*, vol. 114, no. 35, pp. 15121–15128, 2010.

[138] S. S. van Bavel, M. Bärenklau, G. de With, H. Hoppe, and J. Loos, "P3ht/pcbm bulk heterojunction solar cells: Impact of blend composition and 3d morphology on device performance," *Advanced Functional Materials*, vol. 20, no. 9, pp. 1458–1463, 2010.

[139] D. Chen, F. Liu, C. Wang, A. Nakahara, and T. P. Russell, "Bulk heterojunction photovoltaic active layers via bilayer interdiffusion," *Nano Letters*, vol. 11, no. 5, pp. 2071–2078, 2011. PMID: 21476579.

[140] A. J. Parnell, A. D. F. Dunbar, A. J. Pearson, P. A. Staniec, A. J. C. Dennison, H. Hamamatsu, M. W. A. Skoda, D. G. Lidzey, and R. A. L. Jones, "Depletion of pcbm at the cathode interface in p3ht/pcbm thin films as quantified via neutron reflectivity measurements," *Advanced Materials*, vol. 22, no. 22, pp. 2444–2447, 2010.

[141] L.-M. Chen, Z. Xu, Z. Hong, and Y. Yang, "Interface investigation and engineering - achieving high performance polymer photovoltaic devices," *J. Mater. Chem.*, vol. 20, pp. 2575–2598, 2010.

[142] J. W. Kiel, B. J. Kirby, C. F. Majkrzak, B. B. Maranville, and M. E. Mackay,

"Nanoparticle concentration profile in polymer-based solar cells," *Soft Matter*, vol. 6, pp. 641–646, 2010.

[143] H.-J. Liu, U.-S. Jeng, N. L. Yamada, A.-C. Su, W.-R. Wu, C.-J. Su, S.-J. Lin, K.-H. Wei, and M.-Y. Chiu, "Surface and interface porosity of polymer/fullerene-derivative thin films revealed by contrast variation of neutron and x-ray reflectivity," *Soft Matter*, vol. 7, pp. 9276–9282, 2011.

[144] H. Zhong, X. Yang, B. deWith, and J. Loos, "Quantitative insight into morphology evolution of thin ppv/pcbm composite films upon thermal treatment," *Macromolecules*, vol. 39, no. 1, pp. 218–223, 2006.

[145] B. Watts, W. J. Belcher, L. Thomsen, H. Ade, and P. C. Dastoor, "A quantitative study of pcbm diffusion during annealing of p3ht:pcbm blend films," *Macromolecules*, vol. 42, no. 21, pp. 8392–8397, 2009.

[146] S. Berson, R. De Bettignies, S. Bailly, and S. Guillerez, "Poly(3-hexylthiophene) fibers for photovoltaic applications," *Advanced Functional Materials*, vol. 17, no. 8, pp. 1377–1384, 2007.

[147] X. Yang, J. Loos, S. C. Veenstra, W. J. H. Verhees, M. M. Wienk, J. M. Kroon, M. A. J. Michels, and R. A. J. Janssen, "Nanoscale morphology of high-performance polymer solar cells," *Nano Letters*, vol. 5, no. 4, pp. 579–583, 2005. PMID: 15826090.

[148] B. A. Collins, E. Gann, L. Guignard, X. He, C. R. McNeill, and H. Ade, "Molecular miscibility of polymer−fullerene blends," *The Journal of Physical Chemistry Letters*, vol. 1, no. 21, pp. 3160–3166, 2010.

[149] J. Higgins and H. Benoit, *Polymers and Neutron Scattering*. New York, USA: Oxford University Press Inc., 1997.

[150] R. Roe, *Methods of X-ray and Neutron Scattering in Polymer Science*. New York, USA: Oxford University Press Inc., 2000.

[151] O. V. Mikhnenko, H. Azimi, M. Scharber, M. Morana, P. W. M. Blom, and M. A. Loi, "Exciton diffusion length in narrow bandgap polymers," *Energy Environ. Sci.*, vol. 5, pp. 6960–6965, 2012.

[152] I. Tokarev, R. Krenek, Y. Burkov, D. Schmeisser, A. Sidorenko, S. Minko, and M. Stamm, "Microphase separation in thin films of poly(styrene-block-4-vinylpyridine) copolymer−2-(4'-hydroxybenzeneazo)benzoic acid assembly," *Macromolecules*, vol. 38, no. 2, pp. 507–516, 2005.

[153] V. R. Tirumala, A. Romang, S. Agarwal, E. K. Lin, and J. J. Watkins, "Well ordered polymer melts from blends of disordered triblock copolymer surfactants and functional homopolymers," *Advanced Materials*, vol. 20, no. 9, pp. 1603–1608, 2008.

[154] K. I. Winey, E. L. Thomas, and L. J. Fetters, "Ordered morphologies in binary blends of diblock copolymer and homopolymer and characterization of their intermaterial dividing surfaces," *The Journal of Chemical Physics*, vol. 95, no. 12, pp. 9367–9375, 1991.

[155] M. E. Vigild, K. Almdal, K. Mortensen, I. W. Hamley, J. P. A. Fairclough, and A. J. Ryan, "Transformations to and from the gyroid phase in a diblock copolymer," *Macromolecules*, vol. 31, no. 17, pp. 5702–5716, 1998.

[156] R. Wang, Y. Tong, A. Manzi, K. Wang, Z. Fu, E. Kentzinder, J. Feldmann, A. Urban, H. Frielinghaus, and P. Müller-Buschbaum, "Preferential orientation of crystals induced by incorporation of organic ligands in mixed-dimensional hybrid perovskite films," *Advanced Optical Materials*, vol. 6, p. 1701311, 2018.

[157] F. Li, C. Ma, H. Wang, W. Hu, W. Yu, A. D. Sheikh, and T. Wu, "Ambipolar solution-processed hybrid perovskite phototransistors," *Nature Communications*, vol. 6, pp. 8238 EP –, 09 2015.

[158] G. Xing, N. Mathews, S. Sun, S. S. Lim, Y. M. Lam, M. Grätzel, S. Mhaisalkar, and T. C. Sum, "Long-range balanced electron- and hole-transport lengths in organic-inorganic ch3nh3pbi3," *Science*, vol. 342, no. 6156, pp. 344–347, 2013.

[159] L. Protesescu, S. Yakunin, M. I. Bodnarchuk, F. Krieg, R. Caputo, C. H. Hendon, R. X. Yang, A. Walsh, and M. V. Kovalenko, "Nanocrystals of cesium lead halide perovskites (cspbx3, x = cl, br, and i): Novel optoelectronic materials showing bright emission with wide color gamut," *Nano Letters*, vol. 15, no. 6, pp. 3692–3696, 2015. PMID: 25633588.

[160] J. Huang, Y. Shao, and Q. Dong, "Organometal trihalide perovskite single crystals: A next wave of materials for 25% efficiency photovoltaics and applications beyond?," *The Journal of Physical Chemistry Letters*, vol. 6, no. 16, pp. 3218–3227, 2015.

[161] N. J. Jeon, J. H. Noh, Y. C. Kim, W. S. Yang, S. Ryu, and S. I. Seok, "Solvent engineering for high-performance inorganic–organic hybrid perovskite solar cells," *Nat Mater*, vol. 13, pp. 897–903, 09 2014.

[162] H.-S. Kim, C.-R. Lee, J.-H. Im, K.-B. Lee, T. Moehl, A. Marchioro, S.-J. Moon, R. Humphry-Baker, J.-H. Yum, J. E. Moser, M. Grätzel, and N.-G. Park, "Lead iodide perovskite sensitized all-solid-state submicron thin film mesoscopic solar cell with efficiency exceeding 9%," *Scientific Reports*, vol. 2, pp. 591 EP –, 08 2012.

[163] J. M. Ball, M. M. Lee, A. Hey, and H. J. Snaith, "Low-temperature processed meso-superstructured to thin-film perovskite solar cells," *Energy Environ. Sci.*, vol. 6, pp. 1739–1743, 2013.

[164] H. Zhou, Q. Chen, G. Li, S. Luo, T.-b. Song, H.-S. Duan, Z. Hong, J. You, Y. Liu, and Y. Yang, "Interface engineering of highly efficient perovskite solar cells," *Science*, vol. 345, no. 6196, pp. 542–546, 2014.

[165] S. D. Stranks and H. J. Snaith, "Metal-halide perovskites for photovoltaic and light-emitting devices," *Nat Nano*, vol. 10, pp. 391–402, 05 2015.

[166] Y.-H. Kim, H. Cho, J. H. Heo, T.-S. Kim, N. Myoung, C.-L. Lee, S. H. Im, and T.-W. Lee, "Multicolored organic/inorganic hybrid perovskite light-emitting diodes," *Advanced Materials*, vol. 27, no. 7, pp. 1248–1254, 2015.

[167] F. Deschler, M. Price, S. Pathak, L. E. Klintberg, D.-D. Jarausch, R. Higler, S. Hüttner, T. Leijtens, S. D. Stranks, H. J. Snaith, M. Atatüre, R. T. Phillips, and R. H. Friend, "High photoluminescence efficiency and optically pumped lasing in solution-processed mixed halide perovskite semiconductors," *The Journal of Physical Chemistry Letters*, vol. 5, no. 8, pp. 1421–1426, 2014. PMID: 26269988.

[168] L. Dou, Y. M. Yang, J. You, Z. Hong, W.-H. Chang, G. Li, and Y. Yang, "Solution-processed hybrid perovskite photodetectors with high detectivity," *Nature Communications*, vol. 5, pp. 5404 EP –, 11 2014.

[169] Y. Fang, Q. Dong, Y. Shao, Y. Yuan, and J. Huang, "Highly narrowband perovskite single-crystal photodetectors enabled by surface-charge recombination," *Nat Photon*, vol. 9, pp. 679–686, 10 2015.

[170] M. Gratzel, "The light and shade of perovskite solar cells," *Nat Mater*, vol. 13, pp. 838–842, 09 2014.

[171] T. C. Sum and N. Mathews, "Advancements in perovskite solar cells: photophysics behind the photovoltaics," *Energy Environ. Sci.*, vol. 7, pp. 2518–2534, 2014.

[172] N. Kitazawa and Y. Watanabe, "Optical properties of natural quantum-well compounds (c6h5-cnh2n-nh3)2pbbr4 (n=1–4)," *Journal of Physics and Chemistry of Solids*, vol. 71, no. 5, pp. 797 – 802, 2010.

[173] Z. Xiao, R. A. Kerner, L. Zhao, N. L. Tran, K. M. Lee, T.-W. Koh, G. D. Scholes, and B. P. Rand, "Efficient perovskite light-emitting diodes featuring nanometre-sized crystallites," *Nat Photon*, vol. 11, pp. 108–115, 02 2017.

[174] Y. Tong, F. Ehrat, W. Vanderlinden, C. Cardenas-Daw, J. K. Stolarczyk, L. Polavarapu, and A. S. Urban, "Dilution-induced formation of hybrid perovskite nanoplatelets," *ACS Nano*, vol. 10, no. 12, pp. 10936–10944, 2016. PMID: 28024369.

[175] M. C. Weidman, M. Seitz, S. D. Stranks, and W. A. Tisdale, "Highly tunable colloidal perovskite nanoplatelets through variable cation, metal, and halide composition," *ACS Nano*, vol. 10, no. 8, pp. 7830–7839, 2016. PMID: 27471862.

[176] M. Pandey, K. W. Jacobsen, and K. S. Thygesen, "Band gap tuning and defect tolerance of atomically thin two-dimensional organic–inorganic halide perovskites," *The Journal of Physical Chemistry Letters*, vol. 7, no. 21, pp. 4346–4352, 2016.

[177] M. Imran, F. Di Stasio, Z. Dang, C. Canale, A. H. Khan, J. Shamsi, R. Brescia, M. Prato, and L. Manna, "Colloidal synthesis of strongly fluorescent cspbbr3 nanowires with width tunable down to the quantum confinement regime," *Chemistry of Materials*, vol. 28, no. 18, pp. 6450–6454, 2016.

[178] D. Amgar, A. Stern, D. Rotem, D. Porath, and L. Etgar, "Tunable length and optical properties of cspbx3 (x = cl, br, i) nanowires with a few unit cells," *Nano Letters*, vol. 17, no. 2, pp. 1007–1013, 2017. PMID: 28094960.

[179] N. Kitazawa, D. Yaemponga, M. Aono, and Y. Watanabe, "Optical properties of organic–inorganic hybrid films prepared by the two-step growth process," *Journal of Luminescence*, vol. 129, no. 9, pp. 1036 – 1041, 2009.

[180] G. Papavassiliou and I. Koutselas, "Structural, optical and related properties of some natural three- and lower-dimensional semiconductor systems," *Synthetic Metals*, vol. 71, no. 1, pp. 1713 – 1714, 1995.

[181] C. de Weerd, L. Gomez, H. Zhang, W. J. Buma, G. Nedelcu, M. V. Kovalenko, and T. Gregorkiewicz, "Energy transfer between inorganic perovskite nanocrystals," *The Journal of Physical Chemistry C*, vol. 120, no. 24, pp. 13310–13315, 2016.

[182] N. K. Noel, A. Abate, S. D. Stranks, E. S. Parrott, V. M. Burlakov, A. Goriely, and H. J. Snaith, "Enhanced photoluminescence and solar cell performance via lewis base passivation of organic–inorganic lead halide perovskites," *ACS Nano*, vol. 8, pp. 9815–9821, 10 2014.

[183] A. Ng, Z. Ren, Q. Shen, S. H. Cheung, H. C. Gokkaya, G. Bai, J. Wang, L. Yang, S. K. So, A. B. Djurisic, W. W.-f. Leung, J. Hao, W. K. Chan, and C. Surya, "Efficiency enhancement by defect engineering in perovskite photovoltaic cells prepared using evaporated pbi2/ch3nh3i multilayers," *J. Mater. Chem. A*, vol. 3, pp. 9223–9231, 2015.

[184] X. Hong, T. Ishihara, and A. V. Nurmikko, "Dielectric confinement effect on excitons in pbi_4-based layered semiconductors," *Phys. Rev. B*, vol. 45, pp. 6961–6964, Mar 1992.

[185] L. Zhao, Y.-W. Yeh, N. L. Tran, F. Wu, Z. Xiao, R. A. Kerner, Y. L. Lin, G. D. Scholes, N. Yao, and B. P. Rand, "In situ preparation of metal halide perovskite nanocrystal thin films for improved light-emitting devices," *ACS Nano*, vol. 11, no. 4, pp. 3957–3964, 2017. PMID: 28332818.

[186] V. A. Hintermayr, A. F. Richter, F. Ehrat, M. Döblinger, W. Vanderlinden, J. A. Sichert, Y. Tong, L. Polavarapu, J. Feldmann, and A. S. Urban, "Tuning the optical properties of perovskite nanoplatelets through composition and thickness by ligand-assisted exfoliation," *Advanced Materials*, vol. 28, no. 43, pp. 9478–9485, 2016.

[187] J. H. Noh, S. H. Im, J. H. Heo, T. N. Mandal, and S. I. Seok, "Chemical management for colorful, efficient, and stable inorganic–organic hybrid nanostructured solar cells," *Nano Letters*, vol. 13, no. 4, pp. 1764–1769, 2013. PMID: 23517331.

[188] M. Xiao, F. Huang, W. Huang, Y. Dkhissi, Y. Zhu, J. Etheridge, A. Gray-Weale, U. Bach, Y.-B. Cheng, and L. Spiccia, "A fast deposition-crystallization procedure for highly efficient lead iodide perovskite thin-film solar cells," *Angewandte Chemie*, vol. 126, no. 37, pp. 10056–10061, 2014.

[189] H. Cho, S.-H. Jeong, M.-H. Park, Y.-H. Kim, C. Wolf, C.-L. Lee, J. H. Heo, A. Sadhanala, N. Myoung, S. Yoo, S. H. Im, R. H. Friend, and T.-W. Lee, "Overcoming the electroluminescence efficiency limitations of perovskite light-emitting diodes," *Science*, vol. 350, no. 6265, pp. 1222–1225, 2015.

[190] J. Liang, Y. Zhang, X. Guo, Z. Gan, J. Lin, Y. Fan, and X. Liu, "Efficient perovskite light-emitting diodes by film annealing temperature control," *RSC Adv.*, vol. 6, pp. 71070–71075, 2016.

[191] B. A. Collins, J. R. Tumbleston, and H. Ade, "Miscibility, crystallinity, and phase development in p3ht/pcbm solar cells: Toward an enlightened understanding of device morphology and stability," *The Journal of Physical Chemistry Letters*, vol. 2, no. 24, pp. 3135–3145, 2011.

[192] Y.-C. Huang, C.-S. Tsao, Y.-J. Cho, K.-C. Chen, K.-M. Chiang, S.-Y. Hsiao, C.-W. Chen, C.-J. Su, U.-S. Jeng, and H.-W. Lin, "Insight into evolution, processing and performance of multi-length-scale structures in planar heterojunction perovskite solar cells," *Scientific Reports*, vol. 5, pp. 13657 EP –, 09 2015.

[193] J. Schlipf, P. Docampo, C. J. Schaffer, V. Körstgens, L. Bießmann, F. Hanusch, N. Giesbrecht, S. Bernstorff, T. Bein, and P. Müller-Buschbaum, "A closer look into two-step perovskite conversion with x-ray scattering," *The Journal of Physical Chemistry Letters*, vol. 6, no. 7, pp. 1265–1269, 2015. PMID: 26262985.

[194] H.-C. Liao, C.-S. Tsao, M.-H. Jao, J.-J. Shyue, C.-P. Hsu, Y.-C. Huang, K.-Y. Tian, C.-Y. Chen, C.-J. Su, and W.-F. Su, "Hierarchical i-p and i-n porous heterojunction in planar perovskite solar cells," *J. Mater. Chem. A*, vol. 3, pp. 10526–10535, 2015.

[195] G. Beaucage, "Small-Angle Scattering from Polymeric Mass Fractals of Arbitrary Mass-Fractal Dimension," *Journal of Applied Crystallography*, vol. 29, pp. 134–146, Apr 1996.

[196] D. Ma, A. D. Stoica, and X. L. Wang, "Power-law scaling and fractal nature of medium-range order in metallic glasses," *Nat Mater*, vol. 8, pp. 30–34, 01 2009.

[197] H. Frielinghaus, "Small-angle scattering model for multilamellar vesicles," *Phys. Rev. E*, vol. 76, p. 051603, Nov 2007.

[198] J. E. Martin and A. J. Hurd, "Scattering from fractals," *Journal of Applied Crystallography*, vol. 20, pp. 61–78, Apr 1987.

[199] J. Feldmann, G. Peter, E. O. Göbel, P. Dawson, K. Moore, C. Foxon, and R. J. Elliott, "Linewidth dependence of radiative exciton lifetimes in quantum wells," *Phys. Rev. Lett.*, vol. 59, pp. 2337–2340, Nov 1987.

[200] W. Beek, M. Wienk, and R. Janssen, "Hybrid solar cells from regioregular polythiophene and zno nanoparticles," *Advanced Functional Materials*, vol. 16, no. 8, pp. 1112–1116, 2006.

[201] D. C. Olson, S. E. Shaheen, R. T. Collins, and D. S. Ginley, "The effect of atmosphere and zno morphology on the performance of hybrid poly(3-hexylthiophene)/zno nanofiber photovoltaic devices," *The Journal of Physical Chemistry C*, vol. 111, no. 44, pp. 16670–16678, 2007.

List of publications

Publications related to the dissertation

- R. Wang, Z.-Y. Di, P. Müller-Buschbaum, H. Frielinghaus "Effect of PCBM additive on morphology and optoelectronic properties of P3HT-*b*-PS films", *Polymer*, vol. 121, pp. 173–182, 2017.
- R. Wang, Y. Tong, A. Manzi, K. Wang, Z.-D. Fu, E. Kentzinger, J. Feldmann, A. S. Urban, P. Müller-Buschbaum, H. Frielinghaus "Preferential Orientation of Crystals Induced by Incorporation of Organic Ligands in Mixed-Dimensional Hybrid Perovskite Films", *Advanced Optical Materials*, vol. 6, pp. 1701311, 2018.
- R. Wang, K. Wang, S.-L. Xia, E. Kentzinger, P. Müller-Buschbaum, H. Frielinghaus "Monitoring quantum confined perovskite nanoplatelets self-assembly in perovskite thin film", *to be submitted*.

Further publications

- X. He, J. Wang, R. Wang, B. Qiu, H. Frielinghaus, P. Niehoff, H. Liu, M. C. Stan, E. Paillard, M. Winter, J. Li, "A 3D porous Li-rich cathode material with an *in situ* modified surface for high performance lithium ion batteries with reduced voltage decay", *Journal of Material Chemistry A*, vol. 4, pp. 7230–7327, 2016.
- X. He, R. Wang, M. C. Stan, E. Paillard, J. Wang, H. Frielinghaus, J. Li, "In Situ Investigations on the Structural and Morphological Changes of Metal Phosphides as Anode Materials in Lithium-Ion Batteries", *Advanced Materials Interfaces*, vol. 4, pp. 1601047, 2017.
- X. He, B. Yan, X. Zhang, D. Bresser, Z. Liu, R. Wang, J. Wang, X. Cao, Y. Su, C. Grey, H. Frielinghaus, D. G. Truhlar, M. Winter, J. Li, E. Paillard, "Ionomer-in-water electrolytes for sustainable Li-ion battery free of fluorine, nickel, cobalt or organic solvents", *submitted*.

Scientific reports

- R. Wang, H. Frielinghaus, P. Müller-Buschbaum, "Conjugated diblock copolymer fullerene bulk heterojunction system in organic photovoltaic application", *Lehrstuhl für Funktionelle Materialien, Annual Report*, 2014.
- R. Wang, H. Frielinghaus, A. Koutsioumpas, S. Mattauch, P. Müller-Buschbaum, "Two dimensional organometal halid perovskite nanosheets in light emitting application", *Lehrstuhl für Funktionelle Materialien, Annual Report*, 2015.
- R. Wang, K. Wang, E. Kentzinger, H. Frielinghaus, P. Müller-Buschbaum, "Morphological evolution in mixed dimensional perovskite thin films - a grazing incidence scattering study", *Lehrstuhl für Funktionelle Materialien, Annual Report*, 2016.
- R. Wang, E. Kentzinger, H. Frielinghaus, P. Müller-Buschbaum, "Self-assembly of quantum confined perovskite nanoplatelets in perovskite thin film", *Lehrstuhl für Funktionelle Materialien, Annual Report*, 2017.

Conference talks

- R. Wang, "Morphology investigation on Copolymer based Organic Solar Cells", *Softcomp ESMI Annual Meeting 2014*, Heraklion (Greece), May 2014.
- R. Wang, Y. Yao "Block Copolymer Films", *E13 Polymer Physics Summer School*, Obertauern (Austria), June 2014.
- R. Wang, "Morphology investigation on conjugated diblock copolymer/fullerene BHJ system", *Fourth Annual Niels Bohr International Academy Workshop-School on ESS science*, Copenhagen (Denmark), November 2014.
- R. Wang, Z.-Y. Di, H. Frielinghaus, P. Müller-Buschbaum, D. Richter, "Conjugated diblock copolymer/fullerene bulk heterojunction(BHJ) system in organic photovolatic application", *DPG-Frühjahrstagung*, Berlin (Germany), March 2015.
- R. Wang, Z.-D. Fu, V. Pipich, A. Koutsioumpas, S. Mattauch, P. Müller-Buschbaum, H. Frielinghaus, "Two dimensional organometal halid perovskite nanosheets in light emitting application", *DPG-Frühjahrstagung*, Regensburg (Germany), March 2016.

Conference poster presentations

- R. Wang, P. Müller-Buschbaum, H. Frielinghaus, "Conjugated diblock copolymer/fullerene bulk heterojunction system in organic photovoltaic application ", *International Conference on Hybrid and Organic Photovoltaics 2015*, Rome (Italy), May 2015.

- R. Wang, P. Müller-Buschbaum, H. Frielinghaus, "Morphology and Optoelectronic Properties of P3HT-*b*-PS/PCBM bulk heterojunction system in organic photovoltaic application ", *6th Colloquium of the Munich School of Engineering*, Garching (Germany), July 2016.
- R. Wang, Y. Tong, P. Müller-Buschbaum, H. Frielinghaus, "Low dimensional lead bromide perovskite in light emitting application – investigation on structure evolution via grazing incidence scattering ", *International Conference on Nanoenergy and Nanosystems 2016*, Beijing (China), July 2016.

Acknowledgments

I would like to thank Prof. Dr. Peter Müller-Buschbaum for giving me the opportunity to continue my research work as a PhD student after my master thesis. I appreciate all his constructive advice and patient guidance throughout my whole Ph.D. period. His foresight in science guides me to accomplish each difficulty that I confronted during my study. Also, I am grateful to his encouragement and trust, which reinforced my motivation and self-confidence. His excellent organizational skills and diligent identity are great fortune for me in my future life.

I would also like to thank Dr. Henrich Frielinghaus, my supervisor from Jülich Centre for Neutron Science (JCNS), Forschungszentrum Jülich GmbH. I am grateful for his open mind and abundant experience on scattering techniques, which greatly help me to accomplish my Ph.D. study. Especially, I appreciate his trust of giving me a lot of space in selecting my interested scientific topics. It is a great pleasure to work with him and I obtained numerous scientific inspirations during our extensive discussions.

I am very grateful to Prof. Dr. Dieter Richter for accepting my application and offered me the opportunity of being a member of JCNS. The financial support by JCNS for both my Ph.D. study and for the great opportunities to participate national as well as international conferences are sincerely acknowledged.

Many thanks to all the beamline scientists that helped me to do the measurements presented in this thesis, namely and in no specific order Dr. Zhenyu Di, Dr. Artem Feoktystov, Dr. Zhendong Fu, Dr. Vitaliy Pipich, Dr. Emmanuel Kentzinger, Dr. Alexandros Koutsioumpas and Dr. Stefan Mattauch. Special thanks go to Kun Wang and Senlin Xia for their kindly assistance on GIWAXS measurements.

Tremendous thanks go to my colleagues from TUM and JCNS for their positive support. With the many collaboration possibilities, I learned and improved a lot through presentations and discussions. I would like to thank Dr. Baohu Wu for his introduction of small angle scattering at the beginning of my Ph.D. study. I am grateful to Johannes Schlipf who offered my a lot of suggestions when I started the perovskite study. I am grateful to Dr. Sabine Pütter and Patrick Schöffmann for their introduction and assistance on AFM measurements. I want to thank Armin Kriele from HZG for the possibility

to measure XRD and XRR. I am sincerely grateful to Patrick Schöffmann and Dr. Judith Houston for their generous help of proof reading the present thesis.

The works presented in this thesis can not be finished without a good working environment. Therefore, I would like to thank all my office mates, Dr. Bob Aldus, Dr. Antonella Campanella, Dr. Bernhard Hopfenmüller, Dr. Alexsandra Steffen, Stefan Holler, Patrick Schöffmann, Xiao Wang, Manuchar Gavaramia and Erxi Feng. All the moments we shared together are great memory for me and I will never forget it in my life.

In the present thesis, I benefited a lot from the excellent collaboration. I am sincerely grateful to Yu Tong, Aurora Manzi, Dr. Alexander Urban and Prof. Dr. Jochen Feldmann from LMU for their kindly offer of optical measurements and results discussions.

Last but not least, I want to thank all my family, especially my parents-in-law and my parents for their unconditional support and steadfast trust. My ineffable gratitude to your love can not be expressed in words and please accept my best wishes for your health and happiness. I love you all so much.

In the end, I want to thank my wife, Wenjun Li. For the ups and downs in the last 7 years, you were here and always being accompany with me. I am very grateful to the chance of meeting you and I appreciate to be a part of your life. Your understanding and trust are my great motivations. I look forward for the every day of our future. I love you.